USAAVRADCOM-TR-81-D-28

LEVEL

AD A109181

STRUCTURAL SYSTEM IDENTIFICATION TECHNOLOGY
VERIFICATION

N. Giansante, A. Berman, W. G. Flannelly, E. J. Nagy
KAMAN AEROSPACE CORPORATION
Old Windsor Road
Bloomfield, Conn. 06602

DTIC
SELECTE**D**
JAN 5 1982
H

November 1981

Final Report

Approved for public release;
distribution unlimited.

82 01 04 016

APPLIED TECHNOLOGY LABORATORY POSITION STATEMENT

The Applied Technology Laboratory has been involved in the development of the Structural System Identification Technology (SSIT) over the past decade. In this program various SSIT concepts of computational algorithms, previously verified on a simulated helicopter structure, were applied on a full-scale helicopter to determine their applicability. The main thrust of this program was directed toward evaluating the Truncated Model and Incomplete Model methods. The Truncated Model method uses test data to identify the modal parameters, such as mass and stiffness, from fewer modes than degrees-of-freedom, and also allows rapid evaluation of structural modification via analytic mass and stiffness changes. The Incomplete Model method can be used when an existing math model, such as a Finite Element (FE) model, yields unsatisfactory vibratory response. The method uses analytic mass and stiffness properties in conjunction with test data to determine the changes required in the mass and stiffness matrices to improve the vibratory response prediction capability of the model. The results obtained from this program indicate that the SSIT methodology can be a useful analytical tool in developing the dynamic design of a helicopter.

Mr. Nicholas J. Calapodas of the Aeronautical Technology Division served as project engineer for this effort.

REPORT DOCUMENTATION PAGE		READ INSTRUCTIONS BEFORE COMPLETING FORM
1. REPORT NUMBER USAAVRADCOM TR 81-D-28	2. GOVT ACCESSION NO. AD-A109 181	3. RECIPIENT'S CATALOG NUMBER
4. TITLE (and Subtitle) STRUCTURAL SYSTEM IDENTIFICATION TECHNOLOGY VERIFICATION		5. TYPE OF REPORT & PERIOD COVERED Final Report
		6. PERFORMING ORG. REPORT NUMBER R-1631
7. AUTHOR(s) N. Giansante E. J. Nagy A. Berman W. G. Flannelly		8. CONTRACT OR GRANT NUMBER(s) DAAK51-78-C-0017
9. PERFORMING ORGANIZATION NAME AND ADDRESS Kaman Aerospace Corporation Old Windsor Road Bloomfield, CT 06002		10. PROGRAM ELEMENT, PROJECT, TASK AREA & WORK UNIT NUMBERS 62209A 1L162209AH 76 00 237 EK
11. CONTROLLING OFFICE NAME AND ADDRESS Applied Technology Laboratory, US Army Research and Technology Laboratories (AVRADCOM) Fort Eustis, Virginia 23604		12. REPORT DATE November 1981
		13. NUMBER OF PAGES 216
14. MONITORING AGENCY NAME & ADDRESS(If different from Controlling Office)		15. SECURITY CLASS. (of this report) Unclassified
		15a. DECLASSIFICATION/DOWNGRADING SCHEDULE

16. DISTRIBUTION STATEMENT (of this Report)

Approved for public release; distribution unlimited.

17. DISTRIBUTION STATEMENT (of the abstract entered in Block 20, if different from Report)

18. SUPPLEMENTARY NOTES

19. KEY WORDS (Continue on reverse side if necessary and identify by block number)

System Identification	Complex Modes
Modal Analysis	Truncated Model
Mechanical Impedance	Incomplete Model
Acceleration Mobility	Force Determination

20. ABSTRACT (Continue on reverse side if necessary and identify by block number)

Structural system identification is the method of obtaining structural and dynamic mathematical models and improving existing mathematical models using ground vibration test data. The purpose of the subject program was to perform experimental, development, and research work to verify the concepts of structural system identification technology. To accomplish this, system identification techniques were applied to a U. S. Army AH-1G helicopter fuselage to create a mathematical model from ground vibration test data, to

DD FORM 1473 EDITION OF 1 NOV 65 IS OBSOLETE
1 JAN 73

404362

20. ABSTRACT (Continued)

improve a reduced model of an existing NASTRAN model of the AH-1G using shake test data, and to test the effectiveness of these new mathematical models in predicting the effects of stiffness and mass changes to the airframe.

The results of the program indicate that system identification is a viable and cost-effective technique for developing new models and for improving existing finite-element models of an airframe using ground vibration test data.

PREFACE

The work presented in this report was performed by Kaman Aerospace Corporation under Contract DAAK51-78-C-0017 for the Applied Technology Laboratory, U. S. Army Research and Technology Laboratories (AVRADCOM), Fort Eustis, Virginia. The program was implemented under the technical direction of Nicholas J. Calapodas of the Aeronautical Technology Division.

The report presents a general description of the analytical and experimental techniques for implementing system identification methodology with specific application to the AH-1G airframe.

Accession For

NTIS GRA&I
DTIC TAB
Unannounced
Justification

By
Distribution/
Availability Codes
Avail and/or
Dist   Special

3

SUMMARY

The purpose of this program was to perform experimental and analytical
work to verify the structural system identification methodology developed
at Kaman Aerospace Corporation. To accomplish this, system identification
techniques were applied to a U. S. Army AH-1G airframe (S/N 57-15683) to
create mathematical models from dynamic test data and to improve a reduced
version of the existing NASTRAN model of the AH-1G helicopter using dynamic
test data. An additional objective of the program was to test the effect-
iveness of the mathematical models developed in predicting the effects of
structural stiffness and mass changes to the helicopter.

The analytical models that were developed proved to be effective in pre-
dicting the effects of the stiffness and mass changes which were incorpor-
ated in the helicopter. Additionally, the improved version of the reduced
NASTRAN model successfully predicted the frequency response of the AH-1G
airframe for the frequency range of interest.

A significant part of the program involved development and refinement of
test procedures for acquiring impedance type test data which would yield
modal data suitable for implementation of the system identification method-
ology. Complex modes resulting from elastomeric isolators and nonstruc-
tural access panels were found to exist in the AH-1G airframe. These com-
plex modes were successfully measured, which represents an advancement
in the state of the art of dynamic testing and modal parameter extraction.

TABLE OF CONTENTS

LIST OF ILLUSTRATIONS

LIST OF ILLUSTRATIONS (CONCLUDED)

LIST OF TABLES

9

LIST OF TABLES (CONTINUED)

LIST OF TABLES (CONTINUED)

LIST OF TABLES (CONCLUDED)

INTRODUCTION

High vibration levels experienced by current production helicopters result
in fatigue damage to airframe structure and components with ultimate re-
duction in reliability. Additionally, high vibratory structural response
and accompanying high noise levels in the cabin area degrade the efficien-
cy, health, and comfort of both the crew and passengers. Currently, the
solution to this problem relies on flight test information to effect vibra-
tion reduction procedures, but these procedures result in high cost and
schedule delays. An alternate solution is to develop analytical methods to
accurately predict the vibration response characteristics of the helicopter
and allow structural modifications during prototype development to reduce
vibration levels with inherent lower development time and cost.

Thus, the Army has a continuing goal to improve analytical methods capable
of predicting the vibration levels experienced by a helicopter in flight.
One aspect of this involves the analytical modeling of rotorcraft airframes
and, in particular, use of the finite-element method to make analytical
predictions of airframe vibration frequencies and responses. The finite-
element method, which is the only method in general use capable of the
detailed mathematical modeling of helicopter structures, has experienced
difficulty in predicting airframe vibration. Consequently, improvement
in the modeling of helicopter structures for the purpose of vibration
prediction is essential.

Once a prototype has been built, system identification methodology can be
used to generate mathematical models or to improve existing analytical
models using ground vibration test data. Thus, system identification can
be applied to combine test data and analytical models into an engineering
tool useful in developing new rotorcraft and in incorporating modifica-
tions to existing airframes. System identification unifies analyses de-
veloped from idealizations regarding the mass, stiffness, and damping
characteristics of the structure with dynamic test methods resulting in
improved mathematical models which can successfully predict the dynamic
response characteristics of the helicopter.

13

Kaman Aerospace Corporation has developed system identification methodology through two separate techniques. The Incomplete Model and the Truncated Model methods have progressed successfully from theoretical formulation, computer simulations, application to small structures, and finally to full-scale craft applications.

The purpose of the present program was to apply system identification methodology to the AH-1G airframe to create a mathematical model, to improve the existing NASTRAN model using dynamic test data, and to test the effectiveness of the mathematical models in predicting the effects of mass and stiffness changes to the airframe. The program involved extensive shake tests of several mass and stiffness configurations and extraction of natural frequencies, orthonormal mode shapes, and modal parameters for the respective conditions.

Ground vibration tests of the AH-1G helicopter revealed that the airframe is characterized by complex mode shapes which are caused by the nonproportional distribution of damping resulting from the elastomeric isolators and nonstructural access panels in the structure. These complex modes were successfully measured during the test phase of the program; however, both the Incomplete Model and the Truncated Model, which rely on mode shapes in their formulation, cannot, currently, accommodate the complex modes. Consequently, the complex modes had to be transformed to the real domain for use in the theories. It is essential that the Incomplete Model and Truncated Model methodologies be extended to include the complex mode feature to improve the accuracy of their vibration prediction capability.

NASTRAN MODEL

EXISTING NASTRAN MODEL OF AH-1G

An important aspect of helicopter vibration prediction is related to the analytical modeling of the airframe, and, in particular, the use of the finite element method to make analytical predictions of the dynamic response characteristics of the vehicle. The finite element method is the only method in general use that is capable of the detailed mathematical modeling required for the analysis of the complex, redundant airframe structures of modern helicopters. The basic NASTRAN model of the AH-1G helicopter used in the current program is documented, in detail, in Reference 1. The NASTRAN model was developed to represent the vibration response of the AH-1G airframe for excitation frequencies below 30 Hz. Figure 1 illustrates the actual airframe structure with skins removed and Figure 2 presents the NASTRAN model, which consists of a built-up idealization of the fuselage and an elastic line representation for the tail boom, vertical fin, and horizontal stabilizer. As described in Reference 1, several regions of the structure are not effective in providing stiffness and are not included in the NASTRAN model. These components are the canopy, cowling around the engine and main rotor pylon, access panels at fuselage station (FS) 61.25 in. to 213.94 in., doors on the ammunition bay at FS 95 in. to 135 in., top access door on the nose at FS 33 in. to 45 in., and the drive shaft connection of the engine to the main transmission. The model was intuitively developed using structural elements available in the NASTRAN library and consists of bars, rods, shear panels, triangular and quadralateral plate elements, and scalar spring elements.

1. Cronkhite, James D., et al. A NASTRAN VIBRATION MODEL OF THE AH-1G HELICOPTER AIRFRAME, Vol. 1, USAAMRDL R-TR-74-045, Rock Island Arsenal, U. S. Army Air Mobility Research and Development Laboratory, Rock Island, Illinois, June 1974, AD-A009482.

Helicopter Airframe Structure
(skins removed)
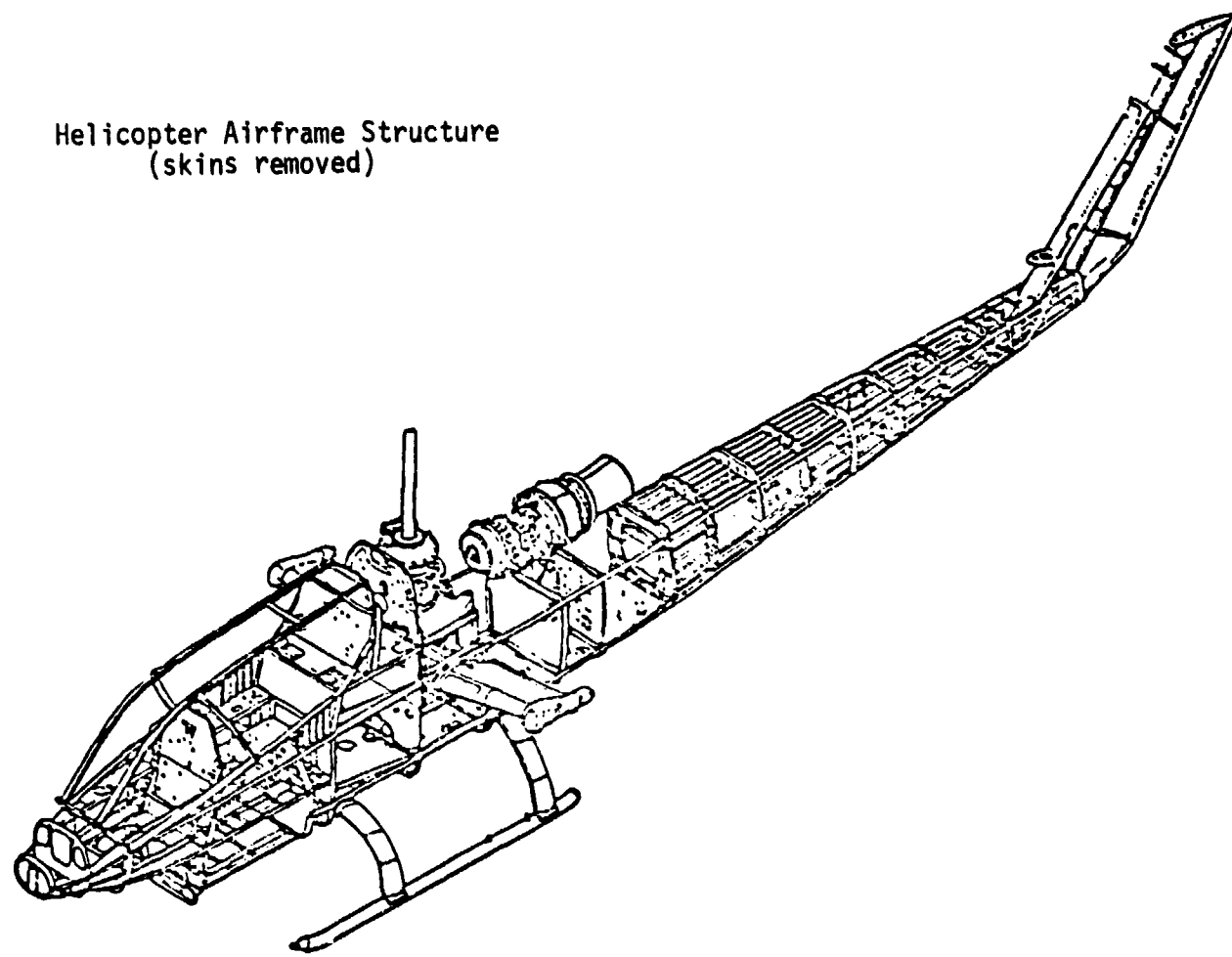
Figure 1.   AH-1G helicopter airframe structure.

Degrees of Freedom		Elements	
K_{gg}	2940	BAR	184
K_{nn}	2699	ROD	2013
K_{ff}	1714	SHEAR	340
K_{aa}	241	QDMEN	160
K_{11}	235	TRMEM	243
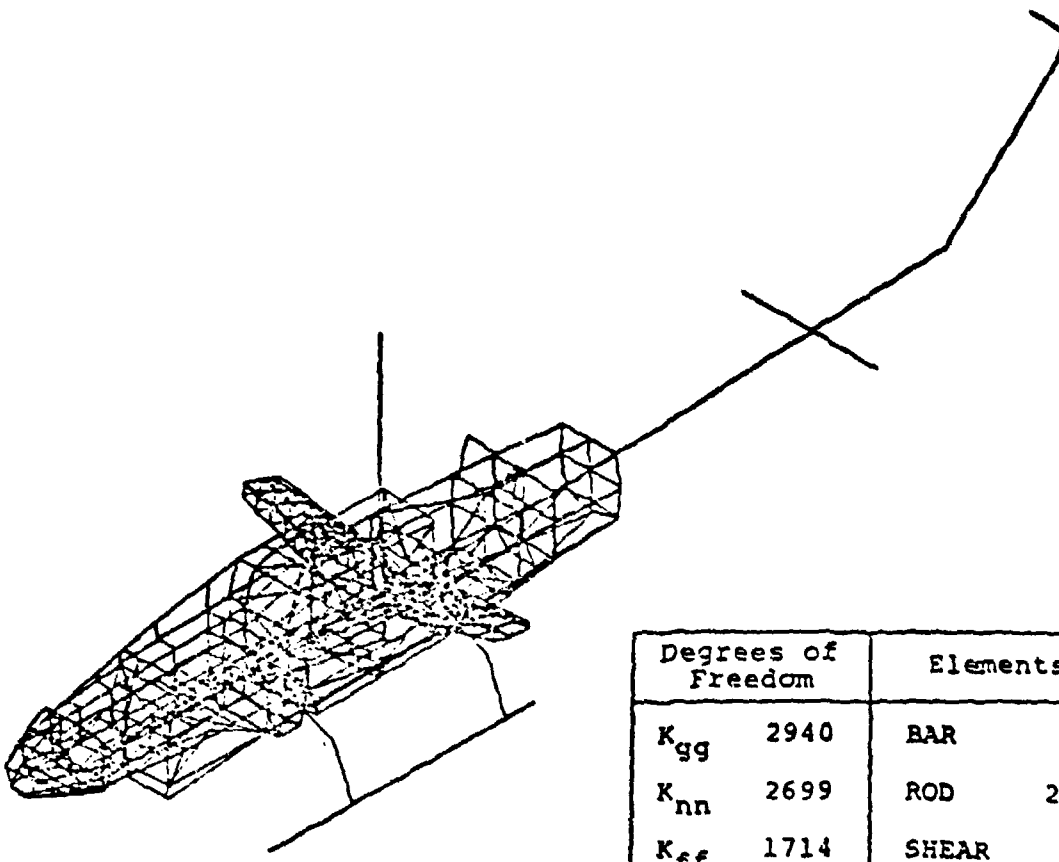
Figure 2. AH-1G NASTRAN dynamics model.

NASTRAN MODEL USED IN SYSTEM IDENTIFICATION

Originally, the NASTRAN model contained 2940 degrees of freedom and was
reduced to 2699 degrees of freedom through the use of Multi-Point Constraint
(MPC) equations. Use of the MPC equations allows description of a degree
of freedom as a linear combination of the values of two or more degrees of
freedom. The model was further reduced to 1714 degrees of freedom by the
application of Single Point Constraints (SPC), which forces a degree of
freedom to zero. Use of the GUYAN reduction, which is a static condensation
procedure, further deleted the degrees of freedom to 98, and eliminating
six support degrees of freedom reduced the model to the final 92 degrees
of freedom.

The existing NASTRAN model of the AH-1G was reduced to 92 degrees of free-
dom for the purpose of the Structural System Identification Technology Veri-
fication Program. The 92 degrees of freedom selected were consistent with
the locations of the accelerometers placed on the airframe as described
in Reference 2 and consistent with the requirements of the subject con-
tract.

GUYAN Reduction

The mathematics of the static condensation procedure that yields the re-
duced mass and stiffness matrices in a NASTRAN dynamic analysis is briefly
described. Since the technique is a static condensation it is theoretically
applicable only at zero excitation frequency. However, it is generally
used independent of excitation frequency. The formulation is similar to

2.   Jones, R., et al., EXPERIMENTAL VERIFICATION OF FORCE DETERMINATION
     AND GROUND FLYING ON A FULL-SCALE HELICOPTER. Kaman Aerospace Cor-
     poration Report Number R-1625, USAAVRADCOM-TR-81-D-11, Applied Tech-
     nology Laboratory, U. S. Army Research and Technology Laboratory,
     Fort Eustis, Virginia, 23604, May 1981, AD A100182.

that of Reference 3 and is presented here only for completeness. The equilibrium equations for a structure may be written as

$$[K] \{x\} = \{F\} \tag{1}$$

The structural equations can be rearranged and written in partitioned form as

$$\begin{bmatrix} K_{11} & | & K_{12} \\ \hline K_{12}^T & | & K_{22} \end{bmatrix} \begin{Bmatrix} x_1 \\ \hline x_2 \end{Bmatrix} = \begin{Bmatrix} F_1 \\ \hline F_2 \end{Bmatrix} \tag{2}$$

Assuming that no forces are applied at the coordinate set x_2 the two resulting matrix equations developed from equation (2) become

$$K_{11} x_1 + K_{12} x_2 = F_1 \tag{3}$$

$$K_{12}^T x_1 + K_{22} x_2 = 0 \tag{4}$$

The coordinate set x_2 can be obtained from equation (4)

$$x_2 = -K_{22}^{-1} K_{12}^T x_1 \tag{5}$$

Substituting equation (5) into equation (3) will eliminate the coordinates x_2

$$\left[K_{11} - K_{12} K_{22}^{-1} K_{12}^T \right] x_1 = F_1 \tag{6}$$

where $[K]_{RED} = \left[K_{11} - K_{12} K_{22}^{-1} K_{12}^T \right]$ is defined as the reduced stiffness matrix. The original coordinate system has effectively been

---

3. Guyan, R., Reduction of Stiffness and Mass Matrices. AIAA JOURNAL, vol. 3, No. 2, February 1965, pp. 380.

transformed to the coordinate system at which forces are considered to act, thus

$$\left\{ x \right\} = \left\{ \begin{array}{c} x_1 \\ \hline x_2 \end{array} \right\} = \left[\begin{array}{c} I \\ \hline -K_{22}{}^{-1} K_{12}{}^T \end{array} \right] \left\{ x_1 \right\} \tag{7}$$

or

$$\left\{ x \right\} = [T] \left\{ x_1 \right\}$$

The kinetic energy can be written as

$$V = \frac{1}{2} \left\{ x \right\}^T [M] \left\{ x \right\} \tag{8}$$

Substituting equation (7) into equation (8) yields

$$V = \frac{1}{2} \left\{ x_1 \right\}^T [T]^T [M] [T] \left\{ x_1 \right\} \tag{9}$$

The reduced mass matrix is then defined as

$$[M]_{RED} = [T]^T [M] [T] \tag{10}$$

Substituting for [T] from equation (7) and writing equation (10) in partitioned form, the result is

$$[M]_{RED} = \left[I \;\vdots\; -K_{22}{}^{-1} K_{12}{}^T \right] \left[\begin{array}{c|c} M_{11} & M_{12} \\ \hline M_{21} & M_{22} \end{array} \right] \left[\begin{array}{c} I \\ \hline -K_{22}{}^{-1} K_{12}{}^T \end{array} \right] \tag{11}$$

or

$$[M]_{RED} = \left[M_{11} - \left[K_{22}{}^{-1} K_{12}{}^T \right]^T M_{12}{}^T \;\vdots\; M_{12} \right.$$

$$\left. - \left[K_{22}{}^{-1} K_{12}{}^T \right]^T M_{22} \right] \left[\begin{array}{c} I \\ \hline -K_{22}{}^{-1} K_{12}{}^T \end{array} \right]$$

and finally

$$[M]_{RED} = \left[M_{11}\right] - \left[M_{12} \ K_{22}^{-1} \ K_{12}^{T}\right]$$

$$- \left[K_{22}^{-1} \ K_{12}^{T}\right]^{T} \left[M_{12}^{T} - M_{22} \ K_{22}^{-1} \ K_{12}^{T}\right] \qquad (12)$$

The reduced mass and stiffness matrices developed in the Guyan Reduction procedure are nondiagonal.

NASTRAN Model Gross Weight Configuration

The NASTRAN model of the AH-1G as described in Reference 1 was developed for a production configuration identified as FY71 S/N 21123. The AH-1G S/N 57-15683 was used in the Structural System Identification Technology Verification Program. As a result, the existing Government-furnished NASTRAN model of the AH-1G had to be modified for compatibility with the aircraft tested. This required modifying large weight items and useful load items. The gross weight configuration of the original NASTRAN model was 8933 lb, consisting of a total weight empty of 5760 lb and a useful load of 3173 lb. In addition, the main rotor blade weight and main rotor hub weight were included in the model as concentrated weights. The NASTRAN model of the aircraft that was shake tested during the subject contract was 8750 lb; the main rotor blades were omitted and only 231 lb of hub weight were included. The following tabulations describe the concentrated mass items that were changed from the original NASTRAN AH-1G model.

	LB
Original NASTRAN AH-1G Model	8933
Weight deleted	
XM-28 Gun Turret Launcher	41
Mini-gun	48
40-mm Drum/Pallet	75
40-mm Grenades (250 rounds)	190
7.62-mm Mamee Drum	63
7.62-mm Ammunition (4000 rounds)	260

21

Forward Fuel	780
Aft Fuel	830
Pilot	200
Gunner	200
Main Rotor Hub	490
Main Rotor Blades	458
XM-157A Pod (Right Wing)	57
M-151/XM 429 Rockets (Right Wing)	146
XM-157A Pod (Left Wing)	57
M-151/XM 439 Rockets (Left Wing)	146
Smoke Grenades and Dispenser (Right Wing)	40
Smoke Grenades and Dispenser (Left Wing)	40
	4121

NASTRAN model of AH-1G S/N 57-15683
  Weight added

Test Instrumentation	195
M200 A/1 Inboard Rocket Pod/19 Rockets (Right Wing)	529
Inboard Pylon Assembly (Right Wing)	31
M200 A/1 Inboard Rocket Pod/19 Rockets (Left Wing)	529
Inboard Pylon Assembly (Left Wing)	31
M200 A/1 Outboard Rocket Pod/12 Rockets (Right Wing)	385
M200 A/1 Outboard Rocket Pod/12 Rockets (Left Wing)	385
Main Rotor Hub	231
Turret Ballast	150
Gun Sight Ballast	25
Pilot	230
Gunner	180
Fuel	933
Instrumentation (accelerometers,wire,etc.)	100
	3934

Thus, the NASTRAN model weight for the configuration tested was

$$WT = 8933 - 4121 + 3934 = 8746 \text{ lb}$$

This compares with the actual weight of the test vehicle of 8784 lb

Coordinate Selection

Selection of coordinates on the AH-1G fuselage was based on requirements for determining the modal acceleration coefficients of the structure. In NASTRAN, the Guyan reduction is the technique used for reducing the number of static degrees of freedom to be used in a dynamic analysis. It implies a meaningful redistribution of inertia properties to a subset of the total number of degrees of freedom required in a static analysis of the structure. One of the primary requirements in selection of the dynamic analysis set of coordinates is that they should be uniformly distributed throughout the structure. This insures that the modal acceleration coefficients and, subsequently, the orthonormal modes will be representative of the deformation patterns of the structure.

Ideally, the transformation from the full size model to the smaller size required for an operational model can be achieved with the reduced model capable of accurate analytical prediction of the dynamic response characteristics of the vehicle. Practically, however, the reduction process introduces error in the smaller size model. Minimizing the error inherent in the reduction procedure is of paramount importance. Guidelines for developing the reduced model through implementation of the Guyan Reduction procedure are described in Reference 1. These principles were carefully followed in selecting degrees of freedom pertinent to the AH-1G reduced model. A total of 92 degrees of freedom were used in the reduced NASTRAN model used in the study. The government-furnished NASTRAN model consisting of 2940 degrees of freedom was reduced to 92 degrees of freedom using SPC, MPC, and the Guyan technique.

Accelerometer Location

A total of 92 accelerometers were available on the AH-1G fuselage for use in the current program. Of this total, 58 accelerometers were positioned at locations pertinent to the system identification program and 34 accelerometers had been installed for previous use as described in Reference 2.

Generally, the locations for placement of the accelerometers on the AH-1G fuselage were selected within the constraints specified in Reference 1. Ideally, the fuselage station, butt line station, and water line station of each accelerometer should coincide with a particular grid point in the NASTRAN model. However, since the accelerometers were rigidly attached to the structure via mounting blocks to minimize extraneous localized response effects it was not possible, in every instance, to locate the accelerometers coincident with a NASTRAN grid point. The accelerometers were placed with direction of major sensitivity oriented appropriately with respect to the fuselage station, butt line, and water line orthogonal axes system. In addition, accelerometers oriented with major axis in the water line direction but offset from the butt line zero axis could provide a measure of the torsional deformation of the fuselage. The positive directions in the axes system were aft, up and to the right, as viewed from the pilot seat. Table 1 presents a listing of the accelerometer designation and location on the AH-1G in terms of fuselage, butt line, and water line stations.

The accelerometer identifications are prefixed by either the letters X, Y or Z, which refer to the direction of acceleration measurement in the longitudinal, lateral or vertical directions, respectively. Additionally, the letters R, L, T and B are used as suffixes to describe the location of the accelerometer, with R and L referring to right and left distances from the butt line zero reference, and T and B referring to top and bottom surface of the fuselage. As an illustration of the accelerometer identification, Z46R refers to an accelerometer that is oriented for measurement of acceleration along the vertical axis, the number 46 refers to the nominal fuselage location, and the suffix R indicates the right side or positive lateral axis direction. The actual position of accelerometer Z46R is given in the table as FS 46 in., BL 9.5 in., and WL 65.5 in. Figure 3 presents geometric data and the reference axes system for the AH-1G test program.

24

TABLE 1. ACCELEROMETER DESCRIPTION.

No.	Accelerometer Identification	Fuselage Station	Butt Line Station	Water Line Station	D.O.F. No.
1	Y46L	46.00	-10.10	45.00	91
2	Z46R	46.00	9.50	65.50	89
3	Y50	40.25	0.00	52.00	90
4	Z50	38.75	0.00	52.00	92
5	X60R	59.75	9.50	51.50	82
6	Y60L	60.25	- 9.50	59.50	86
7	Z60L	60.00	-17.50	60.00	87
8	Z61R	61.25	17.50	60.00	88
9	Y90	103.00	0.00	52.00	83
10	Z90R	100.75	20.00	50.00	79
11	Z90L	100.75	-20.00	50.00	85
12	Z92L	92.00	-18.00	46.00	84
13	Z93R	93.00	19.00	46.00	81
14	Y95R	95.00	9.50	46.50	80
15	Z100T	102.75	0.00	100.00	78
16	Y115R	115.00	10.00	45.00	77
17	Z115R	115.00	8.75	62.00	76
18	Y139R	139.00	18.00	46.00	73
19	X140	138.00	0.00	50.00	71
20	Y140	138.00	0.00	50.00	72
21	Z140R	133.50	20.00	50.00	65
22	Z140L	134.50	-20.00	50.00	75
23	Z147R	147.00	8.70	55.50	70
24	Y152L	152.45	-12.50	27.50	74
25	Z155R	155.50	12.00	28.50	68
26	Y156	156.41	0.00	35.00	66
27	Z156R	156.41	19.00	36.00	69
28	Z156L	156.41	-19.00	36.00	67
29	X180T	209.00	- 6.50	125.00	26
30	Y187	187.50	0.00	46.00	63
31	X188	187.75	0.00	56.95	62

TABLE 1. CONTINUED.

No.	Accelerometer Identification	Fuselage Station	Butt Line Station	Water Line Station	D.O.F. No.
32	Z189	189.25	0.00	36.50	64
33	Z195B	195.10	0.00	65.00	37
34	Z195T	195.10	0.00	75.00	25
35	ZLONG	196.00	12.00	59.00	36
36	ZLATR	196.00	-12.00	59.00	38
37	ZCOLL	207.00	-12.00	57.00	34
38	X200R	193.50	55.00	65.00	55
39	X200L	193.50	-55.00	65.00	59
40	Z200R	193.50	55.00	65.00	56
41	Z200L	193.50	-55.00	65.00	60
42	Z201R	201.10	42.50	65.00	54
43	Z201L	201.10	-42.50	65.00	58
44	Z202R	202.00	60.00	63.10	57
45	Z202L	202.00	-60.00	63.10	61
46	XMHUB	197.00	0.00	157.05	29
47	YHUB	198.38	2.00	157.05	30
48	ZHUB	198.38	0.00	158.18	31
49	MZHUB	201.50	0.00	149.55	32
50	Z210T	207.00	- 7.00	125.00	28
51	Z215R	214.70	18.59	55.58	52
52	Z215L	214.70	-18.59	55.58	53
53	X220L	212.00	-20.00	35.00	51
54	Y220B	212.00	0.00	35.00	50
55	Y220T	208.00	- 8.00	125.00	27
56	Y226R	226.41	10.18	29.15	46
57	Z226	226.40	0.00	35.12	48
58	Z226L	226.41	-10.67	29.09	49
59	Y229R	229.12	7.86	26.00	47
60	Z250	250.00	0.00	64.07	35
61	Y251	251.37	0.00	52.59	39
62	Z251	251.00	0.00	79.50	33

4
B

TABLE 1. CONTINUED.

No.	Accelerometer Identification	Fuselage Station	Butt Line Station	Water Line Station	D.O.F. No.
63	Y267	267.25	1.00	64.50	41
64	Z268R	268.25	12.00	64.50	40
65	Z268L	268.25	-12.00	64.20	42
66	Y300	300.00	6.00	50.00	43
67	X301	300.70	- 0.50	30.75	44
68	Z301	301.20	0.00	30.00	45
69	Y339L	338.61	-13.00	57.02	6
70	Z340	341.50	0.00	42.00	7
71	Y380	379.00	0.00	50.00	4
72	Z381	381.09	0.00	42.25	5
73	Z396R	396.50	21.50	60.00	2
74	Z396L	396.50	-21.50	60.00	3
75	Z400	400.00	0.00	48.00	9
76	Z404R	404.00	31.25	56.50	1
77	X405	405.33	- 0.50	44.75	8
78	Y422L	422.24	- 9.00	57.21	10
79	Z422L	422.24	- 8.50	57.71	12
80	Z423	423.08	0.00	46.25	11
81	Y440	448.00	0.00	50.00	13
82	Z460	465.40	0.00	65.00	18
83	Y464L	464.10	- 7.00	59.81	14
84	Z464	464.10	0.00	51.75	15
85	X479	479.23	0.00	54.25	16
86	Y480	480.23	- 4.00	72.40	17
87	Z485	485.50	0.00	93.25	20
88	Y490	489.00	0.00	75.00	19
89	Y517	517.50	- 5.50	105.25	21
90	Y521	520.67	- 4.00	118.27	23
91	X540	545.00	0.00	135.00	22
92	Z540	545.00	0.00	135.00	24
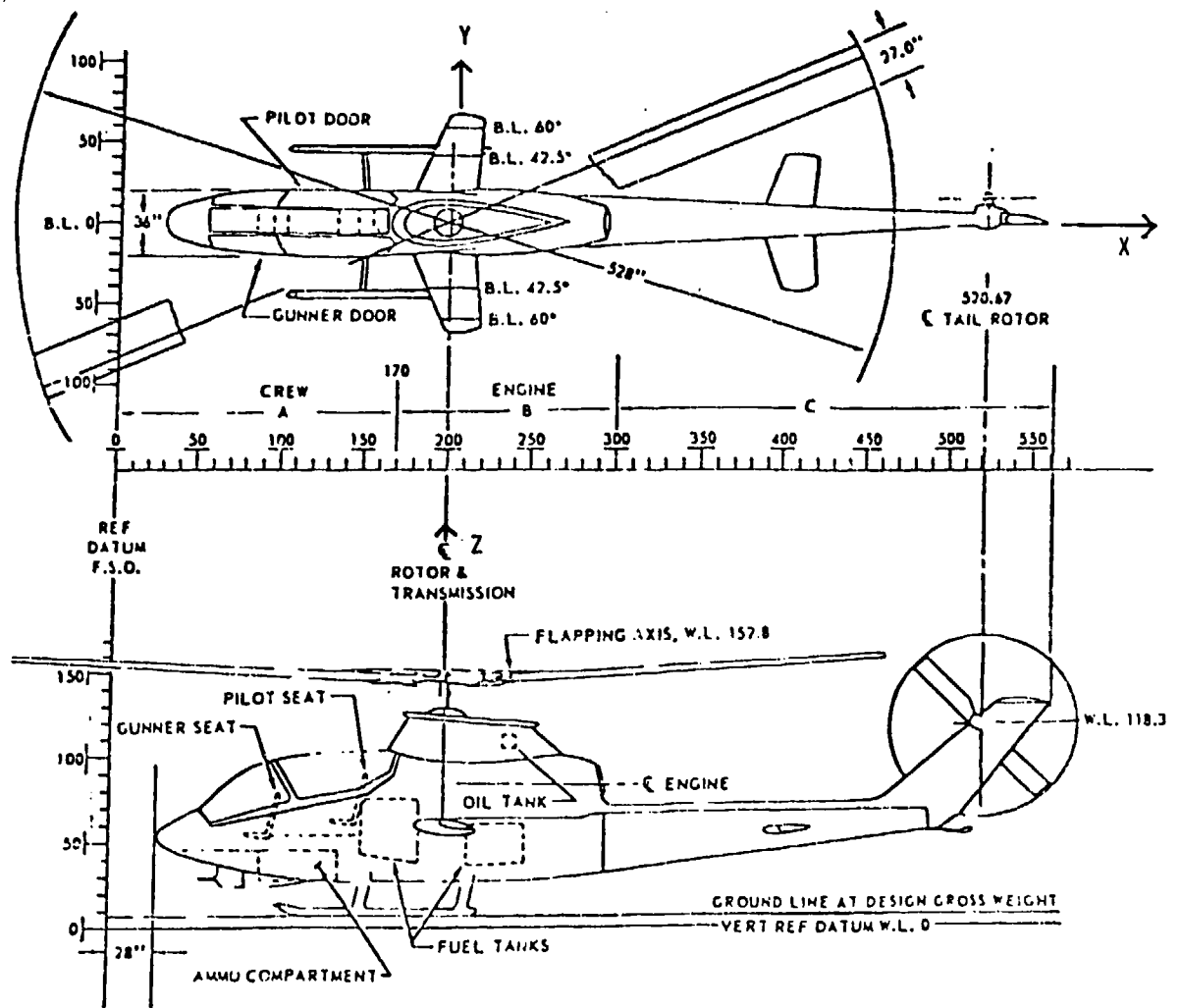
Figure 3. AH-1G axis system.

28

MODE SHAPES

CLASSICAL MODES

Classical modes, frequently referred to as normal modes, exist in systems which have proportional damping of any magnitude. This implies that the mode shapes for the damped system are the same as those for the system with zero damping. The motion in any mode is characterized by the existence of fixed nodes on the structure, and all points in the system attain their maximum or minimum response simultaneously. Therefore the elements of each node will either have the same phase or be 180 degrees out of phase, describing a standing wave pattern.

In addition, if the modes are reasonably separated in frequency, the real part of the acceleration mobility will display two turning points in the vicinity of a natural frequency and the imaginary part of the acceleration mobility will show a single turning point at the natural frequency. Figure 4a presents acceleration mobility measurements obtained on the AH-1G airframe. The figure shows a transfer function relating vertical acceleration measured at a point in the nose of the airframe (Z50) for excitation applied vertically at the tail skid (Z485). Two close, but distinguishable, modes are present. The dominant mode is essentially classical, displaying two turning points in the real acceleration mobility and a single turning point in the imaginary acceleration mobility measurements. Figure 4b shows the acceleration mobility data in the complex plane commonly referred to as the Nyquist diagram.

COMPLEX MODES

Complex modes exist in a structure if it is characterized by the presence of nonproportional damping. In the classical situation, the modes are distinguished by a shape wherein all points in the system attain their maximum or minimum motion at the same time. In contrast, a system with nonproportional damping, and therefore complex modes, is not characterized

29
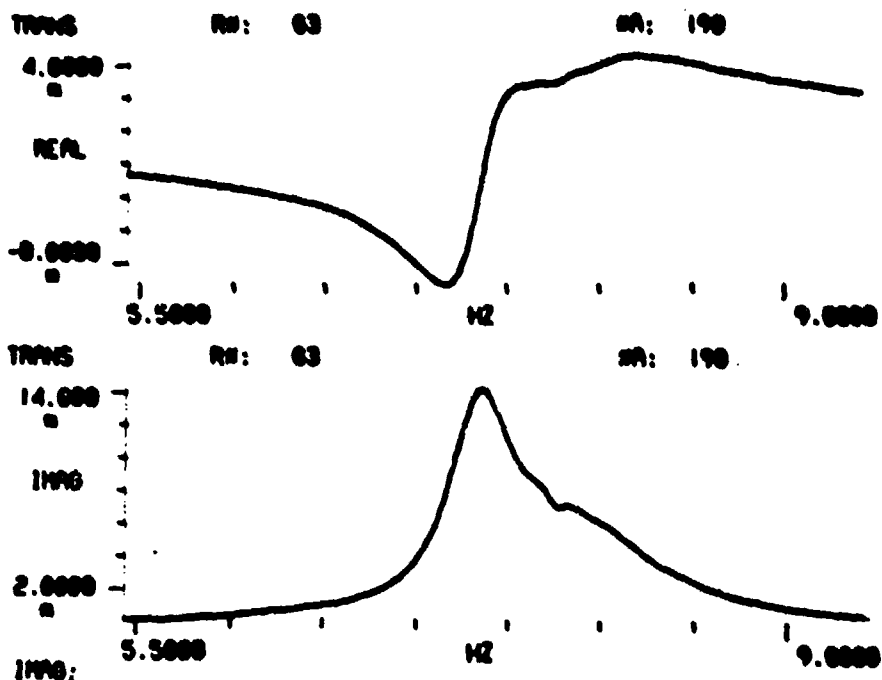
a. Measured acceleration mobility.
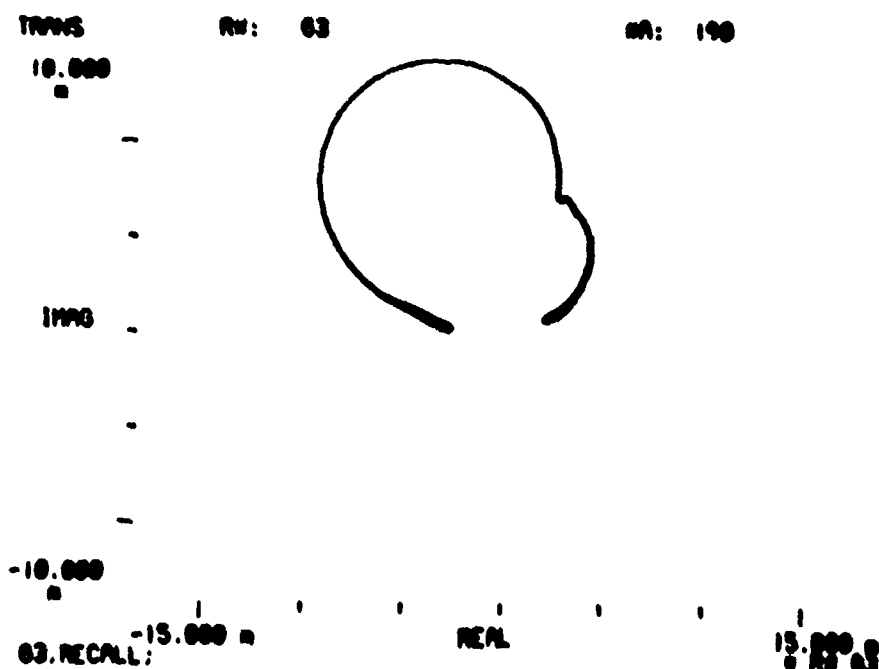
b. Nyquist diagram (frequency 5.5-9.0 Hz)

Figure 4. Acceleration Mobility of the AH-1G.

30

by the presence of fixed nodes in each mode of vibration. Rather, the
points on the structure undergo motion at the same frequency, but with
different phase relationships. Hence, complex modes can be described
as traveling waves as opposed to standing waves, which distinguish the
normal modes of vibration.

For the general case of nonclassical or complex modes the real and imagin-
ary acceleration mobility may not exhibit the characteristic shape displayed
in the classical mode situation. It is possible for the imaginary mobility
to display two turning points in the region of a natural frequency while
the real mobility may show a single turning point at a natural frequency.
Figure 5a shows an example of this phenomenon in data measured on the AH-1G
airframe. The data presented are for a transfer function describing the
acceleration response measured at the nose of the airframe for force excita-
tion applied vertically at the tail skid. It is also possible that either
or both of the real and the imaginary parts of the acceleration mobility
will display two turning points proximate to a natural frequency.
Figure 5b shows che aforementioned measured acceleration mobility in the
complex plane.

Complex modes are likely to exist in a helicopter airframe because of the
nonproportional distribution of damping. In the AH-1G airframe, elastomeric
isolators and nonstructural access panels are the source of nonproportional
damping resulting in the existence of complex modes.

MAJOR MODES

In evaluating the overall dynamic response of a system, the relative contri-
bution of each of the modes in a given frequency range of interest is of
paramount importance. The problem of identifying the significant natural
frequencies of a structure is related to distinguishing the difference
between what can be considered to be a major mode and what can be defined
as a minor or local mode. At a particular excitation frequency, it is
possible to excite a local or minor elastic mode which has negligible

31
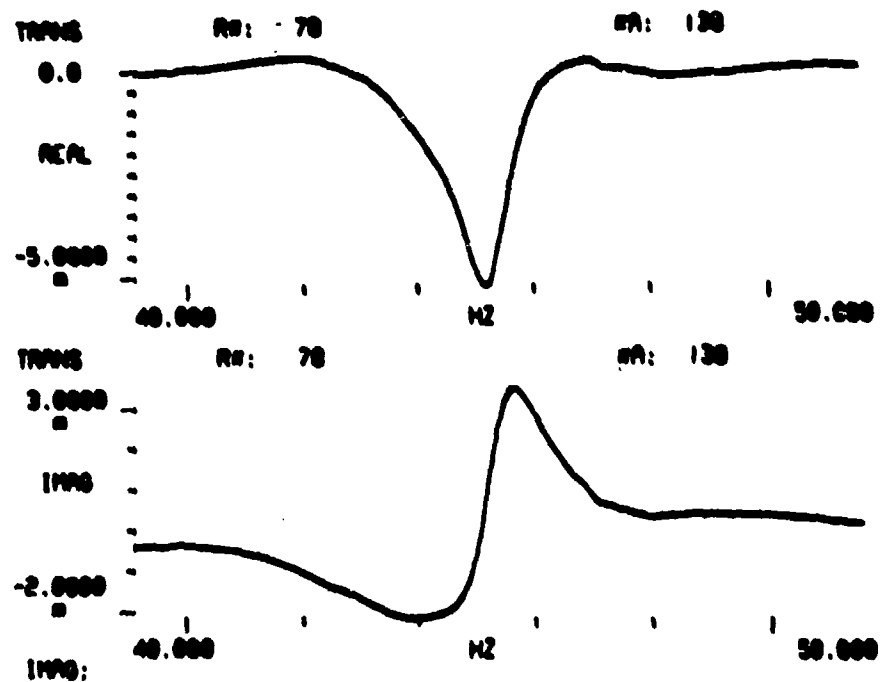
a. Measured acceleration mobility.
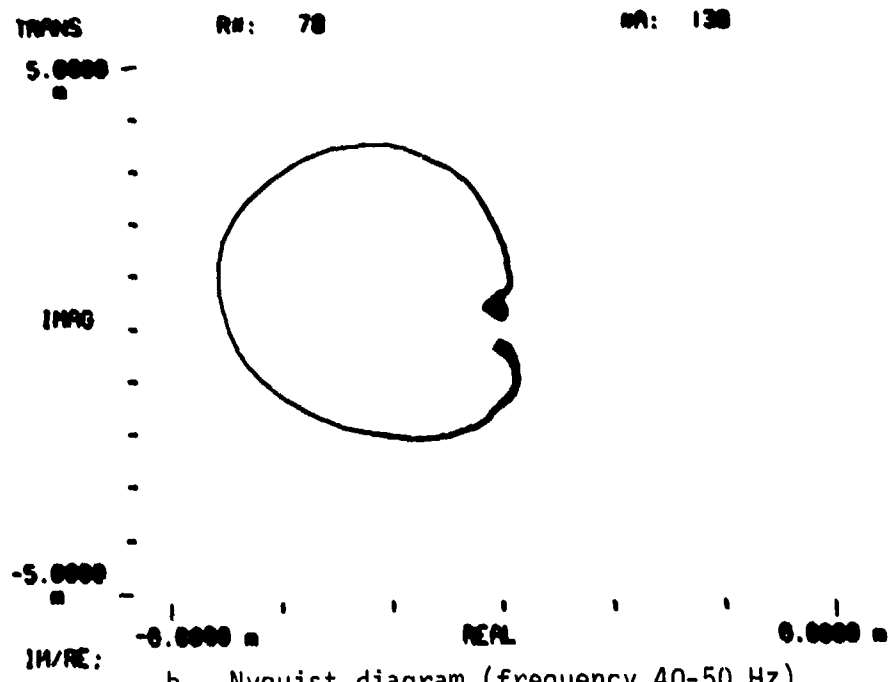
b. Nyquist diagram (frequency 40-50 Hz).

Figure 5. Acceleration Mobility of the AH-1G.

effect on the overall system dynamic response. As an example, consider the flexural vibrations of the tail skid on the AH-1G helicopter. Acceleration mobility measurements on that structure will show the natural frequencies, damping coefficients and mode shapes of all the elastic modes involving the motion of the tail skid. Obviously, these modes are not relevant to the dynamic behavior of the airframe. However, with only normal mode shapes, natural frequencies, and structural damping coefficients obtained from the test data, the question of modal significance cannot be answered. If, however, the normal mode is combined with the generalized mass the result is the orthonormal mode which has physical units. Modes of physical units are absolutely necessary in distinguishing major modes from local modes. Additionally, the Euclidean norm of each mode $\psi_i^T \psi_i$ is a quantity that has physical significance and indicates the relative contribution of each mode to the total structural dynamic response.

Local or Residual Modes

Certain points on an airframe exhibit response characteristics, as evidenced by their modal acceleration properties, which may be significantly higher in any mode than those of other points on the structure. This effect defines a local mode since only geometrically proximate orthonormal modal elements are extraordinarily large in the particular mode. This effect is most critical at a driving point although it may also occur in transfer mobilities. The result is that high frequency local modes can have a pronounced effect on mobilities at much lower frequencies. During dynamic testing of the AH-1G, at Kaman Aerospace Corporation, the discovery was made that high frequency local modes, in the 400-Hz range, could severely influence the low frequency response of the airframe. This phenomenon was observed when force excitation was applied at low frequency for driving point measurements. It occurred during AH-1G dynamic tests for vertical excitation applied proximate to the tail skid attachment point and for vertical excitation applied on the airframe in the vicinity of the horizontal tail. This effect was not witnessed, however, for hub shaking or for lateral force excitation

33

applied at the tail rotor gearbox. Although a common happening, this local mode effect does not occur at all driving points.

Figure 6 shows the real and imaginary parts of the driving-point acceleration mobility measured at the tail skid attachment point of the AH-1G airframe for a frequency range of 0 to 100 Hz. It is evident that the acceleration mobility is steadily drifting away from the zero reference mobility axis. Apparently, the bounds of a local mode have not been spanned. Indeed, when the frequency spectrum is expanded to 800 Hz, as shown in Figure 7, the residual modes occurring in the 400-Hz range are clearly evident. The modal coefficients associated with these modes are large, and if not properly removed analytically can contribute significantly to the acceleration mobility measured at lower frequencies.

The modal parameter extraction techniques that were employed in the analysis require mobility data acquired at discrete frequencies on either side of a natural frequency. Since the methods operate on a mobility difference proximate to the natural frequency, the local mode or residual effect is minimized.
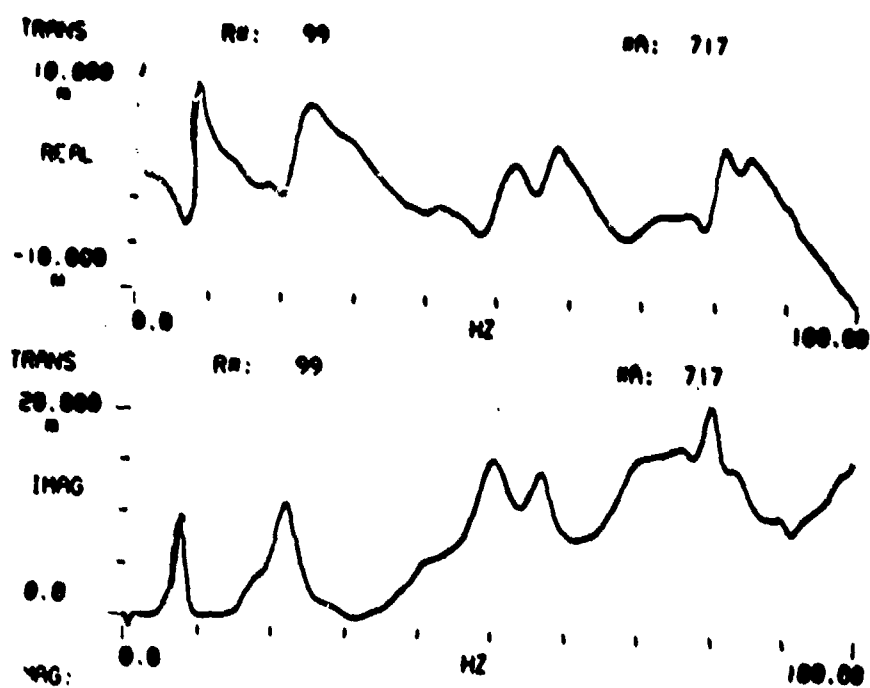
Figure 6. Tail vertical driving point acceleration
mobility (frequency 0-100 Hz).
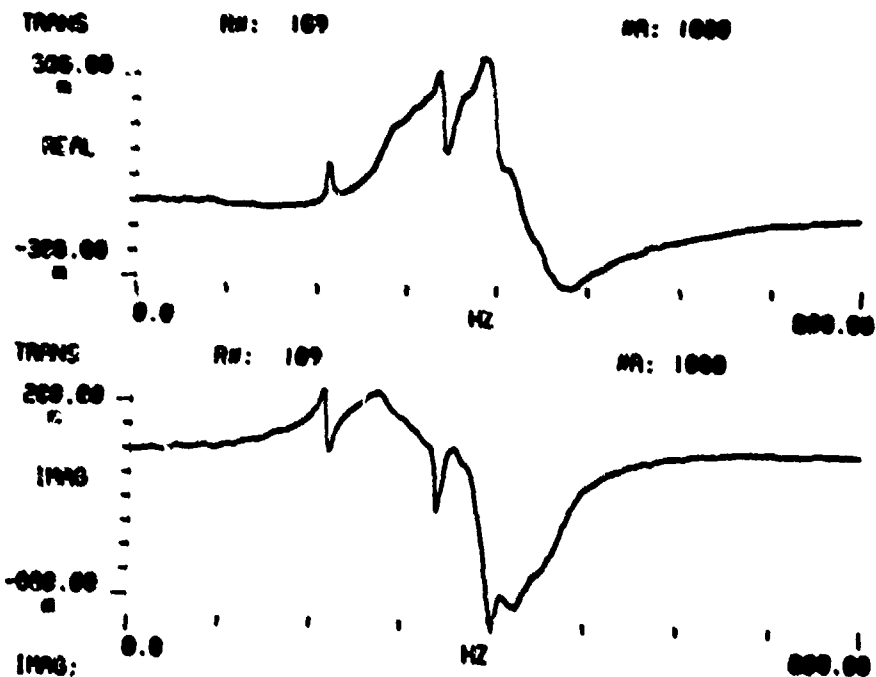
Figure 7. Tail vertical driving point acceleration
mobility (frequency 0-800 Hz).

35

MODAL TRANSFORMATION

COMPLEX MODES TO REAL MODES

The AH-1G airframe is characterized by nonproportional damping; as a result, it exhibits complex modes. The orthonormal mode shapes extracted from test data were complex, displaying imaginary portions of considerable significance. However, the NASTRAN model of the AH-1G that was used in the analysis considers only the undamped situation in the extraction of modal parameters yielding the classical normal mode or orthonormal mode shapes. Thus, the elements of each mode are scalar quantities containing no relative phase angle information among the modal elements. Consequently, to qualitatively and quantitatively compare the complex modes developed from test data with the real modes computed from the NASTRAN model of the AH-1G, the complex modes extracted from test measurements required transformation to the real form. This process of converting complex modes to real modes compromises the physical realities of the structure but is necessary if a comparison of analytical and test results is to be effected. The technique which was implemented for conversion of the complex modes to real modes is a judgemental process based on a reference phase angle. Let Ψ_{jk} be the jth element of the kth complex mode, Ψ.

The complex representation of a modal element is

$$\Psi_j = a_j + i\, b_j$$

where $i = \sqrt{-1}$

The modal element can also be represented by a magnitude and a phase angle

$$\Psi_j = \sqrt{a_j^2 + b_j^2}\ e^{i\theta_j}$$

where $\theta_j = \tan^{-1} \dfrac{b_j}{a_j}$ and $0° \le \theta \le 360°$.

36

Based on a review of test data the complex axes system was rotated 45°, as shown on Figure 8, to accommodate the transformation from complex modes to real modes.
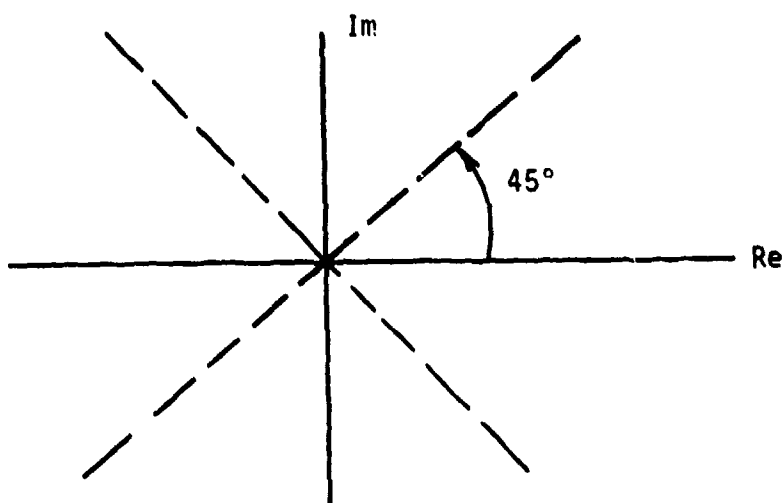
Figure 8.   Coordinate transformation.

The real representation of the complex modes was based on the following phase angle criteria

$$315° \leq \theta_j \leq 135° \qquad \psi_j = \sqrt{a_j^2 + b_j^2}$$

$$135° < \theta_j < 315° \qquad \psi_j = -\sqrt{a_j^2 + b_j^2}$$

TRUNCATED MODEL

The equation of motion of a linear structure can be written as

$$[M] \{\ddot{y}\} + [D] \{\dot{y}\} + [K] \{y\} = \{f\} \tag{13}$$

assuming a steady state solution of the form

$$\{y\} = \{\tilde{y}\}e^{i\omega t} \text{ and } \{f\} = \{\tilde{f}\}e^{i\omega t}$$

and substituting into equation (13) yields

$$\left[-[M]\omega^2 + i\omega[D] + [K] \right] \{\tilde{y}\} = \{\tilde{f}\} \tag{14}$$

Define the displacement impedance as

$$[Z] \equiv [Z^R] + [Z^I] = \left[[K] - \omega^2 [M] \right] + i \,\omega[D] \tag{15}$$

thus

$$[Z] \{\tilde{y}\} = \{\tilde{f}\}$$

The element displacement impedance can be expressed as

$$\left[z_{ij} \right] = \left(\partial\tilde{f}_i / \partial\tilde{y}_j \right)$$

The displacement impedance matrix defined in equation (15) can be premultiplied by $[\Phi]^{-T} [\Phi]^T$ and postmultiplied by $[\Phi] [\Phi]^{-1}$, where $[\Phi]$ is the matrix of modal vectors

$$[Z] = [\Phi]^{-T} \left[[\Phi]^T[K] [\Phi] - \omega^2 [\Phi]^T [M] [\Phi] + i\omega [\Phi]^T [D] [\Phi] \right] [\Phi]^{-1} \tag{16}$$

where $i = \sqrt{-1}$

Using the orthogonality characteristic of the normal modes, the diagonal generalized mass can be expressed as

$$[M^*] = [\Phi]^T [M] [\Phi] \qquad (17)$$

and the diagonal generalized stiffness can be expressed as

$$[K^*] = [\Phi]^T [K] [\Phi] \qquad (18)$$

assuming structural damping which is proportional to stiffness, where g is the structural damping coefficient, yields

$$[\Phi]^T [D] [\Phi] = [gK^*] \qquad (19)$$

Substituting equations (17), (18) and (19) into equation (16) gives

$$[Z] = [\Phi]^{-T} [K^* - \omega^2 M^* + i\, g\, K^*] [\Phi]^{-1} \qquad (20)$$

Define the modal displacement impedance matrix as

$$[Z^*] = [K^* - \omega^2 M^* + i\, g\, K^*] \qquad (21)$$

and when substituted into equation (20) yields

$$[Z] = [\Phi]^{-T} [Z^*] [\Phi]^{-1} \qquad (22)$$

The displacement mobility matrix at a forcing frequency ω has elements which represent the ratio of the displacement phasor along coordinate j to the applied force phasor along coordinate k when the applied forces at all other coordinates are zero. The full displacement mobility matrix is defined as

$$[Y] \equiv [Z]^{-1} \qquad (23)$$

39

and can be obtained from equation (22), thus

$$[Y] = [\Phi] \left\lceil \frac{1}{Z*} \right\rfloor [\Phi]^T \equiv [\Phi] \lceil Y* \rfloor [\Phi]^T \qquad (24)$$

with force excitation applied at a particular coordinate k the response
at each station of interest j can be obtained yielding a column of the
displacement mobility given in equation (24), thus

$$\left\{ Y_{j(k)} \right\}_{exact} = [\Phi] \left\{ Y*\Phi_{(k)i} \right\} = \sum_{i=1}^{\infty} Y*_i \Phi_{(k)i} \{\Phi\}_i \qquad (25)$$

As indicated in equation (25), the exact displacement mobility of a physi-
cal structure is obtained only by considering an infinite number of nor-
mal modes. Practical considerations, however, restrict the number of
normal modes that can be used in an analysis.

A truncated model of a linear system can be formed by considering fewer
normal modes than degrees of freedom associated with the physical sys-
tem. If the number of normal modes is limited, the displacement mobility
becomes

$$\left\{ Y_{j(k)} \right\} = [\Phi] \left\{ Y*\Phi_{(k)i} \right\} + \{\delta\} = \sum_{i=1}^{N} Y*_i \Phi_{(k)i} \{\Phi\}_i + \{\delta\} \qquad (26)$$

where $\{\delta\}$ represents the difference between the actual displacement
mobility and the approximation using only N normal modes.

A truncated model of a linear system is comprised of the constant coef-
ficient matrices in the equation of motion formed using fewer normal
modes than degrees of freedom such that the scalar product of $\{\delta\}^T \{\delta\}$ is
minimized with respect to the modal coefficients $\{Y*\}$. Using equa-
tion (26), the vector representing the difference between the exact and
the approximation to the displacement mobility can be written as

$$\{\delta\} = \left\{ Y_{j(k)} \right\} - [\Phi] \lceil \Phi_{(k)i} \rfloor \{Y*\} \qquad (27)$$

40

and the transpose of $\{\delta\}$ becomes

$$\{\delta\}^T = \left\{Y_{j(k)}\right\}^T - \{Y^*\}^T \left[\, \Phi_{(k)i} \, \right] [\Phi]^T \tag{28}$$

finally

$$\{\delta\}^T \{\delta\} = \left\{Y_{j(k)}\right\}^T \left\{Y_{j(k)}\right\} - \left\{Y_{j(k)}\right\}^T [\Phi] \left[\, \Phi_{(k)i} \, \right] \{Y^*\}$$

$$- \{Y^*\}^T \left[\, \Phi_{(k)i} \, \right] [\Phi]^T \left\{Y_{j(k)}\right\}$$

$$+ \{Y^*\}^T \left[\, \Phi_{(k)i} \, \right] [\Phi]^T [\Phi] \left[\, \Phi_{(k)i} \, \right] \{Y^*\} \tag{29}$$

Equation (29) is a scalar product and the derivative of a scalar with
respect to a vector is also a vector. Thus, the modal vector $\{Y^*\}$ must
be obtained which will minimize the scalar product presented in
equation (29). This can be accomplished by differentiating the scalar
product, equation (29), with respect to the modal displacement mobility
vector and equating the result to zero as follows:

$$\frac{\partial \left[\{\delta\}^T \{\delta\} \right]}{\partial \{Y^*\}} = 0 = -2\left[\, \Phi_{(k)i} \, \right][\Phi]^T \left\{Y_{j(k)}\right\} + 2\left[\, \Phi_{(k)i} \, \right][\Phi]^T [\Phi]\left[\, \Phi_{(k)i} \, \right]\{Y^*\} \tag{30}$$

Solving for the modal displacement vector for which the scalar product is
a minimum yields

$$\{Y^*\} = \left[\, \Phi_{(k)i} \, \right]^{-1} \left([\Phi]^T [\Phi] \right)^{-1} [\Phi]^T \left\{Y_{j(k)}\right\} \tag{31}$$

or

$$\{Y^*\} = \left[\, \Phi_{(k)i} \, \right]^{-1} [\Phi]^+ \left\{Y_{j(k)}\right\}$$

The matrix $[\Phi]^+$ is commonly referred to as the generalized inverse or
pseudoinverse of $[\Phi]$ and is defined by

$$[\Phi]^+ \equiv \left([\Phi]^T [\Phi] \right)^{-1} [\Phi]^T \tag{32}$$

41

Equation (31) may be rewritten as

$$\lceil \Phi_{(k)i} \rfloor \{Y*\} = \lceil Y* \rfloor \{\Phi_{(k)i}\} = [\Phi]^+ \{Y_{j(k)}\} \qquad (33)$$

For the full displacement mobility matrix equation (26) becomes

$$[Y] = [\Phi] \lceil Y* \rfloor [\Phi]^T + [\delta] \qquad (34)$$

and equation (33) can be extended to

$$\lceil Y* \rfloor = [\Phi]^+ [Y] [\Phi]^{+T} \qquad (35)$$

Equation (35) can be premultiplied by $[\Phi]$ and postmultiplied by $[\Phi]^T$ to define the truncated mobility matrix as

$$[Y]_{TR} \equiv [\Phi] \lceil Y* \rfloor [\Phi]^T = [\Phi] [\Phi]^+ [Y] [\Phi]^{+T} [\Phi]^T \qquad (36)$$

The truncated impedance matrix is given as

$$[Z]_{TR} = [\Phi]^{+T} \lceil \frac{1}{Y*} \rfloor [\Phi]^+ = [\Phi]^{+T} \lceil Z* \rfloor [\Phi]^+ \qquad (37)$$

The truncated matrices are of order J, the number of coordinates of interest, and rank N, the number of modes considered, and are therefore singular.

If the product of $[Y]_{TR} [Z]_{TR}$ is premultiplied by $[\Phi]^+$ and postmultiplied by $[\Phi]$, the result is

$$[\Phi]^+ [Y]_{TR} [Z_{TR}] [\Phi] = I \qquad (38)$$

and

$$[\Phi]^T [Z]_{TR} [Y]_{TR} [\Phi]^{+T} = I$$

42

The mass, stiffness, and damping matrices for the truncated model are

$$[M]_{TR} = [\Phi]^{+T} \lceil M^* \rfloor [\Phi]^+$$

$$[K]_{TR} = [\Phi]^{+T} \lceil K^* \rfloor [\Phi]^+ \qquad (39)$$

$$[D]_{TR} = [\Phi]^{+T} \lceil gK^* \rfloor [\Phi]^+$$

The influence coefficient matrix for the truncated model is given by

$$[C]_{TR} = [\Phi] \lceil \frac{1}{K^*} \rfloor [\Phi]^T \qquad (40)$$

The classical modal eigenvalue equation for the truncated model be-comes

$$[C]_{TR} [M]_{TR} \{\Phi\} = \frac{1}{\Omega_i^2} \{\Phi\} \qquad (41)$$

Mass and Stiffness Changes

The displacement of J points on a structure can be written approximately as a function of N modal vectors, thus

$$\{y\} = [\Phi] \{q\} \qquad (42)$$

and the velocity becomes

$$\{\dot{y}\} = [\Phi] \{\dot{q}\} \qquad (43)$$

The kinetic energy of the structure can be written as

$$T = \frac{1}{2} \{\dot{y}\}^T [M] \{\dot{y}\} \qquad (44)$$

43

or using equation (43)

$$T = \frac{1}{2} \{\dot{q}\}^T [\phi]^T [M] [\phi] \{\dot{q}\} = \frac{1}{2} \{\dot{q}\}^T \lceil M^* \rfloor \{\dot{q}\} \qquad (45)$$

Using equation (39) the kinetic energy becomes

$$T = \frac{1}{2} \{\dot{q}\}^T [\phi]^T [M]_{TR} [\phi] \{\dot{q}\} \qquad (46)$$

Consider a structural mass and stiffness change wherein the resulting displacements, in the frequency range of interest, can be expressed approximately by

$$\{y\} = [\phi] \{r\} \qquad (47)$$

The kinetic energy for the modified structure can be expressed approximately as

$$T = \frac{1}{2} \{\dot{r}\}^T [\phi]^T \left([M] + [\Delta M] \right) [\phi] \{\dot{r}\} \qquad (48)$$

which upon expansion becomes

$$T = \frac{1}{2} \{\dot{r}\}^T [\phi]^T [M][\phi] \{\dot{r}\} + \frac{1}{2} \{\dot{r}\}^T [\phi]^T [\Delta M][\phi] \{\dot{r}\} \qquad (49)$$

Considering only the portion of the equation which contains the modification in the mass

$$[\phi]^T[\Delta M][\phi] = \left([\phi]^T[\phi] \right)^T \left([\phi]^T[\phi] \right)^{-T} [\phi]^T[\Delta M][\phi] \left([\phi]^T[\phi] \right)^{-1} \left([\phi]^T[\phi] \right)$$

$$[\phi]^T[\Delta M][\phi] = [\phi]^T[\phi]^{+T}[\phi]^T [\Delta M][\phi][\phi]^+ [\phi] \qquad (50)$$

Defining $\Delta M_{TR} \equiv [\phi]^{+T}[\phi]^T[\Delta M][\phi][\phi]^+$ the kinetic energy becomes

$$T = \frac{1}{2} \{\dot{r}\}^T [\phi]^T \left([M]_{TR} + [\Delta M]_{TR} \right) [\phi] \{\dot{r}\} \qquad (51)$$

44

The potential energy of the structure is given approximately by

$$V = \frac{1}{2} \{r\}^T [\Phi]^T \Big([K] + [\Delta K]\Big) [\Phi]\{r\} \tag{52}$$

$$= \frac{1}{2} \{r\}^T [\Phi]^T \Big([K]_{TR} + [\Delta K]_{TR}\Big)[\Phi]\{r\}$$

where

$$[\Delta K]_{TR} \equiv [\Phi]^{+T}[\Phi]^T[\Delta K][\Phi][\Phi]^+$$

The truncated influence coefficient matrix for the modified structure is given by

$$[C_{MOD}]_{TR} = [\Phi] \Big\langle [\Phi]^T \Big([K]_{TR} + [\Delta K]_{TR}\Big) [\Phi] \Big\rangle^{-1} [\Phi]^T \tag{53}$$

and the eigenvalue equation which reflects the mass and stiffness changes is

$$[C_{MOD}]_{TR}[M_{TR} + \Delta M_{TR}][\Phi_{MOD}] = [\Phi_{MOD}] \left[\frac{1}{\Omega^2_{MOD}}\right] \tag{54}$$

Equations Using Orthonormal Mode Vectors

It is more convenient to use the orthonormal mode in the previous equations, thereby eliminating the effect of normalization on each mode. The orthonormal mode allows a comparison of the relative prominence of each mode. The orthonormal mode is defined as

$$\{\Psi\}^T_i [M]\{\Psi\}_i = 1 \tag{55}$$

For N modes this may be extended to

$$[\Psi]^T[M][\Psi] = [I] \tag{56}$$

The generalized mass associated with each mode can be written as

$$M_i^* = \{\phi\}_i^T [M]\{\phi\}_i \tag{57}$$

If equation (55) is multiplied by the generalized mass of the ith mode and compared to equation (57), the elements of the orthonormal mode shape become

$$\Psi_{ji} = \frac{\phi_{ji}}{\sqrt{M^*_i}} \tag{58}$$

or

$$\phi_{ji} = \sqrt{M^*_i} \; \Psi_{ji}$$

For N modes and J points of interest on the structure equation (58) may be expanded to

$$[\phi] = [\Psi] [\sqrt{M^*}] \tag{59}$$

Some fundamental matrix operations which will be used subsequently are

$$[\phi]^T = [\sqrt{M^*}][\Psi]^T$$

$$[\phi]^+ = \left([\sqrt{M^*}][\Psi]^T [\Psi][\sqrt{M^*}]\right)^{-1} [\sqrt{M^*}][\Psi]^T$$

$$[\phi]^+ = \left[\frac{1}{\sqrt{M^*}}\right] [\Psi]^T[\Psi]^{-1}[\Psi]^T = \left[\frac{1}{\sqrt{M^*}}\right] [\Psi]^+$$

where

$$[\Psi]^+ = \left([\Psi]^T[\Psi]\right)^{-1}[\Psi]^T$$

$$\left.\phi\right.^{+T} = [\Psi]^{+T}\left[\frac{1}{\sqrt{M^*}}\right] \tag{60}$$

If the above relationships are substituted into equation (36) the truncated mobility matrix becomes

$$[Y]_{TR} = [\Psi][\Psi]^{+}[Y][\Psi]^{+T}[\Psi]^{T}$$

$$= [\Psi][\ Y*M* \ ][\Psi]^{T} \tag{61}$$

and equation (37) becomes

$$[Z]_{TR} = [\Psi]^{+T}[\ \frac{Z*}{M*} \ ][\Psi]^{+} \tag{62}$$

The truncated mass, stiffness and damping matrices presented in equation (39) can be written as a function of the orthonormal modal matrices and become

$$[M]_{TR} = [\Psi]^{+T}[I][\Psi]^{+}$$

$$[K]_{TR} = [\Psi]^{+T}[\ \frac{K*}{M*} \ ][\Psi]^{+} \tag{63}$$

$$= [\Psi]^{+T}[\ \Omega^{2} \ ][\Psi]^{+}$$

$$[\supset]_{TR} = [\Psi]^{+T}[\ g\Omega^{2} \ ][\Psi]^{+}$$

The influence coefficient matrix, using the orthonormal mode matrix is

$$[C]_{TR} = [\Psi][\ \frac{M*}{K*} \ ][\Psi]^{T}$$

$$= [\Psi][\ \frac{1}{\Omega^{2}} \ ][\Psi]^{T} \tag{64}$$

The classical modal eigenvalue equation for the truncated model can be written as

$$[C]_{TR} \ulcorner M]_{TR}\{\Psi\} = \frac{1}{\Omega_{i}^{2}} \ \{\Psi\} \tag{65}$$

Considering the mass and stiffness changes to the structure

$$\Delta M_{TR} = [\Psi]^{+T}[\Psi]^T[\Delta M][\Psi][\Psi]^+$$

$$\Delta K_{TR} = [\Psi]^{+T}[\Psi]^T[\Delta K][\Psi][\Psi] \qquad (66)$$

The modified truncated influence coefficient matrix, in terms of the orthonormal mode matrix, is given by

$$[C_{MOD}]_{TR} = [\Psi] \left[[\Psi]^T \left([K]_{TR} + [\Delta K]_{TR} \right) [\Psi] \right]^{-1} [\Psi]^T \qquad (67)$$

and the eigenvalue equation which reflects the mass and stiffness changes is

$$[C_{MOD}]_{TR} \left[[M]_{TR} + [\Delta M]_{TR} \right] [\Psi_{MOD}] = [\Psi_{MOD}] \left\lfloor \frac{1}{\Omega^2}_{MOD} \right\rfloor \qquad (68)$$

TRUNCATED MODEL

COMPUTER EXPERIMENTS

Computer experiments were performed on mass and stiffness changes to
determine the number of degrees of freedom required to insure adequate
representation of the Truncated Model method described in Reference 4.
The computer experiments were conducted for mass and stiffness changes
individually and in combination. The computer experiments were per-
formed using computer codes developed for the IBM 360/50 D.O.S./V.S.
Computer System using the FORTRAN IV Language.

Truncated parameters of a linear system are defined herein as those con-
stant coefficient matrices in the equations of motion formed from fewer
orthonormal modes than degrees of freedom such that the Euclidean Norm
of the difference between the exact mobility matrix and the approxima-
tion to the mobility matrix, which is formed using the orthonormal modes,
generalized masses, and generalized stiffnesses, is minimum with respect
to the modal or generalized mobility. The mobility matrix consists of
elements which are defined generically as the partial derivative of the
response at coordinate i with respect to force excitation applied at
coordinate j while the applied force at all other coordinates is zero.

Development of the truncated model requires the structure's natural
frequencies, orthonormal modes and modal damping which charac-
terize the frequency spectrum of interest. The natural frequencies and
orthonormal mode shapes necessary to effect the truncated model of the
AH-1G airframe were generated from a 92 degree of freedom NASTRAN model.
The truncated model was developed using 92 degrees of freedom and 16
elastic modes which encompassed the frequency range of from 0 to 40 Hz.

---

4.   Flannelly, W. G., and Giansante, N., EXPERIMENTAL VERIFICATION OF
      SYSTEM IDENTIFICATION, Kaman Aerospace Corporation, Report Number
      R-1275, USAAMRDL TR-74-64, Eustis Directorate, U. S. Army Air Mobility
      Research and Development Laboratory, Fort Eustis, Virginia 23604,
      August 1974, AD 784190.

The procedure used in developing the truncated models used in the computer study is shown schematically in Figure 9. The 92 degree of freedom NASTRAN model presented in Reference 1 was modified to be compatible with the mass configuration of the baseline AH-1G helicopter airframe (S/N 57-15683), which was subjected to ground vibration tests. Additionally, the number of degrees of freedom was reduced to 92 to correspond with the locations of the accelerometers positioned on the airframe. A 92 degree of freedom truncated model was subsequently formed using the normal mode shapes, natural frequencies, and generalized masses extracted from the reduced NASTRAN model.

In generating the truncated model, the normal mode shapes obtained from the NASTRAN model were converted to orthonormal mode shapes. The orthonormal mode shape, which is the conventional normal mode shape normalized by the square root of the generalized modal mass, has physical significance and offers a convenient means of comparing the relative importance of the modal responses of a structure. In addition, the product of the transpose of the orthonormal mode vector and the orthonormal mode vector, which yields a scalar, provides a direct measure of the significance of a particular mode, since the numerically greater the product the more important the contribution of that mode to the overall response of the structure. On the contrary, the conventional normal mode shape, which depends on the normalizing station, has no physical significance and taken independently does not yield any information regarding the dynamic response characteristics of the structure.

As indicated in Figure 9, step 3, mass and/or stiffness changes were incorporated in the 92-degree-of-freedom truncated model. Each of the resulting models, which included particular mass changes and stiffness changes, either individually or in combination, became a baseline model that was used as a basis of comparison for the reduced truncated models developed subsequently which incorporated the same mass and/or stiffness change configuration. The reduced truncated models contained 50, 30,

```
┌─────────────────────────────────┐
│ 1.  DEVELOP 92 DOF, 16 ELASTIC  │
│     MODE MODEL OF AH-1G FROM     │
│              NASTRAN             │
└─────────────────────────────────┘
                 │
                 ▼
┌─────────────────────────────────────┐
│ 2.  DEVELOP 92 DOF TRUNCATED MODEL   │
│ USING MODE SHAPES, NATURAL FREQUENCIES│
│       GENERALIZED MASS FROM          │
│       AH-1G NASTRAN MODEL (1)        │
└─────────────────────────────────────┘
                 │
                 ▼
┌────────────────────────────────────────┐
│ 3.  INCORPORATE MASS AND/OR STIFFNESS CHANGES│
│     TO 92 DOF, 16 MODE ELASTIC MODEL DEVELOPED│
│     IN 2.  THESE MODELS BECOME BASELINE  │
│     MODELS USED AS A BASIS OF COMPARISON │
│     FOR REDUCED DEGREE OF FREEDOM MODELS │
│           DEVELOPED SUBSEQUENTLY         │
└────────────────────────────────────────┘
                 │
                 ▼
┌────────────────────────────────────────┐
│ 4.  USING THE TRUNCATED MODEL DEVELOPED IN 2│
│     SELECT DEGREES OF FREEDOM TO FORM REDUCED│
│ TRUNCATED MODELS, INCORPORATING THE SAME MASS│
│     AND/OR STIFFNESS CHANGES AS IN STEP 3│
└────────────────────────────────────────┘
```

Figure 9.   Schematic truncated model development.

and 20 degrees of freedom. The mass changes, stiffness changes, and combinations of mass and stiffness that were incorporated in the models are presented in Tables 2, 3, and 4, respectively. These mass and stiffness change configurations required the formation of 18 baseline models which were used to evaluate the number of degrees of freedom required in the reduced models to substantiate the Truncated Model methodology.

In developing the reduced truncated models, the mass and stiffness changes were applied at grid points corresponding to the grid points at which the same changes were incorporated in the 92 degree of freedom models. Reduced truncated models utilizing 50, 30, and 20 degrees of freedom were developed for the 18 baseline truncated models, and the number of modes retained varied from 5 to 16 modes.

Review of preliminary vibration shake test data of the AH-1G helicopter airframe indicated an absence of dynamic response in the longitudinal (fore and aft) direction for the frequency spectrum of interest. Reference 5 also showed a lack of longitudinal modes except for the pylon fore and aft mode and the main rotor mast longitudinal bending mode. Therefore, the modelling strategy in developing the reduced truncated models was to omit the longitudinal degrees of freedom, except for those associated with the main rotor mast. Generally, the grid points at which concentrated masses were located were also included in the reduced truncated models. Additionally, coordinates at which mass and/or stiffness changes were effected were retained in the reduced models. One further consideration in generating the truncated models was to include coordinates which were reasonably distributed throughout the structure rather than to include only the coordinates concentrated in a region of high dynamic response.

5.   Cronkhite, James D., and Berry, Victor L., CORRELATION OF THE AH-1G AIRFRAME TEST DATA WITH A NASTRAN MATHEMATICAL MODEL. NASA CR-145119, February 1976.

TABLE 2. MASS CHANGES FOR
COMPUTER EXPERIMENTS

Outboard wing stores removed

Inboard wing stores removed

Inboard and outboard wing stores removed

Mass added at c.g. location (1.296 lb sec^2/in.)

Blade and hub mass added at hub location (1.86 lb sec^2/in.)

Inboard and outboard wing stores removed, mass added at c.g. location, blade and hub mass added at hub location.

TABLE 3. STIFFNESS CHANGES FOR
COMPUTER EXPERIMENTS

Add lateral stiffness between grid points 4633T2, 4637T2
(4.56×10^5 lb/in.)

Add lateral stiffness between grid points 42245T2, 46445T2
(1×10^6 lb/in.)

Reduce lift link stiffness by 0.5×10^6 lb/in.

Add stiffness between grid points 4633T2, 4637T2 (4.56×10^5 lb/in.)

Add stiffness between grid points 40145, 52045 (8.17×10^4 lb/in.)

Add stiffness between grid points 40145, 52045 (1.61×10^5 lb/in.)

Add stiffness between grid points 40145, 52045 (2.16×10^5 lb/in.)

Add stiffness between grid points 42245T2, 46445T2 ($.5 \times 10^6$ lb/in.)

TABLE 4. MASS AND STIFFNESS CHANGES

Clean wing configuration
>Add stiffness between grid points 40145, 52045 (8.17×10^4 lb/in.)

Inboard and outboard wing stores removed, mass added at c.g. location, blade and hub mass added at hub location
>Add stiffness between grid points 40145, 52045 (8.17×10^4 lb/in.)

Inboard wing stores removed
>Add stiffness between grid points 42245T2, 46445T2 (0.5×10^6 lb/in.)

Inboard wing stores removed
>Add stiffness between grid points 40145, 52045 (8.17×10^4 lb/in.)

This procedure yields a rectangular modal matrix which can be reliably operated on using the pseudoinverse technique and which, in general, yields numerically stable and physically meaningful results. Distribution of coordinates for typical reduced truncated models having 50, 30, and 20 degrees of freedom for the AH-1G helicopter airframe in the clean wing configuration is presented in Table 5. In performing the computer experiments for a particular mass and/or stiffness change configuration, no attempt was made to optimize the reduced truncated models in relation to the 92 degree of freedom model incorporating the same mass and stiffness changes. However, engineering judgement was applied in selecting the reduced degrees of freedom used in any model.

One of the prime objectives of the Truncated Model methodology is to develop reduced models which can successfully predict the effects of changes in mass and stiffness of the structure. The reduced truncated model allows the rapid determination of variations in configuration and provides a means for evaluating a variety of structural changes in the interest of improving the dynamic response of the vehicle. In the computer experiments which were conducted, the success of a reduced truncated model in adequately predicting mass and stiffness changes was measured by comparing modal parameters obtained from the reduced truncated model with those obtained from the 92 degree of freedom baseline for the same mass and stiffness changes. The modal data which were compared included natural frequencies, generalized masses, and the orthonormal mode shapes in the frequency range of interest. Using the orthonormal mode shape criterion, a single numerical value was determined, for each mode of interest, which provided a basis of comparison of the effectiveness of the reduced truncated model. For a specific mass and stiffness change configuration this numerical value, which will be referred to as the Modal Correlation Number, was calculated for each mode as the summation of the differences between the orthonormal modal elements of the baseline 92 degree of freedom truncated model and the respective modal elements of the reduced truncated model divided by the number of degrees of freedom in the reduced truncated model. The Model Correlation Number,

TABLE 5.   REDUCED TRUNCATED MODELS
INBOARD, OUTBOARD WING STORES REMOVED

92 D.O.F. Index	Degree of Freedom Identification	50 D.O.F.	30 D.O.F.	20 D.O.F.
1	40141T3	x*	x	x
2	40142T3		x	x
4	38045T2	x	x	x
5	38045T3	x	x	x
6	33845T2	x		
7	33845T3	x		
9	40145T3	x		
10	42245T2	x	x	
11	42245T3		x	
14	46445T2	x	x	x
15	46445T3	x	x	x
17	48045T2	x	x	
18	48045T3	x	x	x
19	48845T2		x	x
20	49745T3		x	
23	52045T2	x	x	x
24	52045T3	x	x	x
26	200129T1	x	x	x
27	200129T2	x	x	x
29	200153T1	x	x	x
30	200153T2	x	x	x
33	124800T3	x		
35	25065T3	x		
36	19752T3	x		
37	19765T3	x		
39	25045T2	x		
40	26861T3	x		
41	26865T2	x		
42	26869T3	x		

* "x" Indicates degree of freedom used in the model

TABLE 5. CONTINUED

92 D.O.F. Index	Degree of Freedom Identification	50 D.O.F.	30 D.O.F.	20 D.O.F.
45	30045T3	X		
47	22703T2	X		
48	22725T3	X		
50	21325T2	X		
52	21341T3	X		
54	64229T3	X	X	X
57	65929T3	X	X	X
58	74229T3	X	X	X
61	75929T3	X	X	X
63	18635T2	X		
64	18625T3	X		
66	15625T2	X	X	
67	15629T3		X	
69	15621T3	X		
72	13843T2	X		
74	14809T2	X		
76	11563T3	X		
79	9371T3	X		
80	9363T2	X	X	
81	9331T3		X	
83	9333T2	X		
84	9339T3	X		
86	6167T2	X	X	X
87	6169T3	X	X	X
89	4661T3	X		
90	4633T2	X		
91	4637T2		X	
92	3331T3	X	X	

58

which is determined for each mode of interest, can be expressed algebraically as:

$$\text{MODAL CORRELATION NO.} = \epsilon_i = \left[\frac{1}{N} \sum_{j=1}^{N} \left(\Psi_{ji}{}_{92 \text{ D.O.F.}} - \Psi_{ji}{}_{RED}\right)^2\right]^{1/2}$$

In the above expression, $\Psi_{ji}{}_{92 \text{ D.O.F.}}$ represents the orthonormal modal element for the jth coordinate and the ith mode for the 92 degree of freedom truncated model for a particular mass/stiffness change configuration. The term $\Psi_{ji}{}_{RED}$ represents the corresponding orthonormal modal element for the reduced degree of freedom model. Thus, the Modal Correlation Number can be considered as representative of the average of the differences between the orthonormal mode elements obtained from the 92 degree of freedom baseline model and the corresponding modal elements calculated from a reduced degree of freedom truncated model.

Approximately 90 separate computer experiments were performed in the study. Table 6 presents results for typical reduced degree of freedom truncated models for the mass change configuration of inboard wing stores removed. A comparison of natural frequency and generalized mass is shown in Table 6a and 6b, respectively, for the 92 degree of freedom truncated model and the reduced truncated models with 50, 30 and 20 degrees of freedom. Data for the unmodified structure with inboard and outboard wing stores attached are also presented in the table. Removal of the inboard wing stores does not significantly change the fuselage natural frequencies. A comparison of the predicted natural frequencies shows excellent agreement among the models. A review of the generalized mass predictions indicates good agreement with the 92 degree of freedom baseline model except for the second mode in the 50 degree of freedom model, the first, second, and twelfth mode for the 30 and 20 degree of freedom modes, and the thirteenth mode for the 20 degree of freedom model. The lack of correlation for the aforementioned modes occurred because the coordinates displaying significant response for the modes of interest were omitted

TABLE 6. MASS CHANGE CONFIGURATION - INBOARD WING STORES REMOVED
30 AND 20 DOF MODELS CONTAIN NO DOF ON ROTOR MAST

a. Natural frequency comparison

Mode	w/Stores 92 D.O.F. Unmodified	Inboard Wing Stores Removed 92 D.O.F. Baseline	50 D.O.F.	30 D.O.F.	20 D.O.F.
1	4.18	4.33	4.33	4.33	4.33
2	5.12	5.12	5.12	5.12	5.12
3	6.87	6.90	6.90	6.90	6.90
4	8.02	8.11	8.11	8.11	8.11
5	12.39	12.39	12.39	12.39	12.39
6	15.75	16.35	16.35	16.35	16.35
7	16.37	16.84	16.84	16.85	16.84
8	18.85	18.97	18.96	18.96	18.97
9	20.60	21.09	21.09	21.09	21.10
10	23.93	23.96	23.96	23.97	23.97
11	24.70	24.74	24.74	24.72	24.72
12	27.62	27.65	27.65	27.66	27.65
13	29.95	29.94	29.95	29.95	29.96
14	31.06	31.07	31.06	31.07	31.02
15	33.13	33.23	33.23	33.24	33.23

b. Generalized mass comparison

Mode	w/Stores 92 D.O.F. Unmodified	Inboard Wing Stores Removed 92 D.O.F. Baseline	50 D.O.F.	30 D.O.F.	20 D.O.F.
1	1.089	1.017	1.017	8.587	8.583
2	0.842	0.842	1.812	6.782	6.825
3	0.404	0.408	0.408	0.408	0.408
4	0.732	0.709	0.709	0.709	0.709
5	7.524	7.537	7.534	7.533	7.577
6	3.242	0.885	0.886	0.886	0.884
7	0.832	2.582	2.583	2.588	2.595
8	2.831	3.510	3.507	3.470	4.829
9	2.754	2.767	2.767	2.765	2.764
10	4.575	4.709	4.714	4.753	4.708
11	2.751	2.777	2.779	2.766	2.793
12	1.506	1.484	1.484	5.708	5.724
13	2.369	2.404	2.378	2.355	3.601
14	1.796	1.835	3.44	3.525	3.236
15	1.172	1.159	1.159	1.159	1.158

from the model. Modes one and two are the main rotor pylon pitch and pylon roll modes, respectively; therefore, coordinates on the rotor mast in the longitudinal and lateral directions should be included in the models to satisfactorily predict the associated modal parameters. Modal data presented in Table 7 are also for the inboard wing stores removed configuration. The reduced truncated models for which the data were developed included coordinates on the rotor mast resulting in improved correlation of the modal parameters. However, as shown in Table 7b the generalized masses predicted for the eighth and thirteenth mode for the 20 degree of freedom truncated model lack agreement with the generalized masses predicted by other models for the corresponding modes. Further refinement of the coordinates selected for the model would, undoubtedly, provide improved correlation in the generalized masses for the aforementioned modes. The predicted natural frequencies are not particularly sensitive to the specific coordinates embodied in the specific models as long as the coordinates are reasonably distributed throughout the structure. Table 8 presents a review of the orthonormal mode shapes, in terms of the Modal Correlation Number, for the 50, 30, and 20 degree of freedom models. Generally, the degree of correlation for each mode decreases, as witnessed by an increase in the Modal Correlation Numbers, as the number of degrees of freedom in the model is reduced. Additionally, the ability to predict the higher frequency orthonormal mode shapes decreases as the model size decreases.

Modal data for the configuration with inboard and outboard wing stores removed are presented in Table 9. The data presented in Table 9a indicate excellent correlation for predicted natural frequency regardless of size or specific degrees of freedom contained in the model. Generalized mass data as shown in Table 9b are sensitive to the model size and, more particularly, dependent upon the coordinates included in the model. Specifically, the 50 degree of freedom model does not include coordinates required to define the second mode; therefore, there is no correlation of generalized mass compared to the 92 degree of freedom baseline model. Similarly, the 30 and 20 degree of freedom models do not predict satisfactorily the first

61

TABLE 7. MASS CHANGE CONFIGURATION - INBOARD WING STORES REMOVED
MODELS CONTAIN DOF ON ROTOR MAST

a. Natural frequency comparison

Mode	w/Stores 92 D.O.F. Unmodified	Inboard Wing Stores Removed			
		92 D.O.F. Baseline	50 D.O.F.	30 D.O.F.	20 D.O.F.
1	4.18	4.33	4.33	4.33	4.33
2	5.12	5.12	5.12	5.12	5.12
3	6.87	6.90	6.90	6.90	6.90
4	8.02	8.11	8.11	8.11	8.11
5	12.39	12.39	12.39	12.39	12.40
6	15.75	16.35	16.35	16.35	16.35
7	16.37	16.84	16.84	16.84	16.84
8	18.85	18.97	18.97	18.97	18.96
9	20.60	21.09	21.09	21.09	21.09
10	23.93	23.96	23.96	23.97	23.97
11	24.70	24.74	24.74	24.74	24.71
12	27.62	27.65	27.65	27.65	27.65
13	29.95	29.94	29.94	29.95	29.95
14	31.06	31.07	31.07	31.07	31.07
15	33.13	33.23	33.23	33.23	33.23

b. Generalized mass comparison

Mode	w/STORES 92 D.O.F. Unmodified	Inboard Wing Stores Removed			
		92 D.O.F. Baseline	50 D.O.F.	30 D.O.F.	20 D.O.F.
1	1.089	1.017	1.017	1.017	1.017
2	0.842	0.842	0.842	0.842	0.842
3	0.404	0.408	0.408	0.408	0.408
4	0.732	0.709	0.709	0.709	0.709
5	7.524	7.537	7.528	7.534	7.539
6	3.242	0.885	0.886	0.885	0.884
7	0.832	2.582	2.582	2.588	2.591
8	2.831	3.510	3.509	3.469	4.846
9	2.754	2.767	2.767	2.766	2.764
10	4.575	4.709	4.714	4.724	4.749
11	2.751	2.777	2.778	2.771	2.786
12	1.506	1.484	1.484	1.484	1.484
13	2.369	2.404	2.375	2.371	3.393
14	1.796	1.835	1.800	1.794	1.804
15	1.172	1.159	1.159	1.159	1.159

TABLE 8. MODAL CORRELATION NUMBERS
AH-1G 92 DOF TRUN MODEL
INBOARD WING STORES REMOVED

	Modal Correlation Numbers		
Mode No	50 D.O.F.	30 D.O.F.	20 D.O.F.
1	1.1398E-05	1.6446E-05	1.2684E-05
2	1.0834E-05	3.1038E-05	1.7606E-05
3	7.3745E-05	1.1379E-04	1.1564E-04
4	2.1504E-04	2.5062E-04	2.4844E-04
5	1.3904E-05	2.1723E-05	8.7160E-05
6	7.0850E-04	7.5913E-04	7.9816E-04
7	2.1655E-03	2.2494E-03	1.9935E-03
8	1.1842E-03	1.2631E-03	1.0259E-03
9	1.7968E-04	1.7109E-04	3.2246E-04
10	8.2326E-04	7.7938E-04	2.1052E-03
11	1.2275E-03	1.1383E-03	1.7857E-03
12	2.2285E-04	2.6249E-04	3.5256E-04
13	2.9074E-03	3.8075E-03	4.3400E-03
14	3.2571E-03	4.1353E-03	3.4196E-03
15	8.9115E-04	1.0828E-03	1.1774E-03

TABLE 9. MASS CHANGE CONFIGURATION
INBOARD, OUTBOARD WING STORES REMOVED
30 AND 20 DOF MODELS CONTAIN NO DOF ON ROTOR MAST

a. Natural frequency comparison

Mode	w/Stores 92 D.O.F. Unmodified	Inboard, Outboard Wing Stores Removed 92 D.O.F. Baseline	50 D.O.F.	30 D.O.F.	20 D.O.F.
1	4.18	4.57	4.57	4.57	4.57
2	5.12	5.12	5.12	5.12	5.12
3	6.87	6.95	6.95	6.95	6.95
4	8.02	8.19	8.19	8.20	8.19
5	12.39	12.41	12.41	12.41	12.41
6	15.75	16.57	16.57	16.57	16.57
7	16.37	17.99	17.99	17.99	17.98
8	18.85	22.26	22.25	22.26	22.28
9	20.60	23.17	23.17	23.17	23.16
10	23.93	24.63	24.63	24.63	24.62
11	24.70	28.00	27.86	27.89	27.87
12	27.62	28.20	28.18	28.19	28.18
13	29.95	30.41	30.42	30.51	30.41
14	31.06	31.21	31.20	31.23	31.24
15	33.13	33.30	33.30	33.31	33.30

b. Generalized mass comparison

Mode	w/Stores 92 D.O.F. Unmodified	Inboard, Outboard Wing Stores Removed 92 D.O.F. Baseline	50 D.O.F.	30 D.O.F.	20 D.O.F.
1	1.083	.922	.922	5.997	5.994
2	0.842	0.842	6.857	6.778	6.880
3	0.404	0.417	0.417	0.417	0.417
4	0.732	0.693	0.693	0.693	0.692
5	7.524	7.472	7.470	7.472	7.520
6	3.242	0.818	0.818	0.818	0.816
7	0.832	1.644	1.645	1.648	1.645
8	2.831	8.013	7.986	7.915	7.863
9	2.754	2.273	2.271	2.271	2.263
10	4.575	5.320	5.316	5.342	5.340
11	2.751	2.348	2.779	2.739	2.775
12	1.506	2.781	1.264	9.733	9.891
13	2.369	3.008	4.887	4.16	10.80
14	1.796	2.502	2.490	2.79	2.47
15	1.172	1.154	1.153	1.155	1.150

and second modes since the models lack modal participation of these modes as a result of the coordinates selected for the models. Table 10 presents data for models wherein the coordinates used include the effect of the modes in question. Consequently, the generalized masses predicted by the reduced models agree with those obtained from the 92 degree of freedom baseline model.

The ability of a model, with a particular coordinate configuration, to accurately predict the generalized mass of a specific mode must be evaluated with regard to the relative significance of that mode. The importance of any mode is directly proportional to the product of the transpose of the orthonormal mode and the orthonormal mode. Thus, the predictive capability of any model must be characterized by the ability to successfully determine the modal parameters associated with the significant modes in the frequency spectrum of interest.

Table 11 presents data for the first fuselage lateral bending orthonormal mode for the 50, 30, and 20 degree of freedom models and the corresponding modal elemental data which has been extracted from the 92 degree of freedom baseline model. Comparison of the modal data for reduced degree of freedom models with those from the 92 degree of freedom baseline model indicates excellent correlation for all models. Table 12 presents data similar to that given in Table 11, except the data is for the second fuselage vertical bending. Again, there is excellent agreement among the orthonormal elements of the reduced models compared to the 92 degree of freedom model. Thus, the 20 degree of freedom truncated model is a satisfactory representation of the actual structure with excellent modal predictive capability.

Modal data are presented in Table 13 for a stiffness change configuration realized by introducing a stiffening element having a spring rate of 8.17×10^4 lb/in. between grid points 40145 and 52045. Grid point 40145 is located on the tail boom at FS 401.33 in., BL 55.91 in., WL 0.0 in. and grid point 52045 is located on the vertical tail at FS 520.67 in., BL 118.27 in., and WL 0.0 in. Table 13a and 13b present natural frequency and

65

TABLE 10.   MASS CHANGE CONFIGURATION

INBOARD, OUTBOARD WING STORES REMOVED
MODELS CONTAIN DOF ON ROTOR MAST

a.   Natural frequency comparison

	w/Stores	Inboard, Outboard Wing Stores Removed			
	92 D.O.F.	92 D.O.F.	50 D.O.F.	30 D.O.F.	20 D.O.F.
Mode	Unmodified	Baseline			
1	4.18	4.57	4.57	4.57	4.57
2	5.12	5.12	5.12	5.12	5.12
3	6.87	6.95	6.95	6.95	6.95
4	8.02	8.19	8.19	8.19	8.19
5	12.39	12.41	12.41	12.41	12.41
6	15.75	16.57	16.57	16.57	16.57
7	16.37	17.99	17.99	17.99	17.99
8	18.85	22.25	22.26	22.25	22.24
9	20.60	23.17	23.17	23.17	23.16
10	23.93	24.63	24.63	24.63	24.62
11	24.70	28.00	27.86	27.86	27.87
12	27.62	28.20	28.18	28.18	28.18
13	29.92	30.41	30.42	30.42	30.41
14	31.06	31.21	31.21	31.21	31.21
15	33.13	33.30	33.30	33.30	33.30

b.   Generalized mass comparison

	w/Stores	Inboard, Outboard Wing Stores Removed			
	92 D.O.F.	92 D.O.F.	50 D.O.F.	30 D.O.F.	20 D.O.F.
Mode	Unmodified	Baseline			
1	1.089	0.922	0.922	0.922	0.922
2	0.842	0.842	0.842	0.842	0.842
3	0.404	0.417	0.417	0.417	0.417
4	0.732	0.693	0.693	0.693	0.693
5	7.524	7.472	7.470	7.471	7.476
6	3.242	0.818	0.818	0.818	0.818
7	0.832	1.644	1.645	1.645	1.647
8	2.831	8.013	7.997	7.986	7.664
9	2.754	2.273	2.271	2.270	2.256
10	4.575	5.320	5.328	5.323	5.414
11	2.751	2.348	2.727	2.698	2.655
12	1.506	2.731	1.261	1.259	1.259
13	2.369	3.008	3.086	3.070	3.074
14	1.796	2.502	2.512	2.503	2.502
15	1.172	1.154	1.154	1.153	1.156

66

TABLE 11. INBOARD, OUTBOARD WING STORES REMOVED
FIRST FUSELAGE LATERAL BENDING

ORTHONORMAL MODE

92 D.O.F. Element No.	92 D.O.F.	50 D.O.F.	30 D.O.F.	20 D.O.F.
1	-0.0383	-0.0383	-0.0383	-0.0383
2	-0.0209		-0.0209	-0.0209
4	-0.0324	-0.0324	-0.0324	-0.0324
5	0.0117	0.0117	0.0117	0.0117
6	-0.1338	-0.1338		
7	0.0078	0.0078		
9	0.0140	0.0140		
10	0.1491	0.1492	0.1491	
11	0.0166		0.0166	
14	0.4150	0.4150	0.4150	0.4150
15	0.0232	0.0232	0.0232	0.0232
17	0.6576	0.6576	0.6576	
18	0.0261	0.0262	0.0261	0.0261
19	0.8163		0.8163	0.8163
20	0.0295		0.0295	
23	1.5495	1.5495	1.5495	1.5495
24	0.0341	0.0343	0.0342	0.0341
26	-0.0046	-0.0046	-0.0045	-0.0045
27	0.0780	0.0780	0.0780	0.0780
29	-0.0109	-0.0108	-0.0108	-0.0108
30	0.1980	0.1980	0.1980	0.1980
33	-0.0017	-0.0017		
35	0.0029	0.0029		
36	0.0131	0.0131		
37	-0.0007	-0.0007		
39	-0.1439	-0.1439		
40	0.0189	0.0189		
41	-0.1729	-0.1729		
42	-0.0216	-0.0216		

TABLE 11.   CONTINUED.

92 D.O.F. Element No.	92 D.O.F.	50 D.O.F.	30 D.O.F.	20 D.O.F.
45	0.0047	0.0047		
47	-0.0775	-0.0775		
48	-0.0019	-0.0019		
50	-0.0729	-0.0729		
52	0.0262	0.0262		
54	0.0656	0.0656	0.0656	0.0656
57	0.0935	0.0935	0.0935	0.0935
58	-0.0673	-0.0673	-0.0673	-0.0672
61	-0.0956	-0.0956	-0.0956	-0.0956
63	-0.0256	-0.0256		
64	0.0006	0.0006		
66	0.0385	0.0385	0.0385	
67	-0.0194		-0.0194	
69	0.0218	0.0218		
72	0.0527	0.0527		
74	0.0629			
76	0.0115	0.0629		
79	0.0188	0.0188		
80	0.1350	0.1350	0.1350	
81	0.0189		0.0189	
83	0.1601	0.1601		
84	-0.0137	-0.0137		
86	0.2173	0.2173	0.2173	0.2173
87	-0.0094	-0.0094	-0.0095	-0.0095
89	0.0093	0.0093		
90	0.2600	0.2600	0.2600	
91	0.2600			
92	0.0060	0.0061	0.0060	

TABLE 12. INBOARD OUTBOARD WING STORES REMOVED
SECOND FUSELAGE VERTICAL BENDING
ORTHONORMAL MODE

92 D.O.F. Element No.	92 D.O.F.	50 D.O.F.	30 D.O.F.	20 D.O.F.
1	0.7799	0.7798	0.7798	0.7792
2	0.7173		0.7172	0.7169
4	0.1540	0.1540	0.1540	0.1533
5	0.6386	0.6385	0.6384	0.6384
6	0.0930	0.0930		
7	0.5089	0.5088		
9	0.6547	0.6546		
10	0.2030	0.2032	0.2034	
11	0.6167		0.6165	
14	0.2129	0.2132	0.2135	0.2122
15	0.3182	0.3181	0.3180	0.3180
17	0.1549	0.1551	0.1553	
18	0.1336	0.1335	0.1334	0.1337
19	0.1032		0.1035	0.1030
20	-0.0883		0.0885	
23	-0.1616	-0.1618	0.1620	0.1608
24	-0.4108	-0.4108	-0.4109	-0.4104
26	-0.0007	-0.0007	-0.0008	-0.0009
27	-0.0202	-0.0202	-0.0203	-0.0202
29	0.0096	0.0096	0.0096	0.0098
30	0.0077	0.0076	0.0007	0.0077
33	0.0932	0.0932		
35	0.1009	0.1009		
36	-0.1084	-0.1084		
37	-0.1115	-0.1115		
39	-0.0037	-0.0037		
40	0.1909	0.1908		
41	0.0074	0.0075		
42	0.1818	0.1818		

TABLE 12. CONTINUED.

92 D.O.F. Element No.	92 D.O.F.	50 D.O.F.	30 D.O.F.	20 D.O.F.
45	0.3405	0.3404		
47	-0.0052	-0.0052		
48	-0.0080	-0.0080		
50	-0.0142	-0.0142		
52	-0.0449	-0.0449	-0.1226	-0.1228
54	-0.1227	-0.1226	-0.1412	-0.1414
57	-0.1413	-0.1412	-0.1139	-0.1140
58	-0.1140	-0.1139	-0.1158	-0.1161
61	-0.1160	-0.1159		
63	-0.0187	-0.0187		
64	-0.1220	-0.1221		
66	-0.0107	-0.0107	-0.0108	
67	-0.1077		-0.1077	
69	-0.1088	-0.1088		
72	-0.0001	-0.0001		
74	-0.0099	-0.0099		
76	-0.0064	-0.0064		
79	0.1062	0.1062		
80	0.0472	0.0472	0.0473	
81	0.1426		0.1425	
83	0.0360	0.0360		
84	0.1808	0.1808		
86	0.0999	0.1000	0.1001	0.0992
87	0.4531	0.4531	0.4531	0.4529
89	0.5420	0.5420		
90	0.0797	0.0797	0.0800	
91	0.0798			
92	0.6536	0.6536	0.6536	

TABLE 13. STIFFNESS CHANGE CONFIGURATION - ADD STIFFNESS
8.17 x 10^4 lb/in. Between 40145 AND 52045
MODELS CONTAIN DOF ON ROTOR MAST

a. Natural frequency comparison

Mode	92 D.O.F. Unmodified	With Stiffness Change			
		92 D.O.F. Baseline	50 D.O.F.	30 D.O.F.	20 D.O.F.
1	4.18	4.18	4.18	4.18	4.17
2	5.12	5.27	5.27	5.27	5.27
3	6.87	6.87	6.87	6.87	6.87
4	8.02	12.36	12.36	12.36	12.36
5	12.39	12.86	12.86	12.86	12.86
6	15.75	16.31	16.31	16.31	16.31
7	16.37	17.62	17.62	17.62	17.61
8	18.85	20.60	20.60	20.60	20.60
9	20.60	23.57	23.57	23.57	23.60
10	23.93	24.38	24.38	24.38	24.38
11	24.70	27.60	27.60	27.60	27.61
12	27.62	28.88	28.88	28.89	28.89
13	29.95	30.87	30.87	30.87	30.87
14	31.06	32.86	32.68	32.68	32.68
15	33.13	41.34	41.34	41.34	41.34

b. Generalized mass comparison

Mode	92 D.O.F. Unmodified	With Stiffness Change			
		92 D.O.F. Baseline	50 D.O.F.	30 D.O.F.	20 D.O.F.
1	1.089	1.089	1.089	1.089	1.089
2	0.842	0.820	0.820	0.820	0.821
3	0.404	0.404	0.404	0.404	0.404
4	0.732	7.396	7.394	7.398	7.408
5	7.524	2.540	2.539	2.551	2.553
6	3.242	0.789	0.789	0.789	0.789
7	0.832	6.807	6.796	6.797	6.823
8	2.831	2.743	2.743	2.743	14.350
9	2.754	5.650	5.649	5.646	11.350
10	4.575	4.474	6.710	8.493	12.650
11	2.751	1.511	4.788	4.788	4.847
12	1.506	1.834	2.971	7.849	7.819
13	2.369	1.354	6.415	6.414	6.401
14	1.796	1.214	1.214	1.214	1.217
15	1.172	2.678	3.201	3.389	3.393

generalized mass data, respectively, for truncated models having 92, 50, 30, and 20 degrees of freedom. Additionally, modal data are given for the unmodified 92 degree of freedom model.

Natural frequencies derived from the reduced degree of freedom models are in excellent agreement with the natural frequencies predicted by the 92 degree of freedom baseline model. However, the 50 and 30 degree of freedom models yield generalized masses which correlate with those of the baseline model for the first eight modes and for the fourteenth mode while the 20 degree of freedom model generalized masses correlate with the first seven modes and for the fourteenth mode. The generalized masses associated with the remaining modes lack agreement with the baseline model, which indicates that the coordinates used in the reduced degree of freedom models lack adequate representation of the modes in question.

Table 14 presents first fuselage vertical bending modal data for the aforementioned stiffness change configuration for the 50, 30, and 20 degree of freedom models and, additionally, the corresponding modal elements for the 92 degree of freedom baseline model. The Modal Correlation Number for the first fuselage vertical mode associated with each reduced model is also shown in Table 14 to effect a comparison between modal correlation and the value of the Modal Correlation Number. A review of the data given in the table indicates excellent correlation of the modal elements obtained from the reduced models compared to the baseline 92 degree of freedom modal elements.

Table 15 presents data for a combination mass and stiffness change. The condition that is described is for the clean wing configuration with a strut type diagonal element having stiffness of 8.17×10^4 lb/in. added between grid points 40145 and 52045. Tables 15a and 15b show natural frequency and generalized mass predictions, respectively, which were obtained from the 92, 50, 30 and 20 degree of freedom truncated models in which the aforementioned mass and stiffness change combination was incorporated. Each of the reduced degree of freedom models predicted extremely accurately the natural

TABLE 14. STIFFNESS CHANGE CONFIGURATION - ADD STIFFNESS
8.17×10^4 lb/in between 40145 and 52045
FIRST FUSELAGE VERTICAL BENDING
ORTHONORMAL MODE

92 D.O.F. Element No.	92 D.O.F.	50 D.O.F.	30 D.O.F.	20 D.O.F.
4	-0.0141	-0.0141	-0.0147	-0.0152
5	0.4178	0.4178	0.4176	0.4177
8	-0.0097	-0.0097	-0.0097	-0.0097
9	0.4956	0.4956	0.4953	0.4952
10	0.0034	0.0034	0.0028	0.0021
11	0.5613	0.5613		
14	0.0198	0.0198	0.0191	0.0184
15	0.6264	0.6264	0.6260	0.6259
17	0.0343	0.0343		
18	0.6275	0.6275		
19	0.0377	0.0377		
22	0.0178	0.0178	0.0178	0.0178
23	0.0364	0.0364	0.0372	0.0383
24	0.5986	0.5986	0.5983	0.5982
25	-0.0890	-0.0890	-0.0889	
29	-0.0051	-0.0051	-0.0051	-0.0049
30	0.0142	0.0142	0.0143	0.0139
35	-0.0207	-0.0207		
36	-0.0870	-0.0870		
37	-0.0886	-0.0886	-0.0886	
39	-0.0128	-0.0128		
40	0.0170	0.0170		
41	-0.0129	-0.0129	-0.0130	-0.0131
42	0.0304	0.0304	0.0305	0.0307
45	0.1184	0.1184		
46	-0.0142	-0.0142		
47	-0.0144	-0.0144	-0.0145	

TABLE 14. CONTINUED

92 D.O.F. Element No.	D.O.F.	50 D.O.F.	30 D.O.F.	20 D.O.F.
48	-0.0679	-0.0679	-0.0678	
50	-0.0090	-0.0090		
52	-0.0857	-0.0857		
54	-0.1840	-0.1840	-0.1840	-0.1841
57	-0.2671	-0.2671	-0.2670	-0.2673
58	-0.1670	-0.1670	-0.1669	-0.1670
61	-0.2260	-0.2260	-0.2258	-0.2260
63	-0.0269	-0.0269		
64	-0.0266	-0.0766		
66	0.0057	0.0057	0.0057	
67	-0.0285		-0.0186	
69	0.0083	0.0083		
72	0.0058	0.0058		
74	0.0165	0.0165		
76	0.1332	0.1331		
79	0.2319	0.2319		
80	0.0475	0.0475	0.0478	
81	0.2603		0.2602	
83	0.0586	0.0586		
84	0.2471	0.2471		
86	0.0948	0.0948	0.0954	
87	0.4375	0.4375	0.4372	
89	0.5319	0.5319		
90	0.1083	0.1083	0.1090	0.1089
91	0.1084	0.1084	0.1091	0.1090
Modal Correlation Number		6.168×10^{-6}	3.674×10^{-4}	7.131×10^{-4}

10
B

TABLE 15. COMBINATION MASS, STIFFNESS CHANGE
MASS CONFIGURATION - CLEAN WING
STIFFNESS CONFIGURATION - ADD STIFFNESS
8.17×10^4 LB/IN. BETWEEN 40145 AND 52045
30 AND 20 DOF MODELS CONTAIN NO DOF ON ROTOR MAST

a. Natural frequency comparison

		Mass/Stiffness Change			
Mode	92 D.O.F. Unmodified	92 D.O.F. Baseline	50 D.O.F.	30 D.O.F.	20 D.O.F.
1	4.18	4.57	4.57	4.57	4.57
2	5.12	5.27	5.27	5.27	5.27
3	6.87	6.95	6.95	6.95	6.95
4	8.02	12.39	12.39	12.39	12.39
5	12.39	13.87	13.87	13.87	14.03
6	15.75	16.58	16.58	16.58	16.58
7	16.37	22.18	22.18	22.18	22.74
8	18.85	23.17	23.17	23.17	23.77
9	20.60	24.62	24.62	24.62	25.83
10	23.93	26.64	26.64	26.64	
11	24.70	28.18	28.18	28.19	
12	27.62	30.13	30.13	30.13	
13	29.95	30.91	30.91	30.91	
14	31.06	32.87	32.87	32.87	
15	33.13	41.97	41.97	41.97	

b. Generalized mass comparison

		Mass/Stiffness Change			
Mode	92 D.O.F. Unmodified	92 D.O.F. Baseline	50 D.O.F.	30 D.O.F.	20 D.O.F.
1	1.089	0.921	0.921	5.985	5.970
2	0.842	0.820	0.820	38.950	39.590
3	0.404	0.416	0.416	0.416	0.417
4	0.732	7.223	7.221	7.222	7.196
5	7.524	1.920	1.920	1.921	2.102
6	3.242	0.802	0.802	0.802	0.813
7	0.832	9.416	9.420	9.419	6.311
8	2.831	2.275	2.274	2.275	2.758
9	2.754	4.992	4.982	8.582	2.119
10	4.575	3.067	3.932	3.930	
11	2.751	1.293	9.430	9.399	
12	1.506	3.896	4.650	4.641	
13	2.369	1.403	6.692	11.51	
14	1.796	1.198	1.199	1.198	
15	1.172	2.797	3.463	3.462	

75

frequencies resultin from the combination of mass and stiffness change. The generalized masses, which are dependent upon the coordinates incorporated in the model, show a variation in correlation depending upon the mode under consideration. For example, the 30 degree of freedom model was not able to successfully predict the generalized masses associated with the first and second mode. This occurred because the model was deficient in coordinates located on the rotor mast and the first and second modes are the pylon pitch and pylon roll modes, respectively. Modal element data is presented in Table 16, and a comparison of the elements for the 50, 30, and 20 degree of freedom models with the data from the 92 degree of freedom model reveals excellent correlation.

TABLE 16.   COMBINATION MASS, STIFFNESS CHANGE
MASS CONFIGURATION - CLEAN WING
STIFFNESS CONFIGURATION - ADD STIFFNESS
8.17×10^4 lb/in. between 40145 and 52045
FIRST FUSELAGE VERTICAL BENDING
ORTHONORMAL MODE

92 D.O.F. Element No.	92 D.O.F.	50 D.O.F.	30 D.O.F.	20 D.O.F.
1	0.6382	0.6382		
4	0.0425	0.0425	0.0425	.0625
5	0.4622	0.4622	0.4622	.4511
6	0.0119	0.0118	0.0118	
7	0.2636	0.2636	0.2636	
8	-0.0278	-0.0278	-0.0278	-.0217
9	0.5575	0.5575	0.5575	.5385
10	0.0771	0.0770	0.0771	
11	0.6386	0.6386	0.6386	
14	0.1006	0.1005	0.1005	.1002
15	0.7199	0.7200	0.7199	.6815
17	0.0875	0.0874	0.0875	.0830
18	0.7216	0.7216	0.7216	.6898
22	0.0058	0.0058	0.0058	-.0007
23	-0.0485	-0.0484	-0.0485	-.0591
24	0.6861	0.6861	0.6861	.6599
25	-0.1392	-0.1392	-0.1392	
29	-0.0065	-0.0065		
30	-0.0060	-0.0060		
31	-0.1402	-0.1401		
33	-0.0630	-0.0630		
35	-0.0622	-0.0622		
37	-0.1377	-0.1377		
39	-0.0111	-0.0111		
40	-0.0131	-0.0131	-0.0131	-.0020
41	-0.0077	-0.0077	-0.0077	.0047
42	-0.0057	-0.0057	-0.0130	
43	-0.0070	-0.0070		
46	-0.0131	-0.0131		

TABLE 16.   CONTINUED.

92 D.O.F. Element No.	92 D.O.F.	50 D.O.F.	30 D.O.F.	20 D.O.F.
47	-0.0130	-0.0130	-0.0130	
48	-0.1096	-0.1096	-0.1096	
50	-0.0116	-0.0116		
52	-0.1244	-0.1244		
54	-0.1511	-0.1511	-0.1511	-.1498
57	-0.1661	-0.1661	-0.1661	-.1708
58	-0.1306	-0.1306	-0.1306	-.1344
61	-0.1278	-0.1277	-0.1278	-.1380
63	-0.0168	-0.0168	0.0168	
64	-0.1165	-0.1165	-0.1165	
66	0.0003	0.0003		
67	-0.0389	-0.0389		
72	0.0065	0.0065		
74	0.0047	0.0047		
76	0.1249	0.1249	0.1249	.1141
77	0.0206		0.0206	.0219
80	0.0354	0.0354		
81	0.2785	0.2785		.2917
86	0.0671	0.0672	0.0671	
87	0.5214	0.5213	0.5214	
89	0.6292	0.6282		
90	0.0667	0.0668		

INCOMPLETE MODEL

The Incomplete Model methodology provides a technique for correcting a dynamic analytical model of a structure based on natural frequencies and mode shapes developed from ground vibration tests of the structure. The analysis depends on a set of natural frequencies and mode shapes which the analytical models are required to predict and mass and stiffness analytical models which are representative of the structure such that small changes in the elements of each will yield the desired characteristics.

MASS MATRIX IMPROVEMENT

The approach taken in the Incomplete Model methodology is that the measured modes of a structure are correct and the analytical mass matrix is modified to satisfy the orthogonality relationship among the measured modes and the modified mass matrix.

Consider M_A an analytical mass matrix having n degrees of freedom and ψ a matrix containing m measured orthonormal modes each having n degrees of freedom, where $m < n$. The degrees of freedom must correspond to the points of measurement on the structure. In the situation considered herein M_A corresponds to the 92 degree of freedom mass matrix developed from the NASTRAN model of the AH-1G airframe and the modal matrix consists of modes developed from the accelerations measured at locations on the airframe corresponding to the same points of interest as used in the mass matrix. If ΔM represents the changes in the mass matrix required to satisfy the orthogonality relationship, then

$$\psi^T (M_A + \Delta M)\psi = I$$

or

$$\psi^T \Delta M\psi = I - m_a \tag{69}$$

Where m_A is the nondiagonal $\psi^T M_A \psi$. Equation (69) has an infinite number

79

of solutions; that is, there are an infinite number of ΔM matrices that will satisfy the system. It is possible to determine a ΔM which has a minimum Euclidean norm subject to the constraints established in equation (69). Following the procedure used in References 6 and 7, the function to be minimized is established as

$$\epsilon = ||M_A^{-1/2} \Delta M M_A^{-1/2}|| \tag{70}$$

Minimization of equation (70) results in a ΔM matrix which is a minimum in the weighted Euclidean sense.

Using Lagrangian multipliers, λ_{ij}, the constraints of equation (69) may be applied to the function to be minimized (equation 70). Thus, the following Lagrangian function may be written:

$$\beta = \epsilon + \sum_{i=1}^{m} \sum_{j=1}^{m} \lambda_{ij} \left[\Phi^T \Delta M \Phi - I + m_A \right]_{ij} \tag{71}$$

If equation (71) is differentiated with respect to each element of the ΔM matrix and the results are set equal to zero the minimization of equation (70) is effected within the constraints of equation (69). This process results in a matrix of partial derivatives given as

$$\frac{\partial \beta}{\partial \Delta M_{ij}} = 2 M_A^{-1} \Delta M M_A^{-1} + \psi \lambda^T \psi^T = 0 \tag{72}$$

Solving equation (72) for the ΔM matrix yields

$$\Delta M = -1/2 M_A \psi \lambda^T \psi^T M_A \tag{73}$$

6.   Berman, A., et al., IMPROVEMENT OF ANALYTICAL DYNAMIC MODELS USING MODAL TEST DATA. AAIAA/ASME/ASCE/AHS 21st Structures, Structural Dynamics and Materials Conference, May 12-14, 1980, Seattle, Washington.

7.   Baruch, M., and Bar Itzhock, I.Y., OPTIMAL WEIGHTED ORTHAGONALIZATION OF MEASURED MODES. AIAA Journal, vol. 16, No. 4, 1978, pp. 346-351.

where λ is a square matrix of order m whose elements λ_{ij} are the Lagrangian multipliers. Substituting equation (73) into equation (69) yields the solution for λ

$$\lambda = -2 \, m_A^{-1} \, (I - m_A) m_A^{-1} \tag{74}$$

When equation (74) is substituted into equation (73), the corrected mass matrix is given by

$$M = M_A + \Delta M = M_A + M_A \, \Psi \, m_A^{-1} \, (I - m_A) m_A^{-1} \, \Psi^T \, M_A \tag{75}$$

The corrected mass matrix, which is symmetrical, is consistent with the measured modes. The only matrix inversion required in the process is that of m_A, which is of the order of the measured modes.

STIFFNESS MATRIX IMPROVEMENT

In a similar manner, it is possible to correct the stiffness matrix using the natural frequencies and mode shapes developed from test results, the improved mass matrix, and the eigenvalue equation for the ith mode

$$[K - \omega_i^2 M] \, \Psi_i = 0 \tag{76}$$

In addition, three constraint equations are imposed on the improved stiffness matrix, including the eigenvalue equation for all the measured modes, the orthogonality relationship for the stiffness matrix, and the requirement for a symmetrical stiffness matrix. The constraint equations are given by

$$K\Psi - M\Psi\Omega^2 = 0 \tag{77}$$

$$\Psi^T K\Psi - \Omega^2 = \tag{78}$$

$$K - K^T = 0 \tag{79}$$

81

The function to be minimized is

$$\varepsilon = ||M^{-1/2} \Delta K M^{-1/2}|| \tag{80}$$

Lagrangian multipliers $\lambda_{k_{ij}}$, $\lambda_{o_{ij}}$ and $\lambda_{s_{ij}}$ may be used in conjunction with the stiffness matrix constraints of equations (77), (78) and (79), respectively. The resulting Lagrangian function is given by

$$\beta = \varepsilon + \sum_{i=1}^{n} \sum_{j=1}^{m} \lambda_{k_{ij}} (K\Psi - M\Psi\Omega^2)_{ij} \tag{81}$$

$$+ \sum_{i=1}^{n} \sum_{j=1}^{m} \lambda_{o_{ij}} (\Psi^T K \Psi - \Omega^2)_{ij} + \sum_{i=1}^{n} \sum_{j=1}^{n} \lambda_{s_{ij}} (K - K^T)_{ij}$$

Differentiating equation (81) with respect to the elements of the K matrix and setting the result to 0 yields

$$2M^{-1} \Delta K M^{-1} + \lambda_K \Psi^T + \Psi \lambda_o \Psi^T + \lambda_s - \lambda_s^T = 0 \tag{82}$$

Solving equation (82) for the required change in the stiffness matrix gives

$$\Delta K = K - K_A = 1/2 \, M \, [\lambda_K \Psi^T + \Psi \lambda_o \Psi^T + \lambda_s - \lambda_s^T] \tag{83}$$

Substituting for K in Equation (79) yields a solution for the quantity $(\lambda_s - \lambda_s^T)$ which, when substituted into equation (83), eliminates λ_s and results in

$$K \cdot K_A - 1/4 \, M \, [\Psi\lambda_K^T + \lambda_K \Psi^T) \, M - 1/4 \, M\Psi[\lambda_o + \lambda_o^T)\Psi M \tag{84}$$

Inserting equation (84) into the constraint equation (78) and using $\Psi^T M \Psi = I$ gives

$$(\lambda_o + \lambda^T) = 4(\Psi^T K_A \Psi - \Omega^2) - (\lambda_K^T M \Psi + \Psi^T M \lambda_K) \tag{85}$$

82

Equation (85) may be substituted into equation (84) and the result is

$$K = K_A - M\Psi(\Psi^T K_A \Psi - \Omega^2)\Psi^T M - 1/4 M\Psi \lambda_K^T (I - M\Psi\Psi^T)M$$

$$- 1/4 M(I - \Psi\Psi^T)M\lambda_K\Psi^T M \qquad (86)$$

This equation is substituted into the constraint equation (77), giving

$$M(I - \Psi\Psi^T M)\lambda_K = (I - M\Psi\Psi^T)K_A\Psi \qquad (87)$$

and its transpose is given by

$$\lambda_K^T(I - M\Psi\Psi^T)M = \Psi^T K_A(\Psi\Psi^T M - I) \qquad (88)$$

The quantities on the left side of equations (87) and (88) appear in equation (86); these substitutions result in the corrected stiffness matrix expressed as

$$K = K_A - (K_A\Psi\Psi^T M + M\Psi\Psi^T K_A) + M\Psi(\Psi^T K_A \Psi + \Omega^2)\Psi M \qquad (89)$$

83

MASS AND STIFFNESS CHANGES

An important criterion for evaluating the effectiveness of an analytical model developed from dynamic test data is its ability to predict the effect of mass and stiffness changes to the structure. To judge the usefulness of the Truncated and Incomplete Model methodologies, analytical models were developed from dynamic test data for the mass and stiffness configurations that were tested. A truncated model and an incomplete model were developed for the high gross weight, forward center-of-gravity configuration and were used as the baseline analytical models. Mass and stiffness changes were made to the analytical models and the results, in the form of modal data, were compared to similar data extracted from test results for the corresponding airframe configuration. Figure 10 presents a flow diagram representing the typical process which was used in applying the Truncated Model methodology regarding mass and stiffness changes. A flow diagram depicting implementation of the Incomplete Model methodology for mass and stiffness modifications to the AH-1G airframe is shown in Figure 11.

MASS CHANGES

Three gross weight configurations were tested during the program. However, since the high gross weight, forward center-of-gravity condition was used as the baseline, this allowed two mass change conditions to be implemented analytically. The two mass changes were:

1. High gross weight, forward center of gravity to mean gross weight:
   a. remove inboard wing stores
   b. add forward fuel, 357 lb
   c. add aft fuel, 276 lb

2. High gross weight, forward center of gravity to low gross weight:
   a. remove inboard, outboard wing stores
   b. add forward fuel, 429 lb
   c. add aft fuel, 354 lb

84
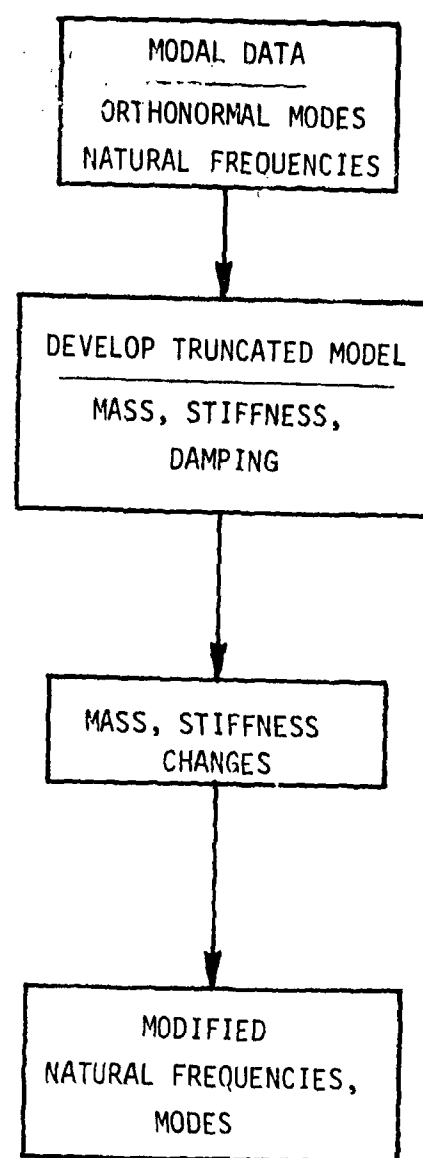
Figure 10.   Truncated model configuration change.
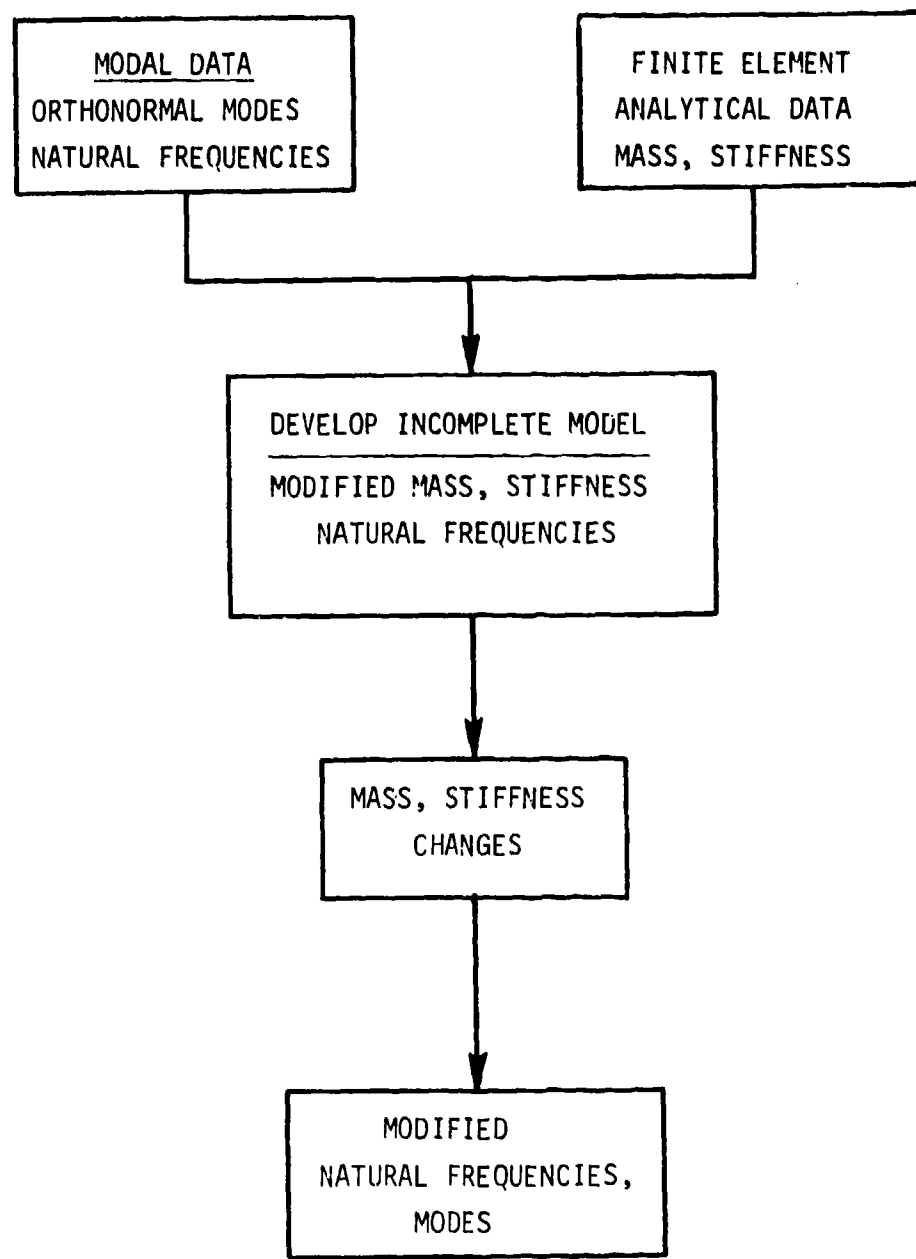
Figure 11.   Incomplete model configuration change.

The wing stores were considered to be concentrated masses rigidly attached to the wings at degrees of freedom corresponding to the NASTRAN model of the AH-1G and at which points accelerometers were located on the AH-1G airframe. The addition of fuel to the forward and aft fuel tanks in the test article was also treated as the addition of concentrated masses at grid points in the NASTRAN model which corresponded to accelerometers positioned geometrically proximate to the fuel tank locations on the AH-1G airframe. Since the fuel is a continuum, consideration of fuel changes as discrete impedance changes is extremely approximate. To investigate this effect many computer experiments were performed related to the manner of fuel and wing stores discretization. Tables 17, 18, and 19 represent typical data used for computer runs for mass changes in developing the high gross weight to low gross weight configuration. Similarly, Tables 20, 21, and 22 contain data used for generating the mean gross weight configuration from the high gross weight forward center of gravity baseline model.

TABLE 17.   MASS CHANGE - HIGH GROSS WEIGHT TO LOW GROSS WEIGHT

DOF	NASTRAN GRID IDENT.	MASS CHANGE LB-SEC^2/IN.	DESCRIPTION
47	22703T2	.917	Add AFT Fuel
48	22725T3	.917	Add AFT Fuel
54	64229T3	-1.370	Remove Inboard Wing Store, R.S
57	65929T3	- .997	Remove Outboard Wing Store. R.S
58	74229T3	-1.370	Remove Inboard Wing Store, L.S
61	75929T3	- .997	Remove Outboard Wing Store, L.S
66	15625T2	1.110	Add Forward Fuel
67	15629T3	.555	Add Forward Fuel
69	15621T3	.555	Add Forward Fuel

TABLE 18. MASS CHANGE - HIGH GROSS
WEIGHT TO LOW GROSS WEIGHT

DOF	NASTRAN GRID IDENT.	MASS CHANGE LB-SEC^2/IN.	DESCRIPTION
47	22703T2	.917	Add AFT Fuel
48	22725T3	.917	Add Aft Fuel
54	64229T3	-1.370	Remove Inboard Wing Store, R.S
57	65929T3	- .997	Remove Outboard Wing Store, R.S
58	74229T3	-1.370	Remove Inboard Wing Store, L.S
61	75929T3	- .997	Remove Outboard Wing Store, L.S
62	18645T1	1.110	Add Forward Fuel
63	18635T2	.4575	Add Forward Fuel
64	18625T3	.4575	Add Forward Fuel
66	15625T2	.6535	Add Forward Fuel
67	15629T3	.3268	Add Forward Fuel
69	15621T3	.3268	Add Forward Fuel

12
F

TABLE 19. MASS CHANGE - HIGH GROSS WEIGHT TO LOW GROSS WEIGHT

DOF	NASTRAN GRID IDENT.	MASS CHANGE LB-SEC^2/IN.	DESCRIPTION
47	22703T2	.917	Add AFT Fuel
48	22725T3	.917	Add Aft Fuel
55	65011T1	-2.367	Remove Inboard, Outboard Wing Stores, L.S
56	65011T3	-2.367	Remove Inboard, Outboard Wing Stores, L.S
59	75011T1	-2.367	Remove Inboard, Outboard Wing Stores, R.S
60	75011T3	-2.367	Remove Inboard, Outboard Wing Stores, R.S
62	18645T1	1.110	Add Forward Fuel
63	18635T2	.4575	Add Forward Fuel
64	18625T3	.4575	Add Forward Fuel
66	15625T2	.6535	Add Forward Fuel
67	15629T3	.3268	Add Forward Fuel
69	15621T3	.3268	Add Forward Fuel

TABLE 20. MASS CHANGE - HIGH GROSS
WEIGHT TO MEAN GROSS WEIGHT

DOF	NASTRAN GRID IDENT.	MASS CHANGE LB SEC^2/IN.	DESCRIPTION
47	22703T2	.715	Add AFT Fuel
48	22725T3	.715	Add Aft Fuel
54	64229T3	-1.370	Remove Inboard Wing Store, R.S
58	74229T3	-1.370	Remove Inboard Wing Store, L.S
66	15625T2	.925	Add Forward Fuel
67	15629T3	.4625	Add Forward Fuel
69	15621T3	.4625	Add Forward Fuel

TABLE 21. MASS CHANGE - HIGH GROSS
WEIGHT TO MEAN GROSS WEIGHT

DOF	NASTRAN GRID IDENT.	MASS CHANGE LB SEC^2/IN.	DESCRIPTION
47	22703T2	.715	Add AFT Fuel
48	22725T3	.715	Add AFT Fuel
54	64229T3	-1.370	Remove Inboard Wing Store, R.S.
58	74229T3	-1.370	Remove Inboard Wing Store, L.S.
62	18645T1	.925	Add Forward Fuel
63	18635T2	.381	Add Forward Fuel
64	18635T3	.381	Add Forward Fuel
66	15625T2	.544	Add Forward Fuel
67	15629T3	.272	Add Forward Fuel
69	15621T3	.272	Add Forward Fuel

TABLE 22.   MASS CHANGE - HIGH GROSS
WEIGHT TO MEAN GROSS WEIGHT

DOF	NASTRAN GRID IDENT.	MASS CHANGE LB SEC^2/IN.	DESCRIPTION
47	22703T2	.715	Add AFT Fuel
48	22725T3	.715	Add AFT Fuel
55	65011T1	-1.370	Remove Inboard Wing Store, L.S
56	65011T3	-1.370	Remove Inboard Wing Store, L.S
59	75011T1	-1.370	Remove Inboard Wing Store, R.S
60	75011T3	-1.370	Remove Inboard Wing Store, R.S
62	18645T1	.925	Add Forward Fuel
63	18635T2	.381	Add Forward Fuel
64	18635T3	.381	Add Forward Fuel
66	15625T2	.544	Add Forward Fuel
67	15629T3	.272	Add Forward Fuel
69	15621T3	.272	Add Forward Fuel

COMPARISON OF ANALYTICAL AND TEST RESULTS

INCOMPLETE MODEL - FREQUENCY RESPONSE

One measure of the success of an analytical dynamic model is its ability
to predict the dynamic response of a structure compared to test measure-
ments. The acceleration mobility, or accelerance, reflects the adequacy
of the analytical mass and stiffness matrices in duplicating test data
over a frequency band of interest. The acceleration mobility matrix for
a linear system is given as

$$[\ddot{Y}] = \left[[M - \frac{1}{\omega^2} K] - i \frac{g}{\omega} [K] \right]^{-1} \qquad (90)$$

The individual elements of the acceleration mobility matrix characterize
the response at the ith degree of freedom for force excitation at the
jth degree of freedom.

The Incomplete Model methodology was applied to the 92 degree of freedom
NASTRAN model to develop improved mass and stiffness matrices representa-
tive of the AH-1G airframe. Subsequently, equation (90) was used to
determine the acceleration mobility matrices of the system. In evaluating
the acceleration mobility of the structure at a particular forcing fre-
quency the value of the structural damping coefficient, g, must be speci-
fied. For frequencies of excitation proximate to the natural frequencies
the modal damping coefficient obtained from test measurements was used in
the analysis. However, use of the modal damping coefficients are theor-
etically valid only at the system natural frequencies. In the current
program at forcing frequencies off-resonance in the range of 9-13 Hz, a
linear distribution of structural damping was applied based on the modal
damping coefficients associated with the natural frequencies at 7.32 Hz
and 14.35 Hz. Additionally, for comparative purposes values of structural
damping of .05 and .10 were used for the same frequency band. Equation (90)
was used to develop acceleration mobility matrices for a frequency spectrum
of 5 Hz to 22 Hz. Typical frequency response curves are presented in
Figures 12, 13, 14, and 15 showing comparisons between the analytical

94
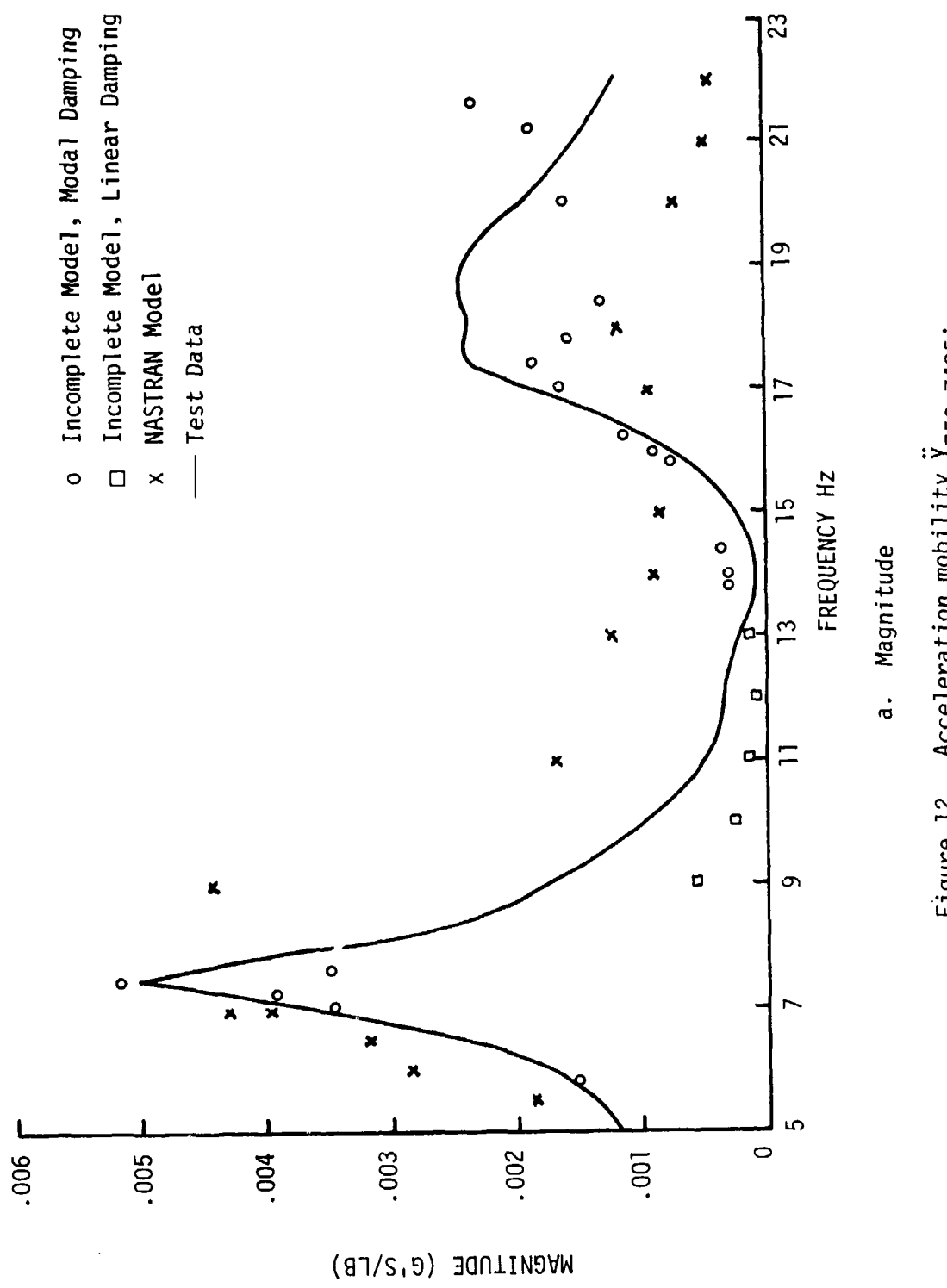
Figure 12. Acceleration mobility $\ddot{Y}_{Z50,Z485}$.

a. Magnitude

b. Phase angle

Figure 12. Continued.

o   Incomplete Model, Modal Damping
□   Incomplete Model, Linear Damping
x   NASTRAN Model
—— Test Data
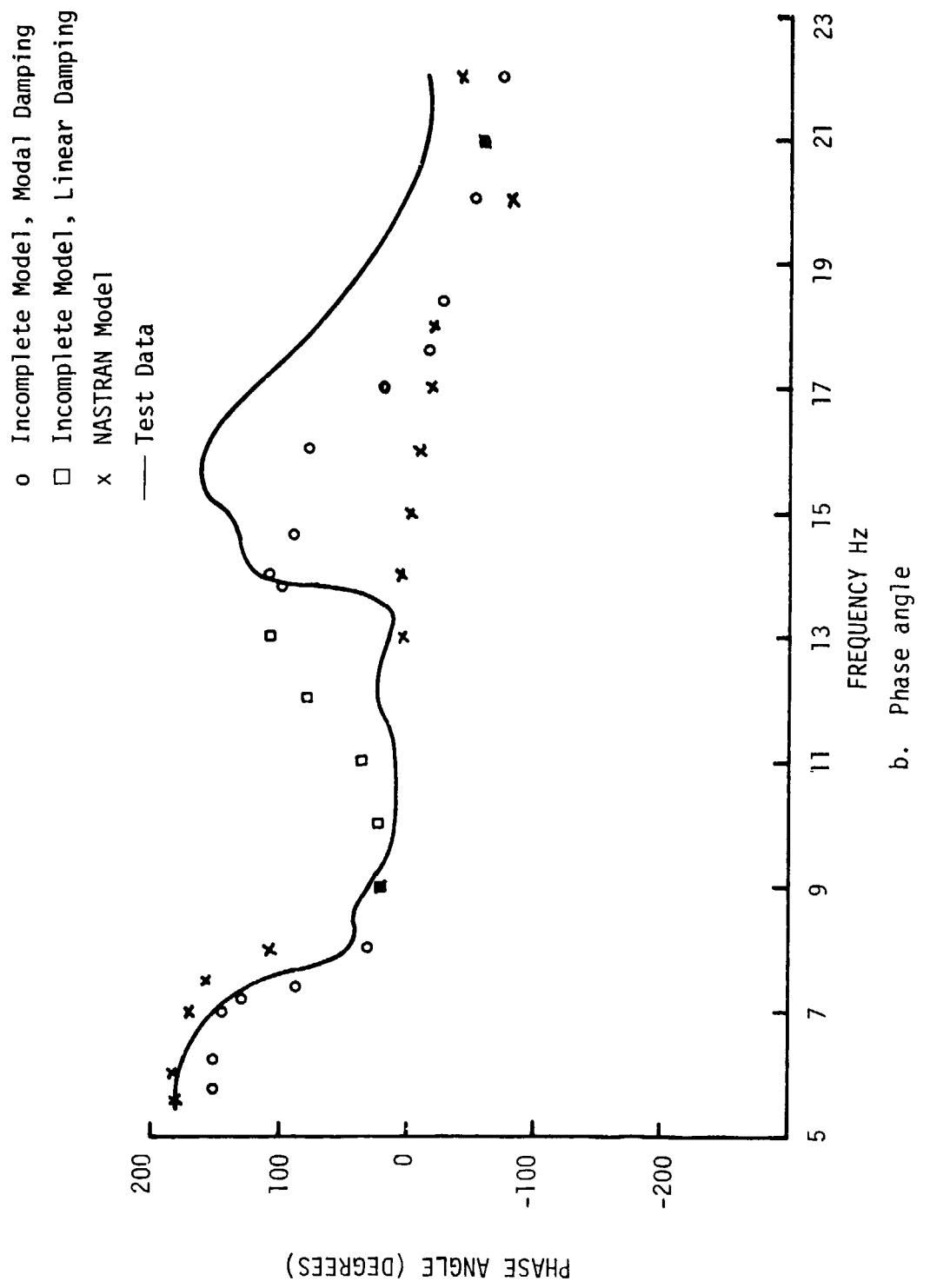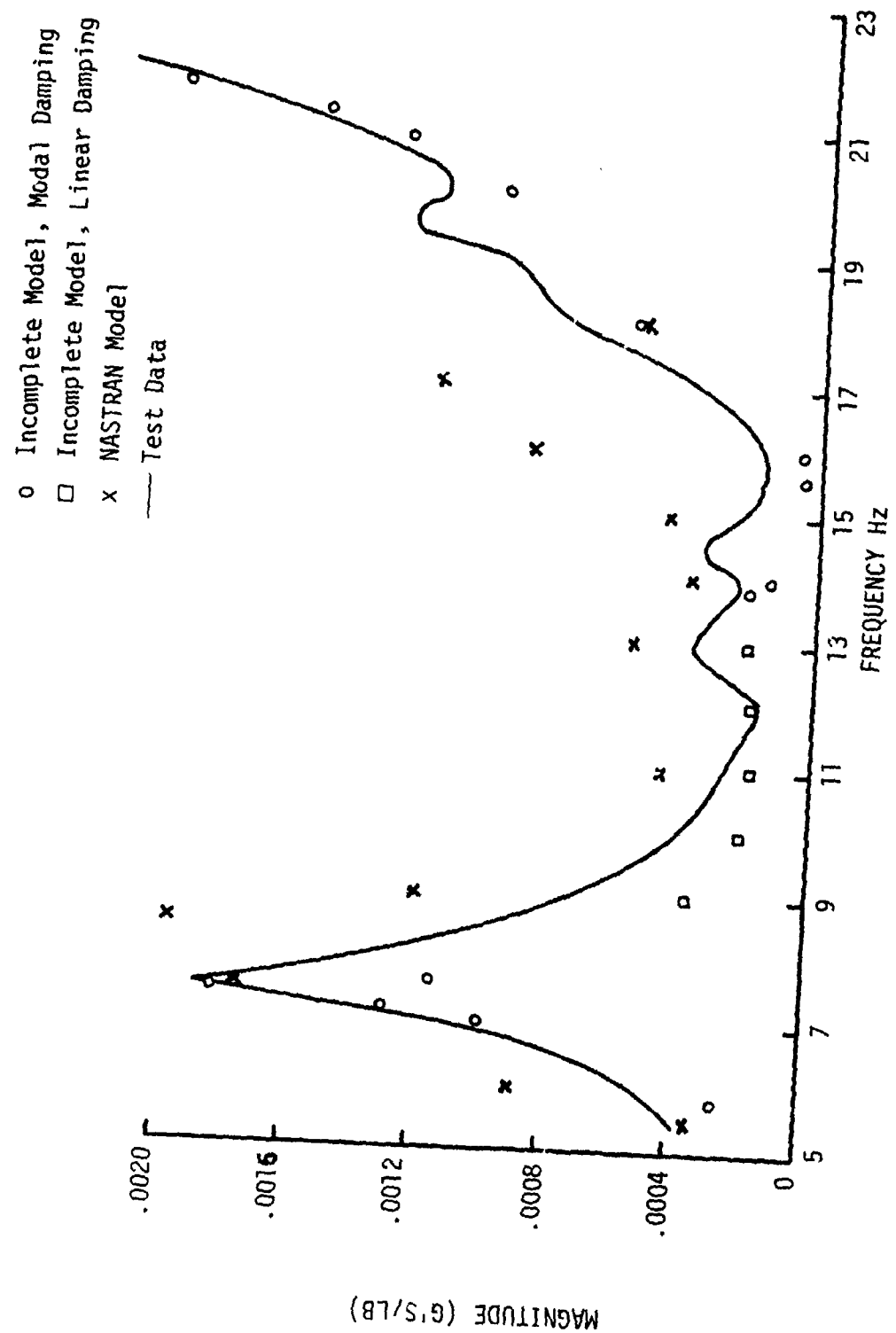
a. Magnitude

Figure 13. Acceleration mobility $\ddot{Y}_{Z202R,Z485}$.

MAGNITUDE (G'S/LB)

o Incomplete Model, Modal Damping
□ Incomplete Model, Linear Damping
x NASTRAN Model
— Test Data

FREQUENCY Hz

PHASE ANGLE (DEGREES)
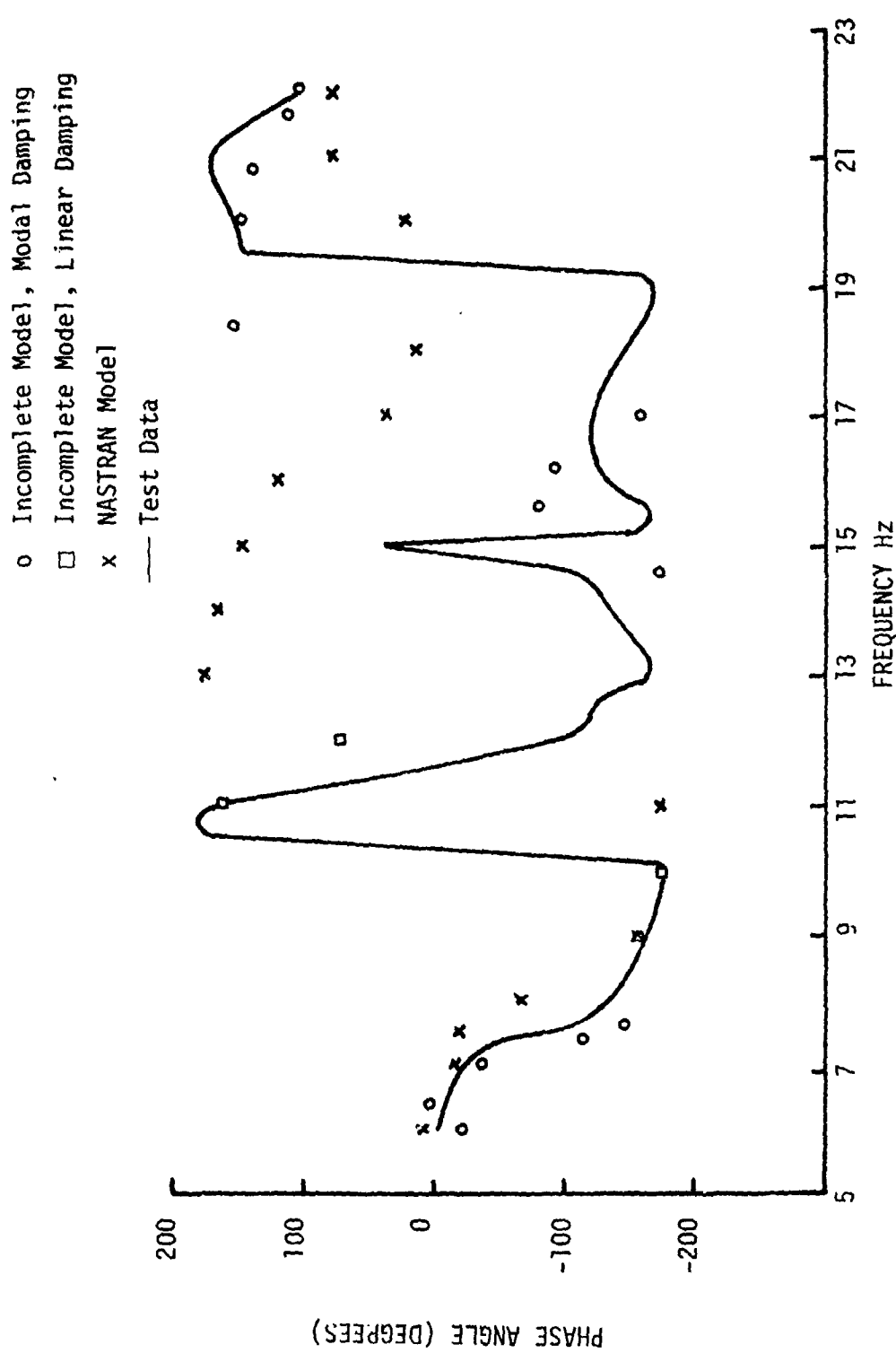
b. Phase angle

Figure 13. Continued.
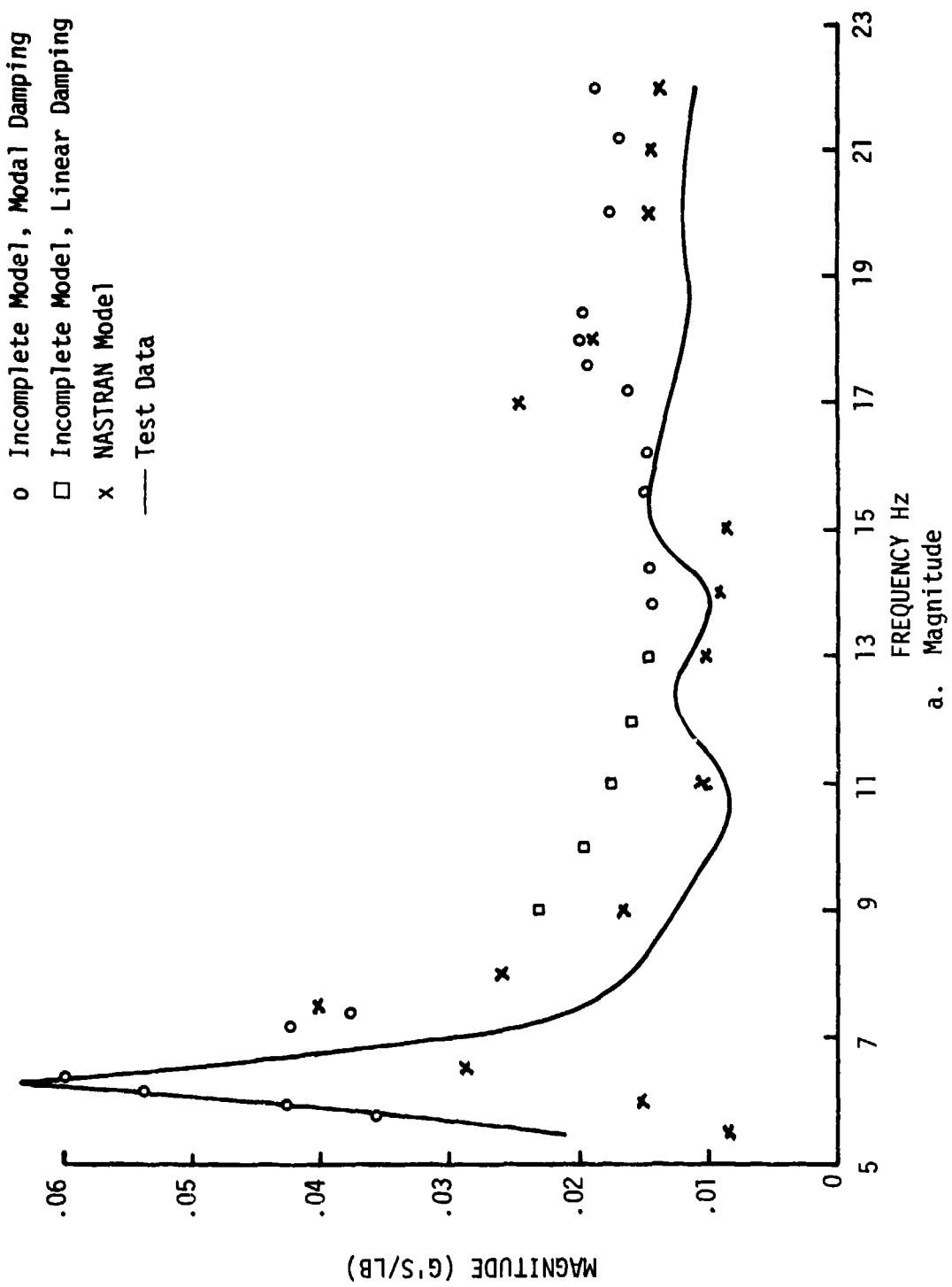
Figure 14. Acceleration mobility $\ddot{Y}_{Y521,Y521}$.

o Incomplete Model, Modal Damping
□ Incomplete Model, Linear Damping
x NASTRAN Model
— Test Data

FREQUENCY Hz
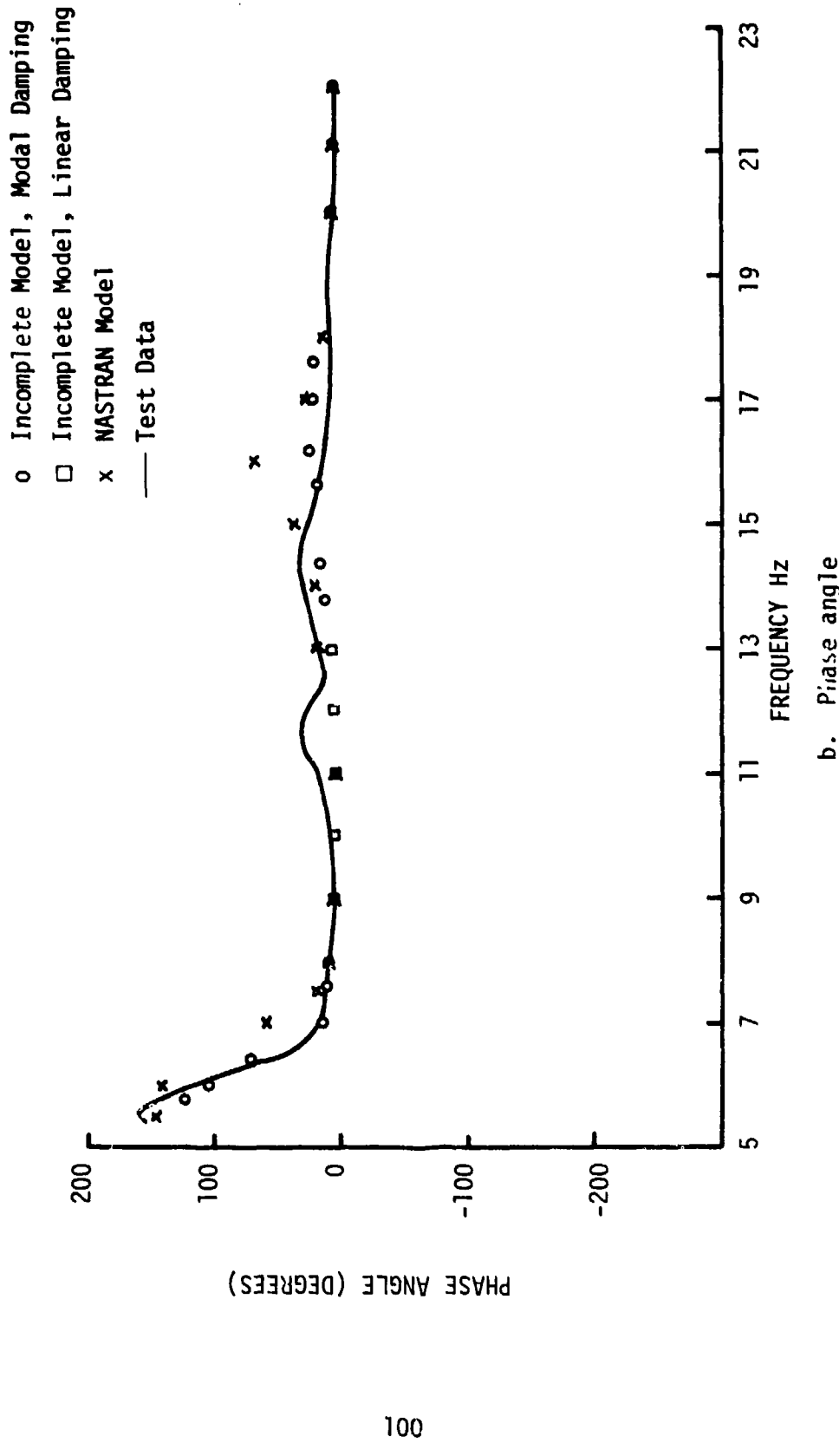
b. Phase angle

Figure 14. Continued.

PHASE ANGLE (DEGREES)
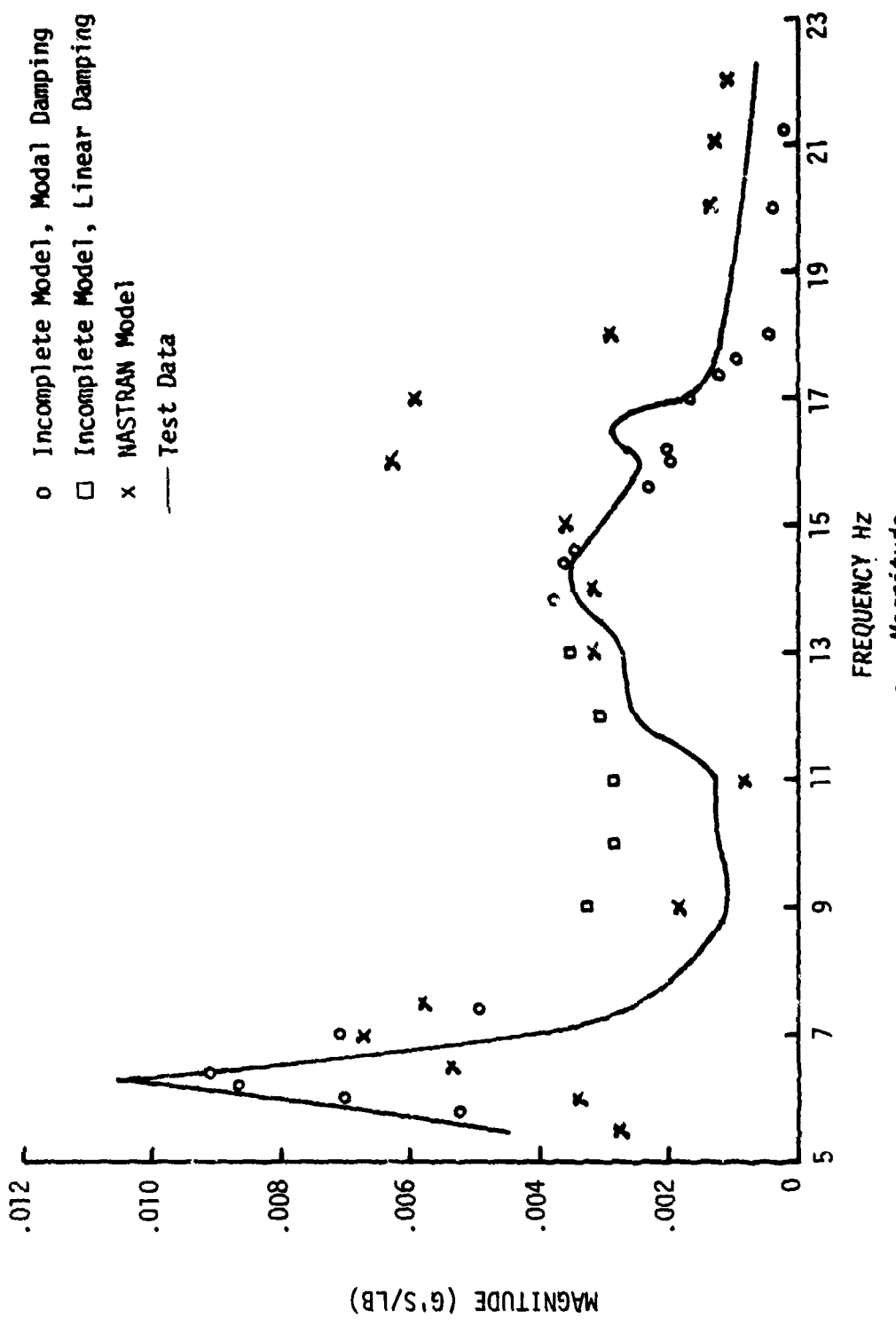
Figure 15. Acceleration mobility $\ddot{Y}_{Y46L,Y52I}$

o Incomplete Model, Modal Damping
□ Incomplete Model, Linear Damping
x NASTRAN Model
—— Test Data

FREQUENCY Hz

PHASE ANGLE (DEGREES)
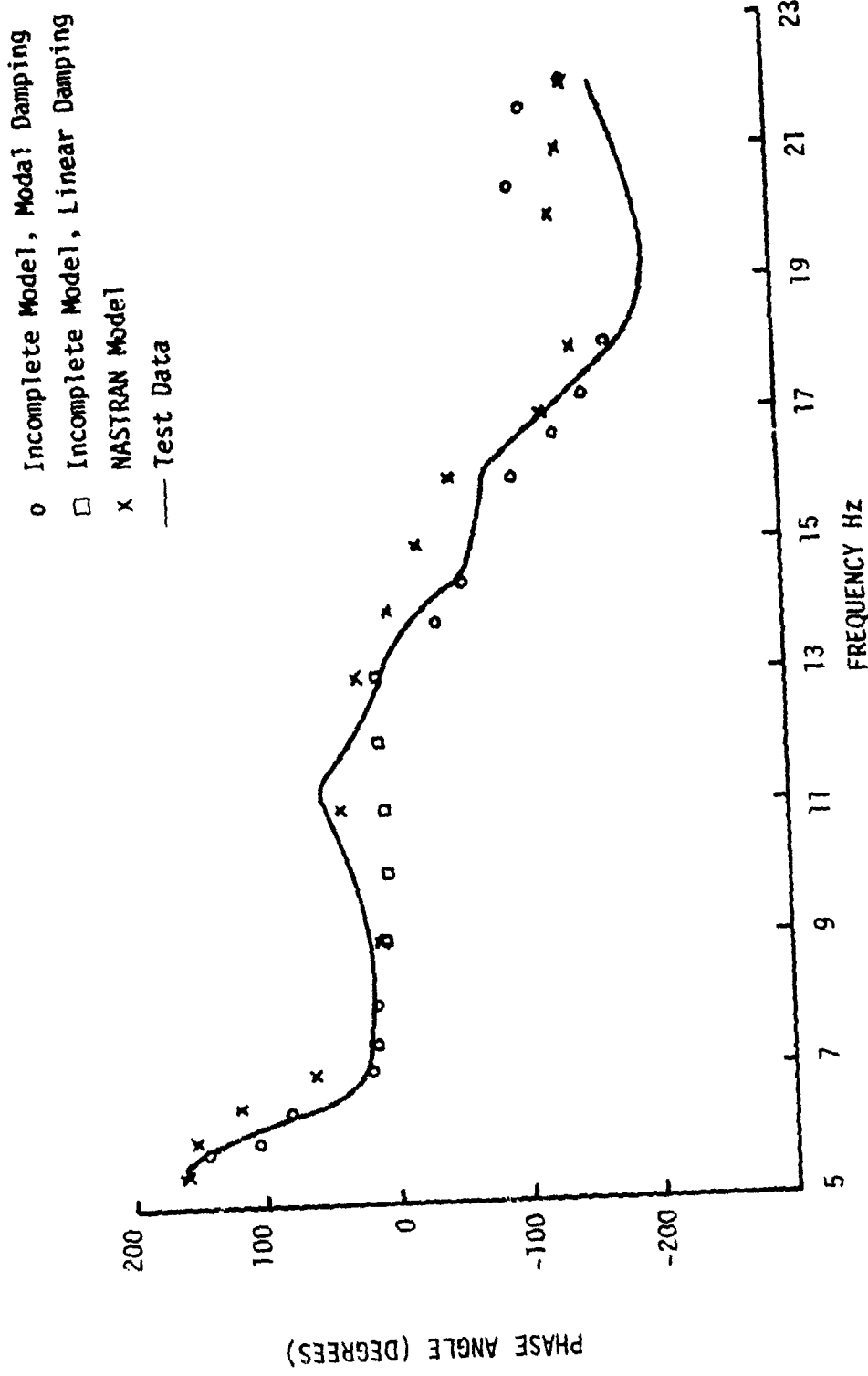
b. Phase angle.

Figure 15. Continued.

102

model predictions incorporating the improved mass and stiffness matrices developed via the Incomplete Model theory and test measurements. Since the mobility acceleration is a complex quantity, data is presented in terms of magnitude (g's/lb) and phase angle (degrees). The values of structural damping which were used in the analysis are shown in Table 23. Figures 12a and 12b present analytical and test results for the magnitude and phase angle, respectively, for the acceleration mobility $\ddot{Y}_{Z50,Z485}$, which represents the acceleration in the vertical direction at fuselage station 50 in. for force excitation applied in the vertical direction at fuselage station 485 in. Figures 13a and 13b show data in the same format for the acceleration mobility $\ddot{Y}_{Z202R,Z485}$, which represents vertical acceleration mobility for a coordinate on the right wing of the airframe for excitation applied at the tail skid location. Similarly, Figures 14 and 15 present acceleration mobility data for the response stations indicated for force excitation applied laterally at the tail rotor gearbox location. A review of the aforementioned figures indicates good agreement between the theoretical predictions and the test measurements, particularly at frequencies of excitation proximate to the natural frequencies of the airframe. The predicted vibration response obtained from the 92 degree of freedom NASTRAN model is also presented on the aforementioned figures. The data indicates that application of the Incomplete Model methodology has significantly improved the analytical model vibration response prediction capability. The natural frequencies predicted using the reduced NASTRAN model did not agree with test data; however, the incomplete model results showed a high degree of correlation with test data in the vicinity of the natural frequencies. Additionally, the incomplete model improved the vibration response predictions for the off resonance frequency bands. One factor which must be considered is that the test data presented in the aforementioned figures reflects the complex modes which characterize the AH-1G airframe, while the analytical predictions are based on a mathematical model developed from orthonormal modal data consisting of scalar elements. Introduction of complex orthonormal modes into the analysis would, undoubtedly, improve the correlation.

TABLE 23.   STRUCTURAL DAMPING USED FOR
ACCELERATION MOBILITY PREDICTION.

Natural Frequency Hz	Modal Damping	Frequency Range Hz
6.28	.16	5.8 - 6.4
7.32	.066	7.0 - 9.0
14.35	.18	13.8 - 14.6
15.99	.103	15.6 - 17.0
17.60	.083	17.2 - 18.4
22.06	.148	20.0 - 22.4

TRUNCATED MODEL MASS AND STIFFNESS CHANGES

Using the Truncated Model methodology, the effects of mass changes on the AH-1G airframe were predicted. The baseline model used in the analysis was based on six modes which were extracted from test data and considered to be significant and linearly independent. The analytical predictions of natural frequencies and orthonormal mode shape elements resulting from the mass changes were compared to test results for the respective mass configurations.

The AH-1G airframe is characterized by high modal response associated with the tail boom, particularly in the area of the vertical fin, and to a lesser degree in the nose section of the fuselage. Generally, the center section of the airframe displays low modal activity.

MASS CHANGES

The mass changes presented in Table 17 were used in the truncated model for predicting the low gross weight natural frequencies and orthonormal mode shapes from the high gross weight baseline configuration. Table 24 presents a comparison of predicted natural frequencies and the results obtained from shake tests of the low gross weight configuration.

TABLE 24. NATURAL FREQUENCIES FOR TRUNCATED MODEL
MASS CHANGE - HIGH TO LOW GROSS WEIGHT

Natural Frequencies	
Test	Analysis
6.29	6.38
7.19	7.37
14.78	14.52
17.71	16.12
19.14	18.30

A comparison of the orthonormal modes associated with the first three natural frequencies shown in the preceding table showed excellent agreement between the modal elements obtained from test data and those developed analytically. However, a comparison of the modal data developed from shake tests of the high gross weight configuration and the low gross weight condition displayed minor changes in the respective modal elements. Table 25 presents results for the first mode which is the fuselage first lateral bending mode. Similar results were obtained for the natural frequencies at 7.19 Hz and 14.78 Hz. Table 26 shows a comparison of test and analytical results for the mode associated with 17.71 Hz. Results for the 19.14 Hz mode are shown in Table 27, indicating the predictive capability of the truncated model. Qualitatively, the results are in agreement and the truncated model satisfactorily predicts the direction of change in the modal elements in developing the low gross weight data from the high gross weight configuration.

TABLE 25. TRUNCATED MODEL MASS CHANGE - HIGH
GROSS WEIGHT TO LOW GROSS WEIGHT
(Orthonormal Mode 6.29 Hz)

Natural Frequency	High Gross Weight	Low Gross Weight	
	Test	Test	Analysis
	6.28	6.29	6.38
D.O.F.			
Y464L 14	.354	.292	.379
Y480 17	.669	.600	.697
Y490 19	.501	.539	.524
Y517 21	1.423	1.669	1.441
Y521 23	1.883	1.891	1.902
YHUB 30	.7530	.650	.767
Y95R 80	.220	.149	.228
Y50 90	.354	.371	.368

TABLE 26. TRUNCATED MODEL MASS CHANGE - HIGH GROSS WEIGHT TO LOW GROSS WEIGHT
(Orthonormal Mode 17.71 Hz)

Natural Frequency	High Gross Weight	Low Gross Weight	
	Test 15.99	Test 17.71	Analysis 16.12
D.O.F.			
Z396R 2	.576	.573	.511
Y380 4	.342	.307	.571
Z340 7	.728	-.198	.392
Y480 17	.430	.610	.772
X540 22	.904	.68̲	.807
Z540 24	-.663	-.358	-.561
Y60L 86	-.651	.168	.070
Z50 92	.334	-.070	.139

TABLE 27. TRUNCATED MODEL MASS CHANGE - HIGH GROSS WEIGHT TO LOW GROSS WEIGHT
(Orthonormal Mode Comparison)

Natural Frequency	High Gross Weight	Low Gross Weight	
	Test 17.60	Test 19.14	Analysis 18.30
D.O.F.			
Z396R 2	.190	.619	.533
Z400 9	.204	.580	.539
Z464 15	.145	.739	.480
Z460 18	.125	.866	.531
X540 22	.158	.986	.706
Z540 24	-.141	-.362	-.288
Z93R 81	.186	-.0280	.201
Z46R 89	.297	-.124	.337

Similarly, the mass changes indicated in Table 17 were applied to the high gross weight mass configuration to develop the natural frequencies and orthonormal mode shapes associated with the mean gross weight condition. Table 28 shows the predicted natural frequencies and test results for the mean gross weight vehicle. The analytical data were achieved by using the high gross weight truncated model and incorporating analytically the mass changes to effect the mean gross weight condition.

TABLE 28. NATURAL FREQUENCIES FOR TRUNCATED MODEL MASS CHANGE - HIGH TO MEAN GROSS WEIGHT

Natural Frequencies	
Test	Analysis
6.17	6.30
7.15	7.34
14.39	14.28
17.88	16.03
24.12	22.45

For the first two modes given in Table 28 the mean gross weight modal data generated analytically from the high gross weight baseline truncated model were in agreement with the similar data developed from dynamic tests of the mean gross weight configuration. However, the orthonormal modes developed from the high gross weight test data did not vary significantly from the respective modes obtained from the mean gross weight test results. Table 29 presents a comparison of the modal elements for the 14.39 Hz mode. The analysis results display the correct trend although, generally, the changes from the high gross weight baseline configuration are small. Table 30 shows elemental mode data for the 24.12 Hz mode.

Comparison of the mode shapes developed analytically for the low and mean gross weight configurations by introducing concentrated mass changes to the high gross weight configuration truncated model generally showed good agreement with natural frequencies and the respective modes generated from test data.

108

TABLE 29. TRUNCATED MODEL MASS CHANGE - HIGH
GROSS WEIGHT TO MEAN GROSS WEIGHT
(Orthonormal Mode 14.39 Hz)

Natural Frequency	High Gross Weight Test 14.35	Mean Gross Weight	
		Test 14.39	Analysis 14.28
D.O.F.			
Z396L 3	.159	-.211	.151
Y422L 10	-.817	-.543	-.780
Y440 13	-1.148	-1.064	-1.093
Y480 17	-1.021	-.624	-.960
Y521 23	.376	.669	.380
Y95R 80	-.349	.198	-.345
Y60L 86	-.545	-.351	-.547
Y50 90	-.676	-.423	-.665

TABLE 30. TRUNCATED MODEL MASS CHANGE - HIGH
GROSS WEIGHT TO MEAN GROSS WEIGHT
(Orthonormal Mode 24.12 Hz)

Natural Frequency	High Gross Weight Test 22.06	Mean Gross Weight	
		Test 24.12	Analysis 22.45
D.O.F.			
Z396R 2	.482	.309	.438
Z400 9	.543	.328	.509
Z423 11	.649	.432	.617
Z464 15	.709	.378	.679
Y490 19	.226	.189	.210
Y517 21	.090	.195	.131
Z61R 88	-.170	-.093	-.197
Z50 92	-.247	-.188	-.286

STIFFNESS CHANGES

The Truncated Model theory was used to predict the effect of the three stiffness changes which were implemented during the ground vibration tests of the AH-1G airframe. Three strut type stiffness changes were applied. The Truncated Model developed from the high gross weight, forward center-of-gravity configuration was used as the baseline and the stiffness changes were analytically incorporated in that model.

During the ground vibration tests of the stiffness modifications force excitation was applied in the vertical direction only. The results of the shake tests indicated that removal of the lift link did not signifi-cantly alter the natural frequencies or response of the airframe vertical bending modes. Removal of the lift link effectively separates the upper body, consisting of the transmission and rotor pylon, from the basic airframe; consequently, the airframe modal characteristics are not affected. A rotor pylon mode in the longitudinal direction was observed in the test results but did not appear in the analytical results. This is probably due to inadequate representation of the pylon structure in the original analytical model.

The first stiffness change involved analytically deleting the lift link calculated stiffness (2.717×10^7 lb/in.) between coordinates Z195T and Z195B. Table 31 lists the natural frequencies developed theoretically and those obtained from test data.

TABLE 31. NATURAL FREQUENCIES FOR TRUNCATED MODEL

STIFFNESS CHANGE - LIFT LINK REMOVED

Natural Frequencies	
Test	Analysis
7.16	7.32
14.65	14.35
20.84	22.06

Table 32 presents data for the first vertical bending mode at 7.16 Hz. Similarly, the data given in Table 33 is for the 14.65 Hz mode. Test results for the lift link removed configuration revealed a mode at 20.84 Hz with primary response in the vertical direction. Analysis indicated a mode at 22.06 Hz, also in the vertical direction. However, there was little correlation between the respective modal elements.

The second stiffness change that was implemented in the airframe involved substitution of a DAVI lift link, with stiffness of 7500 lb/in. in the vertical direction, for the conventional lift link. Regarding the analytical model, this change was reflected by deleting stiffness of 2.709×10^7 lb/in. between coordinates Z195T and Z195B, which are the approximate lift link attachment points.

TABLE 32. TRUNCATED MODEL STIFFNESS CHANGE – LIFT LINK REMOVED
(Orthonormal Mode 7.16 Hz)

| | Lift Link In | Lift Link Out | |
| | Test | Test | Analysis |
Natural Frequency	7.32	7.16	7.32
D.O.F.			
Z404R 1	.139	.145	.130
Z464 15	.407	.477	.399
Z460 18	.439	.512	.430
Z485 20	.610	.722	.602
Z540 24	.974	1.177	.967
ZMHUB 29	.314	.316	.305
X60L 87	.174	.228	.177
Z50 92	.232	.294	.235

TABLE 33. TRUNCATED MODEL STIFFNESS CHANGE -
LIFT LINK REMOVED
(Orthonormal Mode 14.65 Hz)

Natural Frequency	Lift Link In	Lift Link Out	
	Test	Test	Analysis
	14.35	14.65	14.35
D.O.F.			
Y380 4	.478	.343	.471
Y339L 6	.246	.249	.247
Y422L 10	.817	.487	.810
Y464L 14	1.073	.667	1.061
Y490 19	.917	.495	.909
Y520 23	-.376	-.358	-.375
Y60L 86	.545	.120	.549
Y50 90	.676	.154	.675

This value is the difference in spring rate between the original lift link
(2.717 x 10^7 lb/in.) and the spring rate of the DAVI lift link (7500 lb/in.)
Table 34 presents the predicted natural frequencies and test values for the
DAVI lift link configuration.

TABLE 34. NATURAL FREQUENCIES FOR TRUNCATED MODEL STIFFNESS
CHANGE - DAVI LIFT LINK CONFIGURATION

Natural Frequencies	
Test	Analysis
7.17	7.28
14.89	14.35
15.62	15.95
20.90	22.04

113

During the test, the DAVI lift link condition exhibited a rotor pylon mode in the fore-and-aft direction at a frequency of 5.80 Hz, which was not evident in the truncated model analysis. Typical orthonormal mode elements for both theory and test results are presented in Tables 35 and 36. For the DAVI lift link installed configuration the modal elements derived analytically are in agreement with the respective test results. However, there is practically no difference in modal data for the two configurations tested.

TABLE 35. TRUNCATED MODEL STIFFNESS CHANGE -
DAVI LIFT LINK INSTALLED
(Orthonormal Mode 7.17 Hz)

	Lift Link In	DAVI Lift Link Installed	
Natural Frequency	Test	Test	Analysis
	7.32	7.17	7.28
D.O.F.			
Z396R 2	.104	.105	.109
Z423 11	.193	.212	.189
Z464 15	.407	.471	.399
Z460 18	.439	.502	.430
X540 22	-.541	-.620	-.540
Z540 24	.974	1.123	.967
Z46R 89	.201	.252	.200
Z50 92	.232	.288	.235

114

TABLE 36.   TRUNCATED MODEL STIFFNESS CHANGE -
DAVI LIFT LINK INSTALLED
(Orthonormal Mode 15.62 Hz)

Natural Frequency	Lift Link in	DAVI Lift Link Installed	
	Test	Test	Analysis
	15.99	15.62	15.95
D.O.F.			
Z404R 1	.676	.782	.662
Z381 5	.436	.540	.424
Z423 11	.431	.592	.418
Z464 15	.302	.465	.295
Z460 18	.361	.522	.357
Z540 24	-.663	-.549	-.644
Z61R 88	.236	.285	.213
Z50 92	.334	.443	.300

The third stiffness condition that was shake tested introduced a stiffening element between the tail boom and the vertical tail. The spring rate of the element was calculated as 5.53×10^4 lb/in. in a direction coincident with the longitudinal axis of the stiffener. The natural frequencies obtained via test and those analytically generated are detailed in Table 37.

TABLE 37.   NATURAL FREQUENCIES FOR TRUNCATED MODEL STIFFNESS
CHANGE - TAIL STIFFENER CONFIGURATION

Natural Frequencies	
Test	Analysis
7.13	10.83
14.66	14.47
20.94	23.20

The orthonormal mode data associated with the test natural frequencies of 7.13 Hz and 20.94 Hz are presented in Tables 38 and 39. For the tail stiffener configuration theoretical and test results did not compare as favorably as for the other mass and stiffness conditions investigated. A possible explanation is that the attachment points of the stiffener element are soft; consequently the effective stiffness of the element is modified by the local flexibility of the attachment points. Thus, the effective spring rate introduced by the stiffener is insignificant and differs from the value used in the analysis, causing a lack of correlation between test data and theoretical results.

TABLE 38. TRUNCATED MODEL STIFFNESS CHANGE -
TAIL STIFFENER INSTALLED
(Orthonormal Mode 7.13 Hz)

Natural Frequency		No Tail Stiffener	Tail Stiffener Installed	
		Test	Test	Analysis
		7.32	7.13	10.83
D.O.F.				
Z404R	1	.139	.131	.510
Z423	11	.193	.193	.416
Z464	15	.407	.425	.531
Z460	18	.439	.462	.588
Z485	20	.610	.644	.603
Z540	24	.974	.709	.493
Z50L	87	.174	.205	.237
Z50	92	.232	.266	.399

116

TABLE 39. TRUNCATED MODEL STIFFNESS CHANGE -
TAIL STIFFENER INSTALLED
(Orthonormal Mode 20.94 Hz)

Natural Frequency		No Tail Stiffener	Tail Stiffener Installed	
		Test	Test	Analysis
		22.06	20.94	23.20
D.O.F.				
Z404R	1	.597	.556	.232
Z381	5	.436	.294	.195
Z340	7	-.515	-1.048	-.871
Z464	15	.709	.363	.567
Z485	20	.459	.174	.497
X540	22	.792	.695	.196
Z61R	88	-.175	-.168	-.266
Z50	92	-.247	-.235	-.371

INCOMPLETE MODEL MASS AND STIFFNESS CHANGES

MASS CHANGES

Using the Incomplete Model development, the effect of mass changes on the AH-1G airframe were predicted. The procedure described previously for the Truncated Model approach was also used in the Incomplete Model application for predicting the effects of the mass and stiffness modifications to the airframe which were shake tested. Table 40 shows the theoretically derived natural frequencies and those extracted from test data for the low gross weight condition.

Table 41 presents orthonormal modal data at a frequency of 6.29 Hz, which is the first lateral bending mode of the airframe. Modal data for the 17.71 Hz natural frequency are delineated in Table 42. The tabular data present evidence that the incomplete model, generally, is capable of predicting the effect of mass change for the low gross weight configuration. In particular, the changes in the modal elements are usually in the correct direction.

Table 43 shows predicted natural frequencies developed from the Incomplete Model theory and the values obtained from shake tests of the mean gross weight configuration. The theoretical results were obtained by applying the appropriate mass changes to the NASTRAN model, which was originally improved on the basis of the high gross weight orthonormal modes developed from test data.

118

TABLE 40. NATURAL FREQUENCIES FOR INCOMPLETE MODEL
MASS CHANGE - HIGH TO LOW GROSS WEIGHT

Natural Frequencies	
Test	Analysis
6.29	6.29
7.19	7.32
14.78	14.34
17.71	15.97
19.14	20.52

TABLE 41. INCOMPLETE MODEL MASS CHANGE - HIGH
GROSS WEIGHT TO LOW GROSS WEIGHT
(Orthonormal Mode 6.29 Hz)

Natural Frequency		High Gross Weight	Low Gross Weight	
		Test	Test	Analysis
		6.28	6.29	6.28
D.O.F.				
Y464L	14	.354	.292	.357
Y480	17	.669	.600	.673
Y495	19	.501	.539	.505
Y517	21	1.423	1.669	1.427
Y521	23	1.883	1.891	1.887
YHUB	30	.753	.650	.751
Y95R	80	.220	.149	.220
Y50	90	.354	.371	.354

TABLE 42. INCOMPLETE MODEL MASS CHANGE - HIGH GROSS WEIGHT TO LOW GROSS WEIGHT
(Orthonormal Mode 17.71 Hz)

Natural Frequency		High Gross Weight	Low Gross Weight	
		Test	Test	Analysis
		15.99	17.71	15.97
D.O.F.				
Z396R	2	.576	.573	.412
Y380	4	.342	.307	.573
Z340	7	.728	-.198	.341
Y480	17	.430	.610	.773
X540	22	.904	.682	.725
Z540	24	-.663	-.358	-.527
Y60L	80	-.651	.168	-.473
Z50	92	.334	-.07	.127

TABLE 43. NATURAL FREQUENCIES FOR INCOMPLETE MODEL MASS CHANGE
MASS CHANGE - HIGH TO MEAN GROSS WEIGHT

Natural Frequencies	
Test	Analysis
6.17	6.32
7.15	7.34
14.39	14.29
17.88	16.00
24.12	19.94

Data shown in Tables 44 and 45 are for the 14.39 Hz and 24.12 Hz modes which are natural frequencies obtained from dynamic tests of the mean gross weight configuration. From a review of the mean gross weight data presented it is apparent that the mass changes that were effected did not significantly alter the airframe natural frequencies or associated mode shapes.

TABLE 44. INCOMPLETE MODEL MASS CHANGE - HIGH
GROSS WEIGHT TO MEAN GROSS WEIGHT
(Orthonormal Mode 14.39 Hz)

Natural Frequency		High Gross Weight	Mean Gross Weight	
		Test	Test	Analysis
		14.35	14.39	14.29
D.O.F.				
Z396L	3	.159	- .211	.135
Y422L	10	- .817	- .542	- .774
Y440	13	-1.148	-1.064	-1.089
Y480	17	-1.021	- .624	- .964
Y521	23	.376	.669	.356
Y95R	80	- .349	.198	- .343
Y60L	86	- .545	- .351	- .541
Y50	90	- .676	- .428	- .660

TABLE 45. INCOMPLETE MODEL MASS CHANGE - HIGH
GROSS WEIGHT TO MEAN GROSS WEIGHT
(Orthonormal Mode 24.12 Hz)

Natural Frequency		High Gross Weight	Mean Gross Weight	
		Test	Test	Analysis
		22.06	24.12	19.94
D.O.F.				
Z396R	2	.482	.309	.266
Z400	9	.543	.328	.338
Z423	11	.649	.432	.386
Z464	15	.709	.378	.365
Y490	19	.226	.189	-.076
Y517	21	.090	.195	-.036
Z61R	88	-.170	.093	-.281
Z50	92	-.247	-.188	-.283

16
B

STIFFNESS CHANGES

Incomplete Model system identification was also used to predict the effect
on natural frequencies and mode shapes of the stiffness changes that were
incorporated in the AH-1G airframe during the ground vibration phase of
the program. Table 46 presents the natural frequencies for the lift link
removed stiffness configuration.

122

TABLE 46. NATURAL FREQUENCIES FOR INCOMPLETE
MODEL STIFFNESS CHANGE -
LIFT LINK REMOVED

Natural Frequencies	
Test	Analysis
7.16	7.27
14.65	14.34
20.84	21.04

Tables 47 and 48 present orthonormal modal data obtained analytically and similar data extracted from test results for the 14.65 Hz mode and the 20.84 Hz test mode.

TABLE 47. INCOMPLETE MODEL STIFFNESS CHANGE -
LIFI LINK REMOVED
(Orthonormal Mode 14.65 Hz)

		Lift Link In	Lift Link Removed	
Natural Frequency		Test	Test	Analysis
		14.35	14.65	14.35
D.O.F.				
Y380	4	.478	.343	.483
Y339L	6	.246	.249	.244
Y422L	10	.817	.487	.822
Y464L	14	1.073	.667	1.082
Y490	19	.917	.495	.924
Y521	23	- .376	- .358	- .377
Y60L	86	.545	.120	.542
Y50	92	.676	.154	- .090

123

TABLE 48. INCOMPLETE MODEL STIFFNESS CHANGE -
LIFT LINK REMOVED
(Orthonormal Mode 20.84 Hz)

Natural Frequency		Lift Link In	Lift Link Removed	
		Test	Test	Analysis
		22.06	20.84	21.02
D.O.F.				
Z404R	1	.597	-.223	-.331
Z423	11	.649	-.225	-.109
Z464	15	.709	-.258	-.005
X540	22	.792	.109	-.204
Z268L	42	-.208	-.083	.172
Z200L	62	-.052	-.006	.172
Y95R	80	.014	-.015	.215
Z50	92	-.247	-.103	.159

Natural frequency data for the condition wherein the DAVI lift link was
substituted for the conventional lift link are given in Table 49.

TABLE 49. NATURAL FREQUENCIES FOR INCOMPLETE
MODEL STIFFNESS CHANGE -
DAVI LIFT LINK INSTALLED

Natural Frequencies	
Test	Analysis
7.17	7.27
14.89	14.34
15.62	16.03
20.90	21.04

124

Mode shape data associated with the natural frequencies of 7.17 and 15.62 are presented in Tables 50 and 51 respectively. In both the lift link removed and the DAVI lift link installed configurations the test results do not differ significantly from the test data for the conventional lift link condition. Although the analytical predictions of the stiffness changes agree reasonably well with the respective test results, there is no basis for judging the effectiveness of the Incomplete Model methodology in this situation.

TABLE 50. INCOMPLETE MODEL STIFFNESS CHANGE -
DAVI LIFT LINK INSTALLED
(Orthonormal Mode 7.17 Hz)

Natural Frequency	Lift Link In	DAVI Lift Link In	
	Test	Test	Analysis
	7.32	7.17	7.27
D.O.F.			
Z396R 2	.104	.105	.075
Z423 11	.193	.212	.158
Z464 15	.407	.471	.323
Z460 18	.439	.502	.334
X540 22	-.541	-.620	-.409
Z540 24	.974	1.123	.785
Z46R 89	.201	.252	.148
X50 92	.232	.288	.181

TABLE 51.   INCOMPLETE MODEL STIFFNESS CHANGE -
DAVI LIFT LINK INSTALLED

(Orthonormal Mode 15.62 Hz)

Natural Frequency		Lift Link In	DAVI Lift Link In	
		Test	Test	Analysis
		15.99	15.62	16.02
D.O.F.				
Z404R	1	.676	.782	.677
Z381	5	.436	.540	.437
Z423	11	.431	.592	.431
Z464	15	.302	.465	.295
Z460	18	.361	.522	.351
Z540	24	-.663	-.549	-.686
Z61R	88	.236	.285	.249
Z50	92	.334	.443	.354

Natural frequency data for the tail stiffener configuration are shown in Table 52.   Orthonormal mode shape data are presented in Tables 53 and 54 for the 7.13 Hz and 20.94 Hz modes, respectively.   Analytical results

TABLE 52.   NATURAL FREQUENCIES FOR INCOMPLETE
MODEL STIFFNESS CHANGE -
TAIL STIFFENER CONFIGURATION

Natural Frequencies	
Test	Analysis
7.13	10.92
14.66	14.55
20.94	22.24

TABLE 53.   INCOMPLETE MODEL STIFFNESS CHANGE -
TAIL STIFFENER INSTALLED

(Orthornormal Mode Comparison)

Natural Frequency		No Tail Stiffener	Tail Stiffener Installed	
		Test	Test	Analysis
		7.32	7.13	10.92
D.O.F.				
Z404R	1	.139	.131	.590
Z423	11	.193	.193	.510
Z464	15	.407	.425	.617
Z460	18	.439	.462	.678
Z485	20	.610	.644	.690
Z540	24	.974	.707	.352
Z60L	87	.174	.205	.235
Z50	92	.232	.266	.373

TABLE 54.   INCOMPLETE MODEL STIFFNESS CHANGE -
TAIL STIFFENER INSTALLED

(Orthonormal Mode Comparison)

Natural Frequency		No Tail Stiffener	Tail Stiffener Installed	
		Test	Test	Analysis
		22.06	20.94	22.24
D.O.F.				
Z404R	1	.597	.556	.349
Z381	5	.436	.294	.267
Z340	7	-.515	-1.048	-.785
Z464	15	.709	.363	.477
Z485	20	.459	.174	.380
X540	22	.792	.695	.123
Z61R	88	-.175	- .168	-.237
Z50	90	-.247	- .235	-.302

showed the first vertical bending mode at 10.92 Hz, but the test results with the tail stiffener installed did not reflect the change in system natural frequency. It appears the tail stiffener was ineffective because of the softness associated with the mounting system of the stiffener.

Generally, both the incomplete model and the truncated model predicted the effect of mass and stiffness changes to the airframe. The mass and stiffness changes that were incorporated in the airframe did not alter significantly the natural frequencies and mode shapes associated with the unmodified airframe. However, the incomplete model and truncated model did predict the correct trend resulting from the changes to the airframe.

DONE AND HUGHES EQUATION

The technique of Done and Hughes, which is described in Reference 8, was applied to determine the effect of the mass and stiffness changes that were implemented during the program. The method is applicable to concentrated mass changes and for strut type stiffness modifications.

The acceleration mobility between coordinates i and j, resulting from the nth discrete impedance change, is related to the acceleration mobility prior to the change via the following relationship:

$$\ddot{Y}_{ij}^{n} = \ddot{Y}_{ij}^{n-1} - \frac{\left[\ddot{Y}_{ir_n}^{n-1} - \ddot{Y}_{is_n}^{n-1} \quad \ddot{Y}_{jr_n}^{n-1} - \ddot{Y}_{js_n}^{n-1}\right]}{\Delta r_n s_n + \ddot{Y}_{r_n r_n}^{n-1} - 2\ddot{Y}_{r_n s_n}^{n-1} + \ddot{Y}_{s_n s_n}^{n-1}} \tag{91}$$

where $\ddot{Y}^{n-1}$ is the mobility (with respect to the coordinates specified by the subscripts) prior to the nth discrete impedance change and $\ddot{Y}^{n}$ is the mobility after the nth discrete impedance change

$$\Delta r_n s_n = \begin{cases} \dfrac{(2\pi\omega)^2}{384 K_{r_n s_n}} & \text{for a stiffness change of } K_{r_n s_n} \text{ lb/in.} \\ & \text{between coordinates } r_n \text{ and } s_n \\[2em] -\dfrac{1}{m_{r_n}} & \text{for a mass change of } m_{r_n} \text{ lb at coordinate } r_n. \end{cases}$$

8. Done, G. T. S., and Hughes, A. D., The Response of a Vibrating Structure as a Function of Structural Parameters. Journal of Sound and Vibration, Vol. 38, No. 2, 1975.

when the impedance change is a lumped mass at coordinate r_n, the mobilities containing the subscripts s_n in equation (91) are all defaulted to zero

i.e., for $\Delta_{r_n s_n} = -\dfrac{1}{m_{r_n}}$

$$\ddot{Y}^{n-1}_{i s_n} = \ddot{Y}^{n-1}_{j s_n} = \ddot{Y}^{n-1}_{r_n s_n} = \ddot{Y}^{n-1}_{s_n s_n} = 0$$

This is a computational artifice to make the form of equation (91) the same for both stiffness and mass changes.

The subscripts in equation (91) are defined as follows:

i and j refer to the coordinate pair for which the changed mobility is being calculated

r_n and s_n refer to the connection coordinates of the nth impedance change (subject to the artifice mentioned above).

To compute equation (91) for the nth change, all the mobilities on the right must be known after the $(n-1)^{th}$ change. In other words, if there are N discrete changes to be effected, one must start with the following mobilities:

$$\left.\begin{array}{c} \ddot{Y}^{o}_{i r_n} \\[2em] \ddot{Y}^{o}_{i s_n} \\[2em] \ddot{Y}^{o}_{j r_n} \\[2em] \ddot{Y}^{o}_{j s_n} \\[2em] \ddot{Y}^{o}_{r_n r_n} \\[2em] \ddot{Y}^{o}_{r_n s_n} \\[2em] \ddot{Y}^{o}_{s_n s_n} \end{array}\right\} \quad \text{for } n = 1 \text{ to } N$$

130

MASS CHANGES

The configuration changes of the AH-1G from high gross weight to mean gross weight, and from high gross weight to low gross weight are represented as simultaneous discrete mass changes. Table 20 shows the coordinates and the mass changes associated with the change in configuration from high gross weight to mean gross weight. Table 17 shows the coordinates and mass changes associated with the change in configuration from high gross weight to low gross weight.

For two pairs of coordinates (Z90R, Z485 gunner seat with respect to tail vertical shaking location and Z140R, Z485 pilot seat with respect to tail vertical shaking location) between 6 Hz and 10 Hz, acceleration mobilities were calculated. The mobilities of the original structure were derived by the modal series method using the modes measured from the high gross weight configuration. New mobilities resulting from the discrete mass changes of Tables 17 and 20 were calculated using the derived original mobilities and the Done and Hughes equation. Finally, mobilities based on the mode shapes of the new configurations (Mean gross weight and Low gross weight) were also derived for the same pairs of coordinates. The results are presented graphically in Figures 16, 17, 18 and 19.

The discretization of the mass changes due to the fuel redistribution associated with the helicopter configuration changes is approximate at best; the continuum character of these changes can be a major inaccuracy in the application of the Done and Hughes equation.

STIFFNESS CHANGES

Equation 91 was used to predict the effect on acceleration mobility of the stiffness changes which were incorporated in the airframe during the test phase of the program and which have been described previously. Figures 20 and 21, respectively, present the acceleration mobilities $\bar{Y}_{Z195T,Z485}$ and
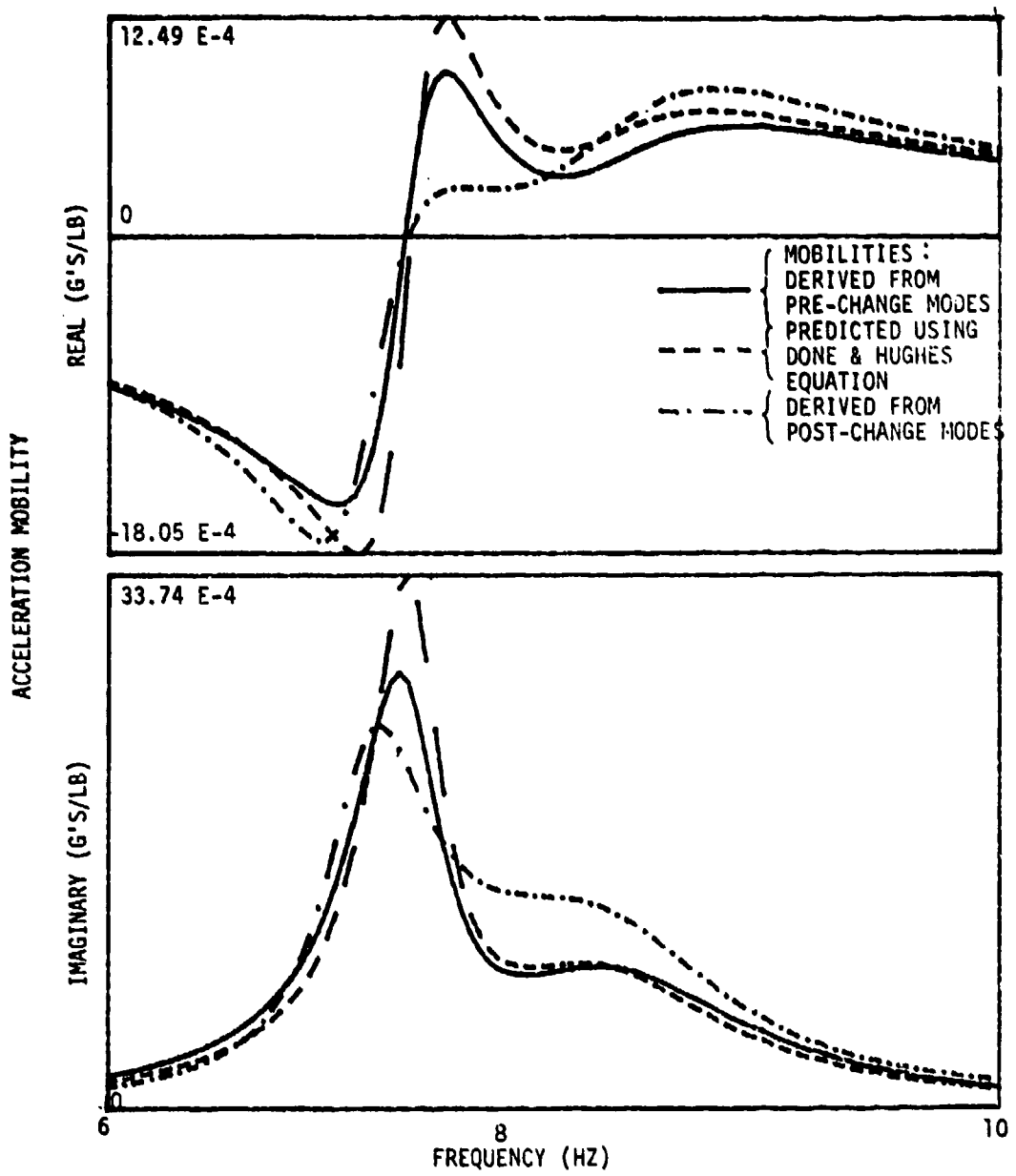
Figure 16. $\ddot{Y}_{Z90R,Z485}$ High to mean gross weight change.

132
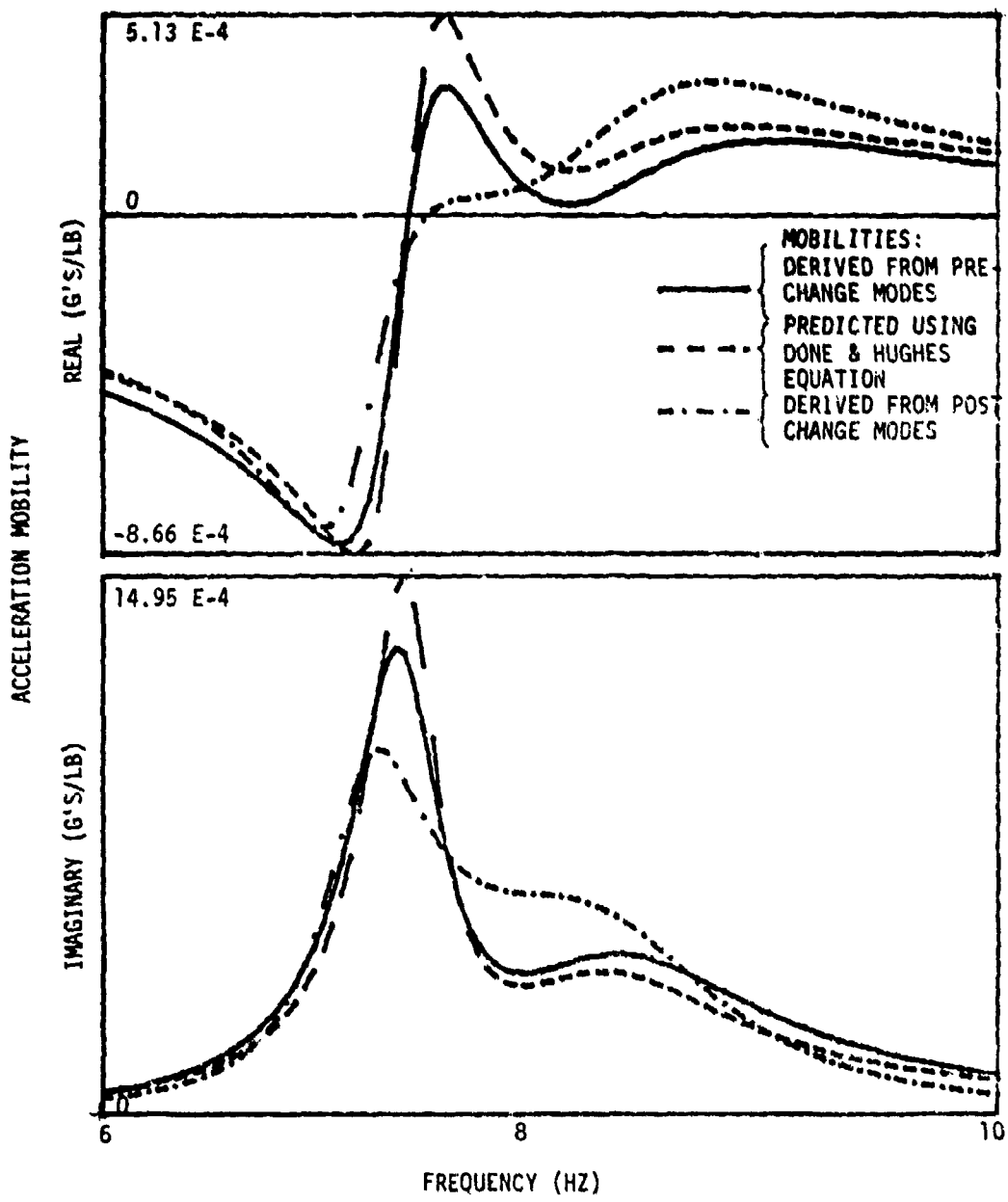
Figure 17. $\ddot{Y}_{Z140R,Z485}$ High to mean gross weight change.
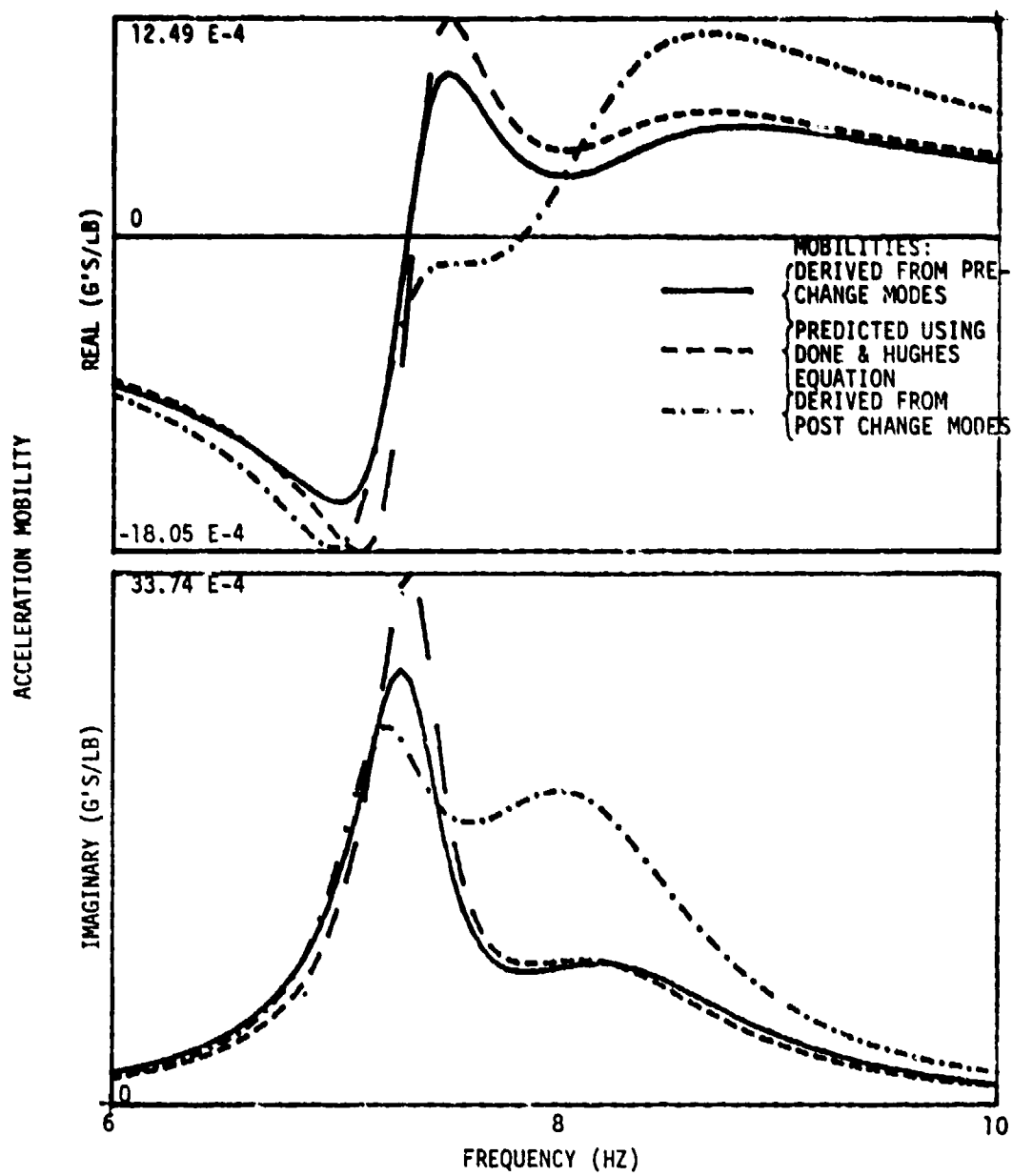
Figure 18. $\ddot{Y}_{Z90R,Z485}$ High to low gross weight change.
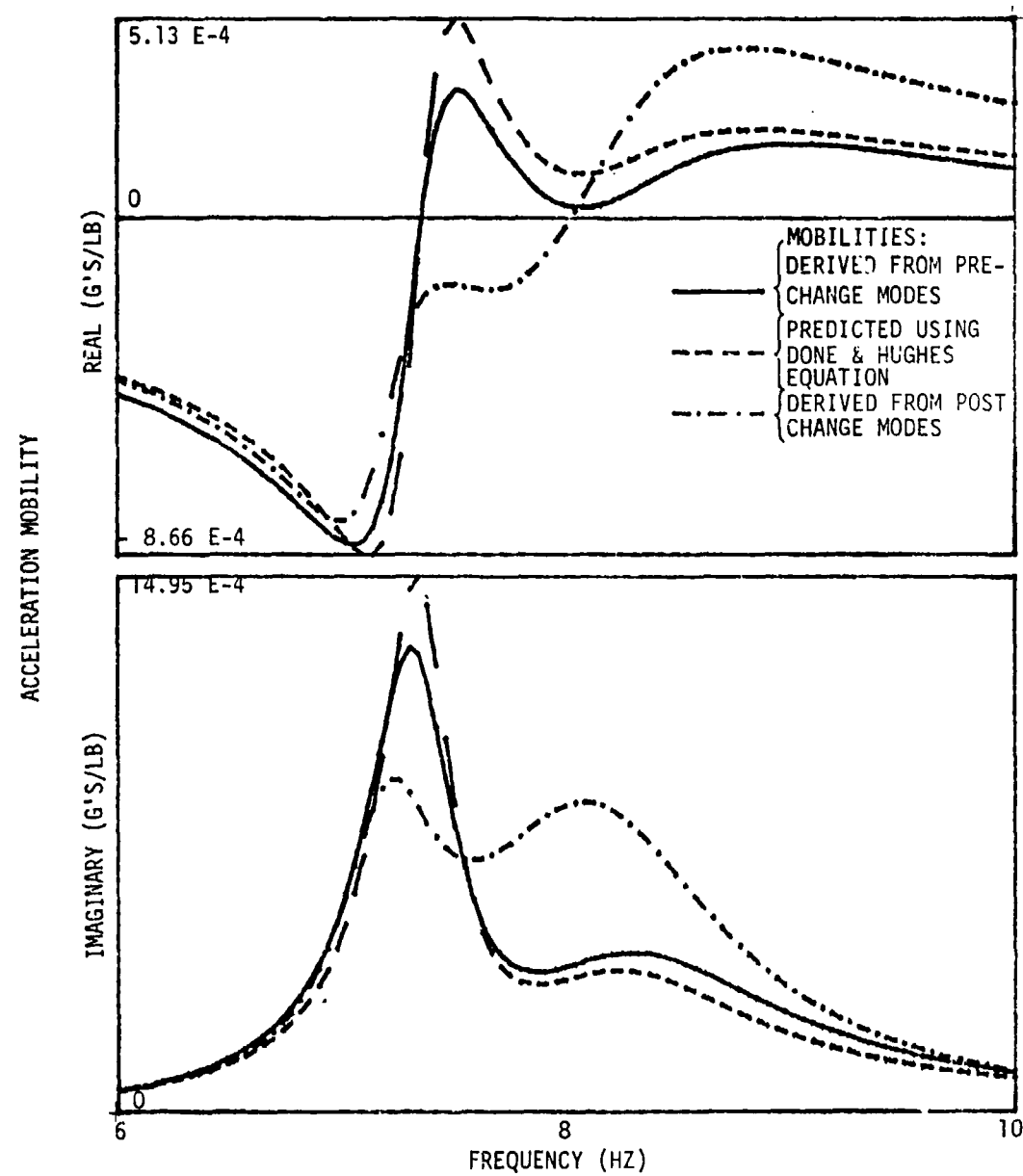
Figure 19. $\ddot{Y}_{Z140R,Z485}$ High to low gross weight change.

135
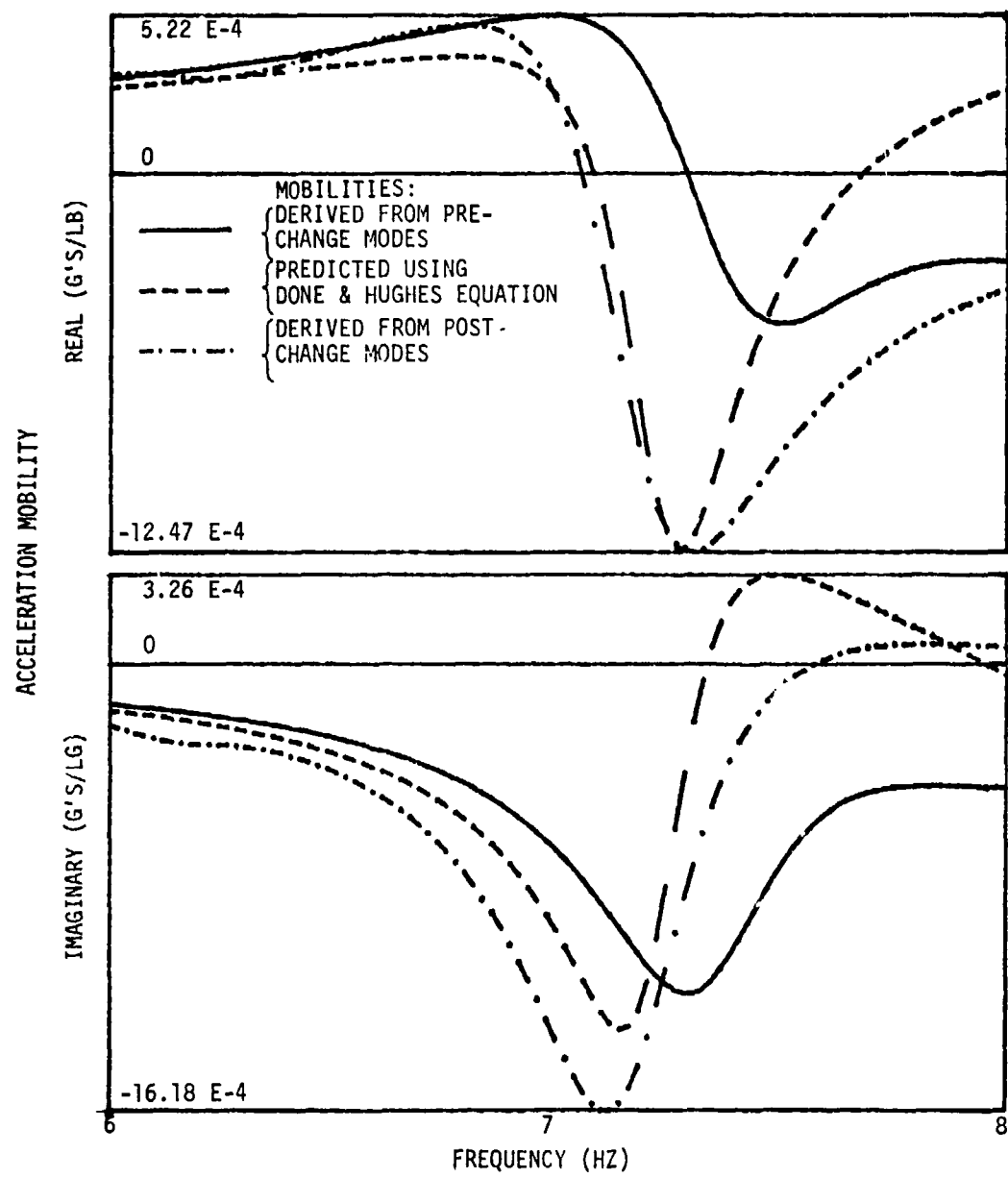
Figure 20. $\ddot{Y}_{Z195T,Z485}$ Lift link removal change.

136
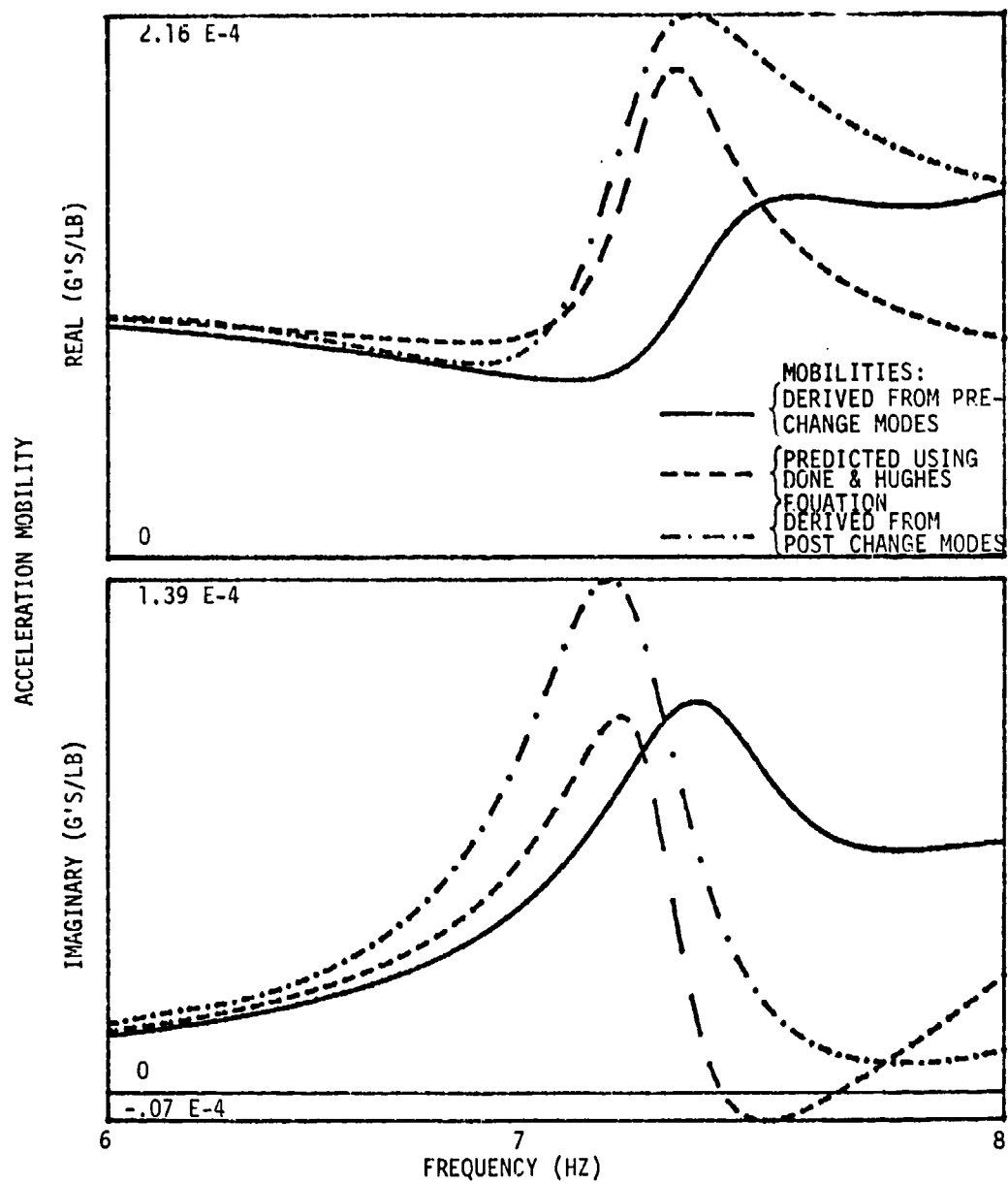
Figure 21. $\ddot{Y}_{Z195T,Z195T}$ Lift link removal change.

$\ddot{Y}_{Z195T,Z195T}$ for the lift link removed configurations. Similarly, data for the stiffness condition wherein the DAVI lift link replaced the conventional lift link are shown in Figures 22 and 23. The acceleration mobility data predicted using the Done and Hughes equation are in reasonable agreement with the synthesized data. Additionally, the shift in natural frequency resulting from the stiffness modification is predicted correctly. The predicted acceleration mobility data indicate that the natural frequency of the system occurs at a lower frequency which is consistent with the acceleration mobility data derived using the measured modes of the changed configuration.

Data for the tail stiffener installed configuration are shown in Figure 24. The results indicate that the effective impedance associated with the installation of the stiffening element is much lower than the value which was calculated for the stiffener. The acceleration mobilities predicted from the Done and Hughes expression are very small compared to those derived using the orthonormal modes of the changed stiffness configuration.

A logical explanation for these results is that the stiffening member attachment points to the airframe are soft and behave as series connected impedances to the stiffening element. This is a manifestation of the problem of local flexibility occurring in the testing of structures. The resultant stiffness of the member and the local flexibility is lower than either of the individual impedances.

18
B

138
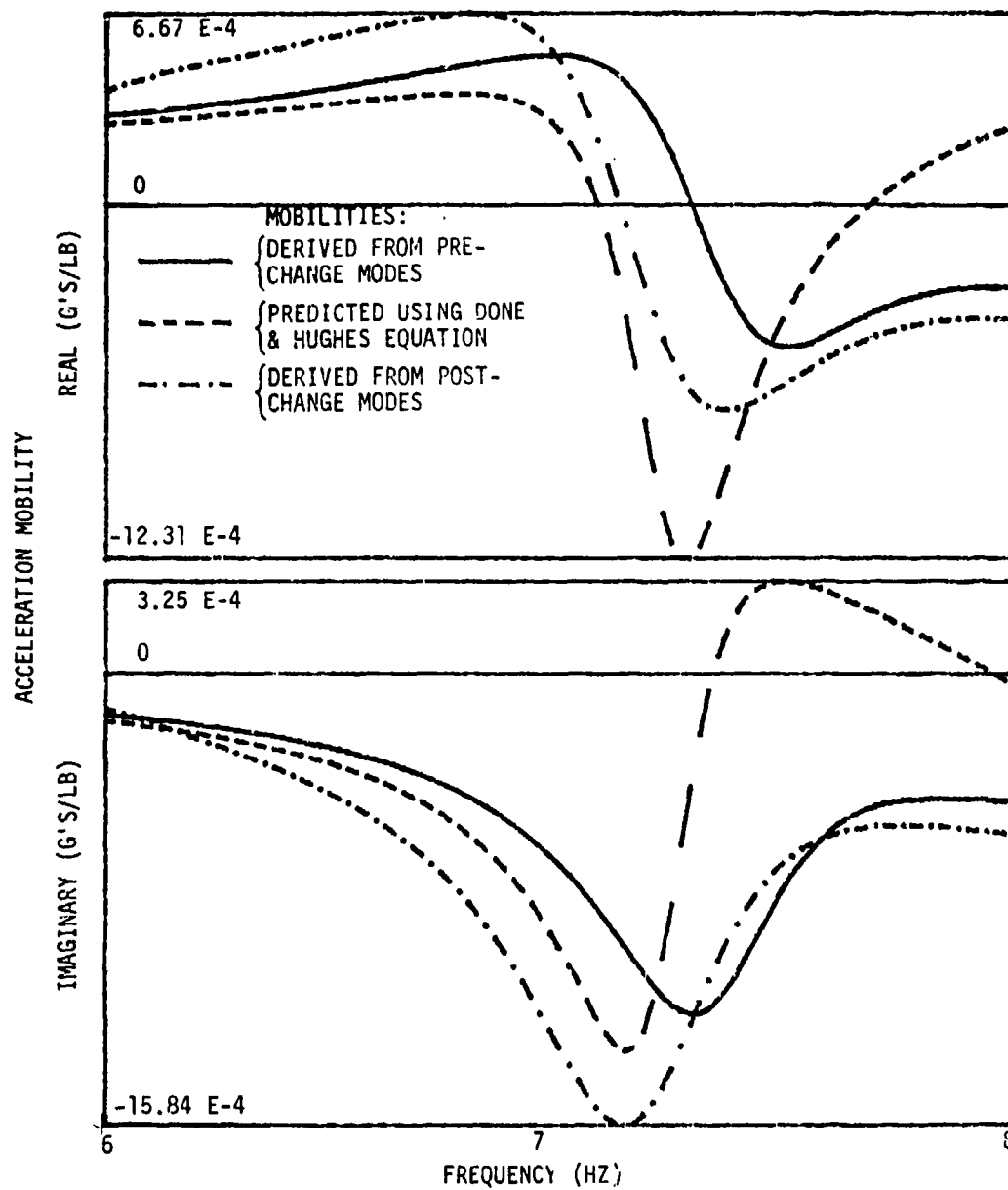
Figure 22. $\ddot{Y}_{Z195T,Z485}$ Lift link replaced by DAVI link.
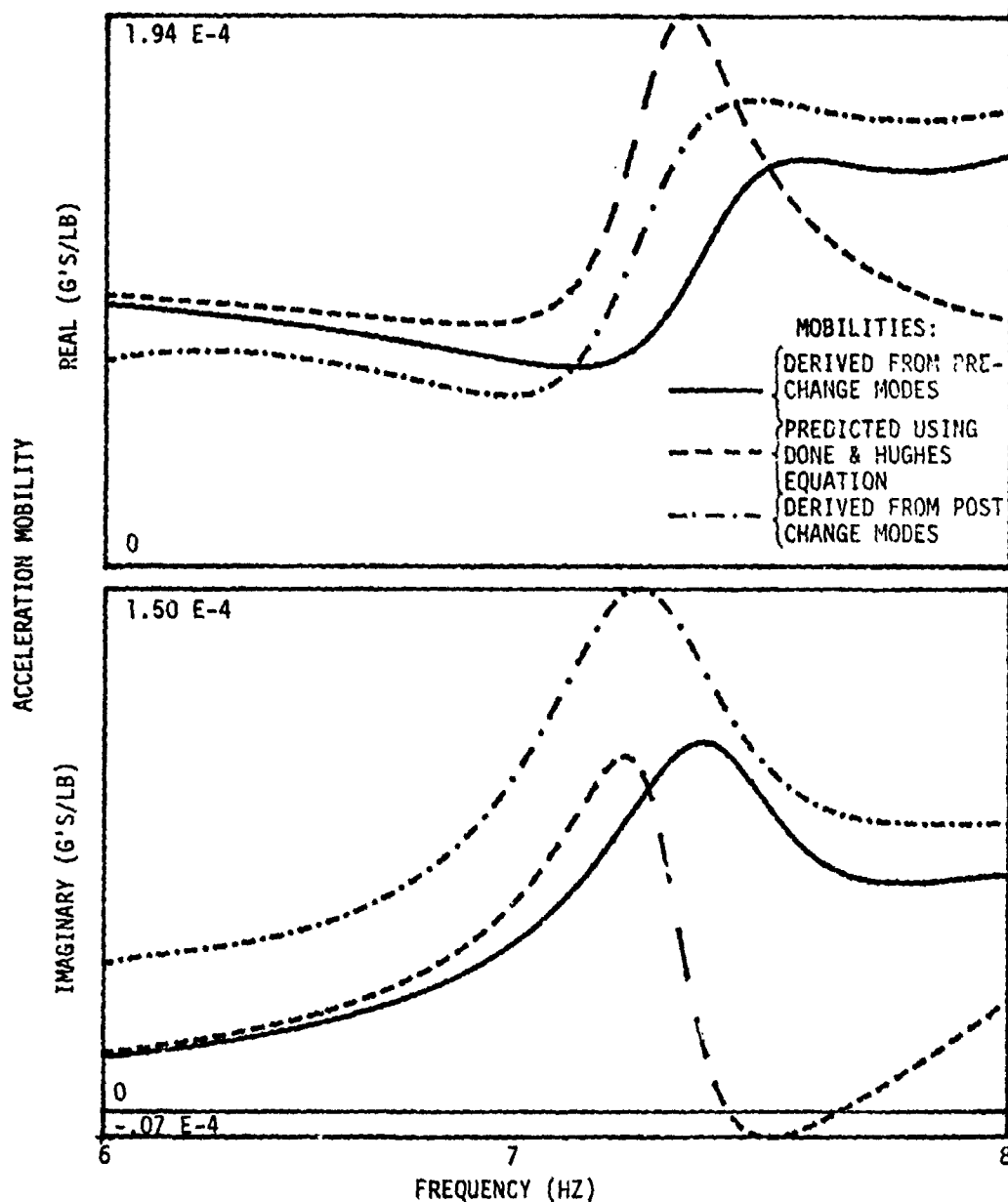
Figure 23. $\ddot{Y}_{Z195T,Z195T}$ Lift link replaced by DAVI link.

140
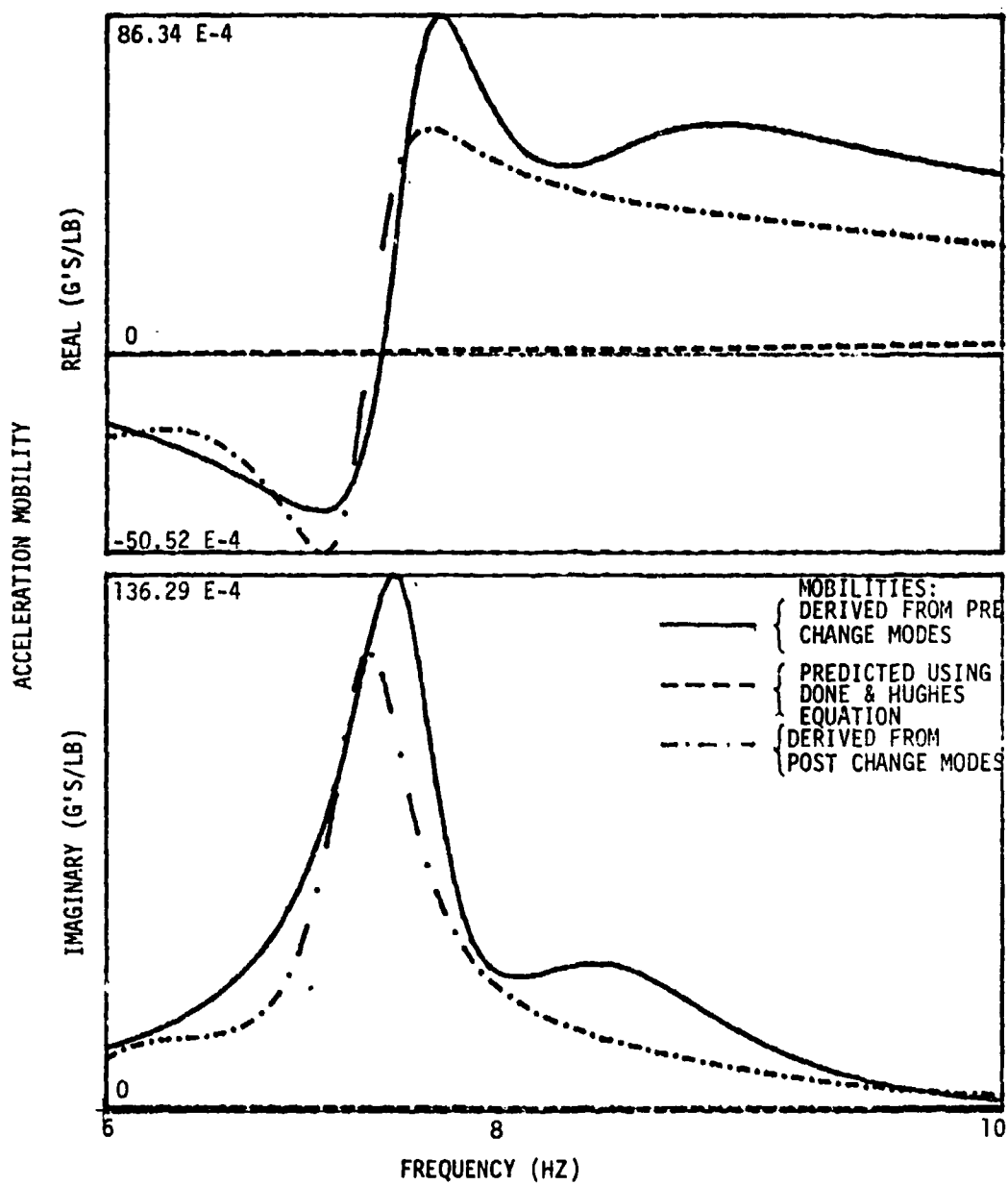
Figure 24. $\ddot{Y}_{X540,Z485}$ Installation of tail stiffener.

ERROR ANALYSIS

In order to evaluate the effect of possible error in the test measurements
on the Incomplete Model technique for model improvement, it is essential to
simulate realistic errors in the test data. In the present analysis, error
was applied to the orthornormal mode shapes to reflect possible errors in
the measurement of airframe accelerations.

The types of errors that were incorporated in the study included uniformly
distributed random percentage error between specified limits and a con-
stant specified percentage bias error. Both types of error were applied
to the orthonormal mode elements.

The simulated measurement errors representative of the current state of the
art and used in the analysis ranged to $\pm$ 10% random error and 10% bias error.
The purpose of the error analysis was to determine the sensitivity of the
Incomplete Model methodology to possible errors in test measurements. The
procedure that was followed involved applying specified levels of random
and bias error to the orthonormal modes derived from test measurements.
Using the orthonormal modes contaminated with the simulated error, the
Incomplete Model theory was applied to the 92 degree of freedom NASTRAN
model yielding modified mass and stiffness matrices. These matrices were
subseq 1tly used in developing acceleration mobilities at particular
forcing frequencies. Frequency spectrums for particular points of interest
on the airframe were developed incorporating the simulated measurement
errors and the results compared to the zero measurement error condition.

Figure 25 presents typical acceleration mobility data, $\ddot{Y}_{Z50, Z485}$, describ-
ing the vertical response at degree of freedom Z50 for force excitation
applied arti   at the tail skid location Z485. Data for $\ddot{Y}_{Y521,Y521}$
are shown in Figure 26. In each situation the frequency response data are
shown for the zero error condition and for several levels and a combination
of random and bias error applied to the orthonormal mode shape data.

142
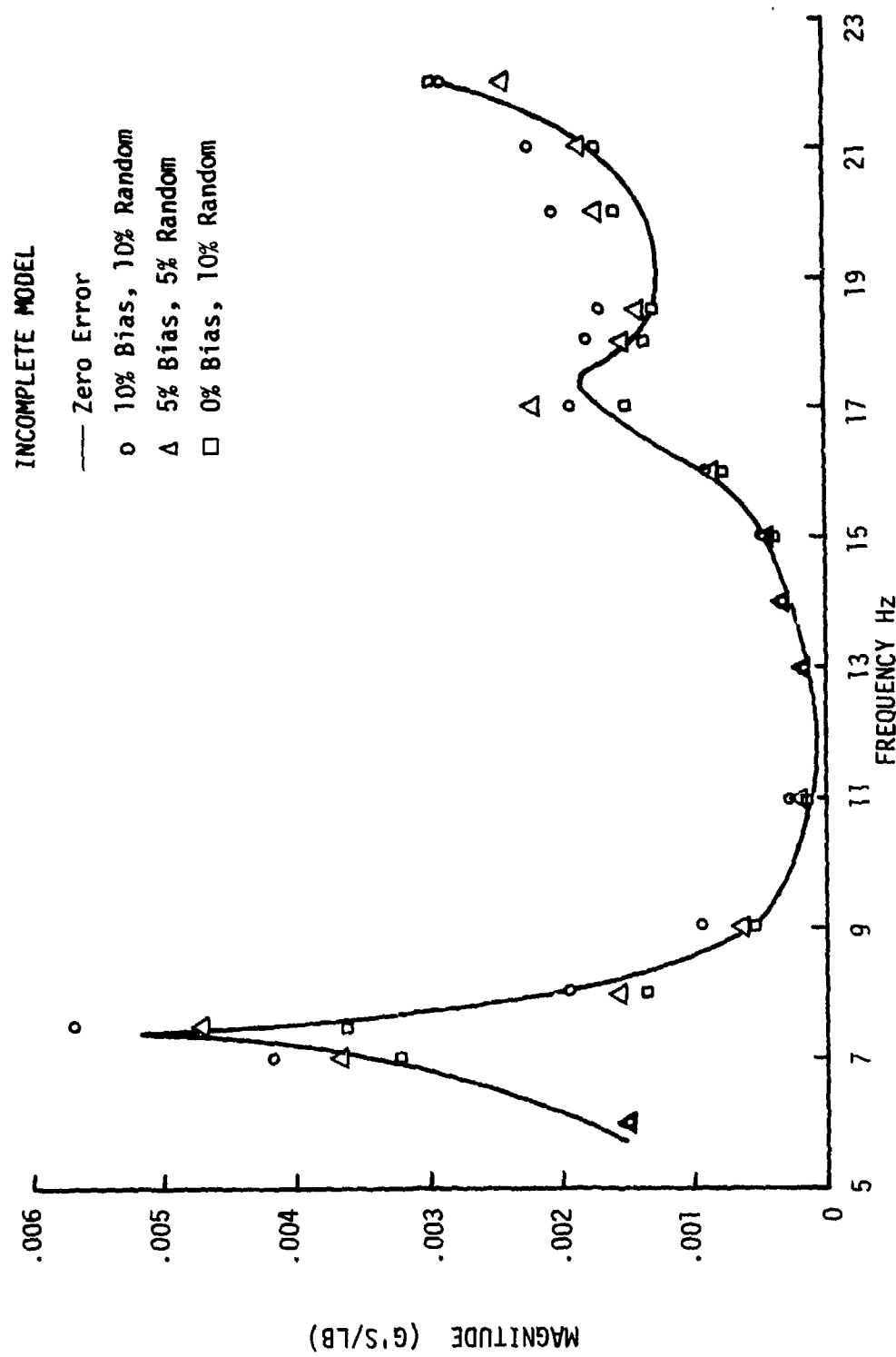
Figure 25.   Effect of error on acceleration mobility magnitude $\ddot{Y}_{Z50,Z485}$.

143
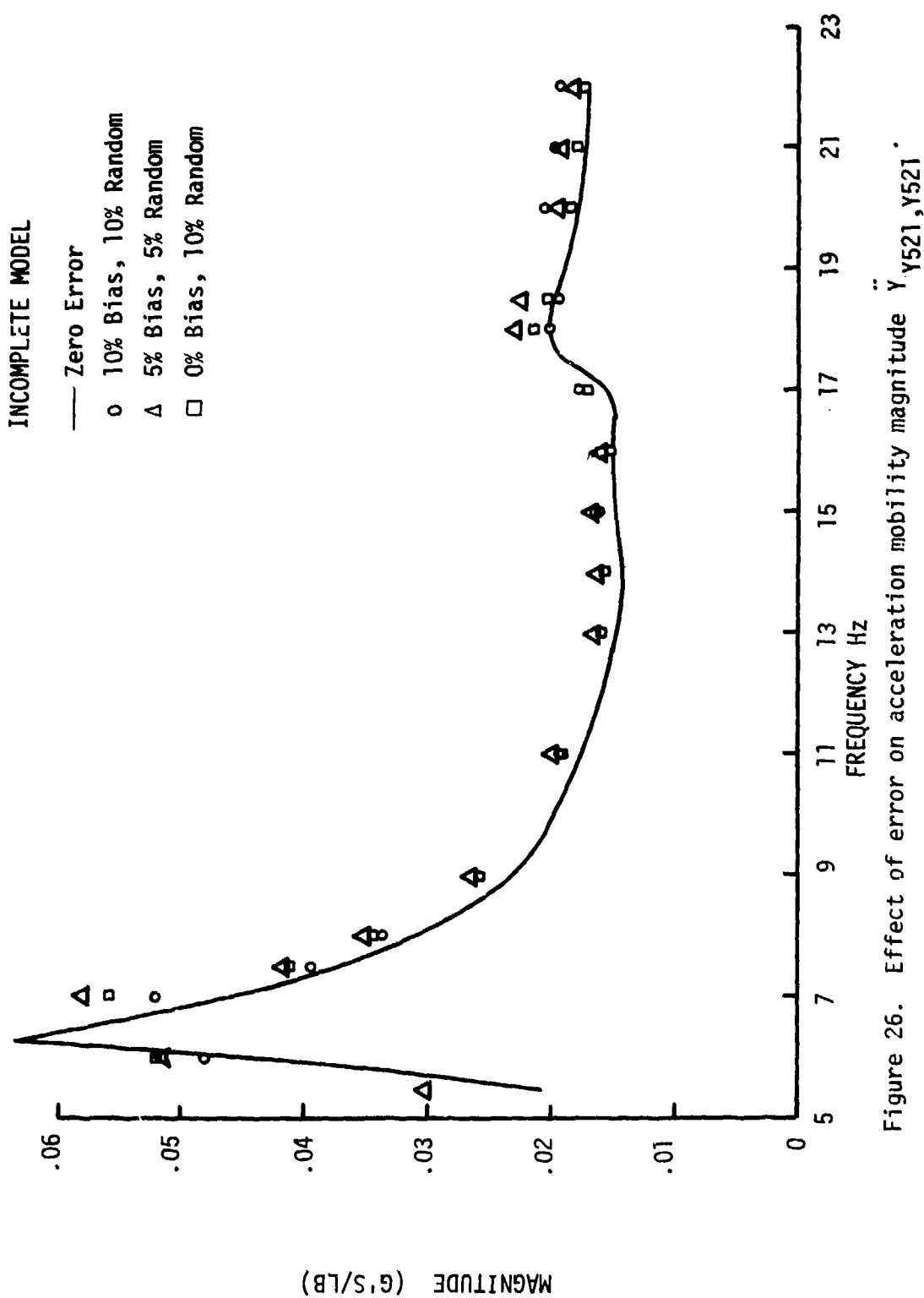
Figure 26. Effect of error on acceleration mobility magnitude $\ddot{Y}_{Y521,Y521}$.

144

Generally, the acceleration mobility frequency response predicted using the Incomplete Model development is relatively insensitive to the level of measurement error applied in the study. The data indicate that even with the high level of error used in the analysis the frequency response is well defined and approximates the no error results. The areas of the frequency response proximate to the natural frequencies are more sensitive to measurement error than are the off-resonance responses   However, even with the high levels of measurement error incorporated in the study, the system natural frequencies can be easily identified.

Introducing the aforementioned levels of error into the mode shapes which were extracted from test measurements affected both the mass and stiffness matrices developed from the Incomplete Model system identification. The respective changes in the mass and stiffness matrices and their sensitivity to measurement error are reflected by the root mean square of the mass and stiffness changes and, more significantly, by the ratio of the root mean square of the changes to the root mean square of the modified mass and stiffness matrices. The ratio of the root mean square of the mass changes to the root mean square of the elements of the mass matrix is representative of the average change in the individual elements to satisfy the incomplete model constraints. Similarly, the parameter referenced to the stiffness matrix reflects the average change in the elements of the stiffness matrix. Tables 55 and 56 present data in root mean square form for the mass and stiffness matrices, respectively. Additionally, the effects of measurement error on selected elements of the mass and stiffness matrices are given in Tables 57 and 58, respectively. Also shown in the tables are the elemental mass and stiffness values for the 92 degree of freedom NASTRAN model. The data indicate that the Incomplete Model methodology yields mass and stiffness matrices that are insensitive to measurement error, at least for the levels of error considered in the analysis.

145

TABLE 55. EFFECT OF MEASUREMENT ERROR ON
INCOMPLETE MODEL MASS MATRIX

% Error		RMS Of Mass Change	RMS Of Mass	RMS Of Mass Change/Mass
Random	Bias			
0	0	.02490	.2665	.0934
5	5	.02063	.2665	.0774
10	0	.02317	.2665	.0869
10	10	.02027	.2665	.0761

TABLE 56. EFFECT OF MEASUREMENT ERROR ON
INCOMPLETE MODEL STIFFNESS MATRIX

% Error		RMS Of Stiff-ness Change	RMS Of Stiffness	RMS Of Stiffness Change/Stiffness
Random	Bias			
0	0	4.2678 + 04	2.7919 + 05	.1529
5	5	4.3006 + 04	2.7919 + 05	.1540
10	0	4.4255 + 04	2.7919 + 05	.1585
10	10	4.1885 + 04	2.7919 + 05	.1500

TABLE 57.   EFFECT OF ERROR ON MASS ELEMENTS

Mass Element Coordinates	92 D.O.F. NASTRAN Model	Incomplete Model			
		0% Random 0% Bias	5% Random 5% Bias	10% Random 0% Bias	10% Random 10% Bias
(23.23)	.9744	1.1647	1.0621	1.0771	1.0808
(25.25)	3.6783	3.6761	3.6743	3.6657	3.6813
(35.35)	2.3522	2.3023	2.2901	2.2959	2.2955
(56.56)	8.0584	8.1556	7.8237	7.7976	8.1717
(60.60)	8.1160	8.1505	8.0465	8.0618	8.1170

TABLE 58.   EFFECT OF ERROR ON STIFFNESS ELEMENTS

Stiffness Element Coordinates	92 D.O.F. NASTRAN Model	Incomplete Model			
		0% Random 0% Bias	5% Random 5% Bias	10% Random 0% Bias	10% Random 10% Bias
(23.23)	6.562+04	1.226+05	1.2676+05	1.349+05	1.328+05
(25.25)	4.036+06	4.083+06	4.0828+06	4.091+06	4.082+06
(35.35)	2.107+05	2.267+05	2.3417+05	2.243+05	2.468+05
(56.56)	1.341+05	1.196+06	1.1681+06	1.147+06	1.158+06
(60.60)	1.327+05	3.288+05	3.0633+05	2.962+05	2.888+05

147

APPLICATION OF FORCE DETERMINATION FORCES

The Force Determination methodology is described in detail in Reference 2;
a brief description of the technique is presented here.

Using Force Determination, the magnitudes and phasings of the vibratory
forces and moments acting on a helicopter can be obtained for the flight
conditions of the mission profile and the calculated loads can be reproduced
on a helicopter during ground vibration tests in a test bay. "Ground flying"
allows fatigue data to be accumulated at a rapid rate, and because the
airframe is tested on the ground conditions pertinent to fatigue damage
are observable. Further, "ground flying" provides the opportunity to
conduct vibration surveys, to monitor acoustic emission, and to evaluate
vibration reduction devices and structural design changes.

Force Determination methodology was recently applied to a Bell AH-1G air-
frame; to implement the technique, 34 strain gage accelerometers were
positioned on the airframe to measure vertical, lateral, and longitudinal
accelerations. The aircraft was flown through typical mission profiles
for each of four gross weight configurations, and the airframe acceler-
ometer signals were recorded yielding a vector of accelerations y for
each flight condition. Subsequently, the aircraft was subjected to ground
vibration tests using both random and sinusoidal force excitation. The
acceleration and force signals were processed using a Fast Fourier Trans-
form analyzer to yield a calibration matrix relating the acceleration
at point i for excitation applied at point j. The acceleration mobility
calibration matrix is given by

$$[\ddot{Y}] = \begin{bmatrix} \partial\ddot{y}_i/\partial F_1 & \partial\ddot{y}_i/\partial F_2 \cdots \partial\ddot{y}_i/\partial F_M \\ \partial\ddot{y}_j/\partial F_1 & \partial\ddot{y}_j/\partial F_2 \cdots \partial\ddot{y}_j/\partial F_M \\ \vdots \\ \partial\ddot{y}_N/\partial F_1 & \cdots \cdots \partial\ddot{y}_N/\partial F_M \end{bmatrix} \qquad (92)$$

148

The calibration matrix consists of N rows, one for each accelerometer location and M columns, one for each position on the airframe at which a force is acting. In the subject program, the main rotor vertical, lateral and longitudinal forces and a lateral force at the tail rotor location were considered.

The acceleration response of a structure at a particular frequency of excitation is expressed by the product of the acceleration mobility matrix and the external forces acting on the structure

$$\{\ddot{y}\} = [\ddot{Y}] \ \{F\} \tag{93}$$

The accelerations and forces are, in general, complex quantities consisting of magnitude and relative phase angle. Therefore, the acceleration mobility matrix consists of complex elements, also. Theoretically, if there are M forces to be determined it is necessary to measure only M acceleration on the airframe. However, the accelerations and the acceleration mobility matrix in equation (93) are measured parameters and are subject to error. Consequently, the solution of equation (93) for forces could yield meaningless results.

To eliminate this effect the property of redundancy is introduced wherein many more accelerations are measured on the airframe compared to the forces which are to be determined. As a result, the calibration matrix of equation (93) becomes rectangular, having many more rows representing the measured airframe accelerations than columns which are associated with the forces to be evaluated. The resulting system of equations can be solved by using the pseudoinverse, which effects a multivariate least squares solution to the problem. Thus, the solution to equation (93) becomes

$$\{F\} = [\ddot{Y}]^{+} \ \ddot{y}$$

or $\tag{94}$

$$\{F\} = \left[[\ddot{Y}]^{T}[\ddot{Y}]\right]^{-1}[\ddot{Y}]^{T} \ \{\ddot{y}\}$$

In equation (94), $[\ddot{Y}]$ is the calibration acceleration mobility matrix that is obtained from analysis of ground vibration test data, $\{\ddot{y}\}$ is the airframe acceleration data acquired from flight tests, and $\{F\}$ is the forces acting on the airframe that are to be determined. Figure 27 is a pictorial representation summarizing the Force Determination process.

In the current program the forces that were determined using the Force Determination methodology of Reference 2 were applied to the improved 92 degree of freedom NASTRAN model of the AH-1G airframe, which was improved via the Incomplete Model methodology. Forces were applied to the improved model at a frequency of 10.8 Hz, which is the main rotor 2/rev source of excitation. The analysis considered main rotor vertical, lateral and longitudinal forces in addition to a lateral force at the tail rotor gearbox to be acting on the airframe. Table 59 presents a summary of the magnitudes and phases of the vibratory forces acting on the airframe for the six flight conditions investigated.

The steady-state equations of motion in matrix form of a linear system with proportional structural damping may be expressed as

$$\left[[M] - \frac{(1+ig)}{\omega^2} \ [K] \right] \{\ddot{y}\} = \{F\} \tag{95}$$

At any forcing frequency, ω, the acceleration response and the force excitation are related by the system impedance matrix

$$[\ddot{Z}] \{\ddot{y}\} = \{\ddot{F}\} \tag{96}$$

From equation (95) the impedance matrix is given by

$$[\ddot{Z}] = [M] - \frac{(1+ig)}{\omega^2} \ [K] \tag{97}$$

The acceleration response at a particular frequency of excitation is given by

$$\{\ddot{y}\} = [\ddot{Z}]^{-1} \{F\} \tag{98}$$

150
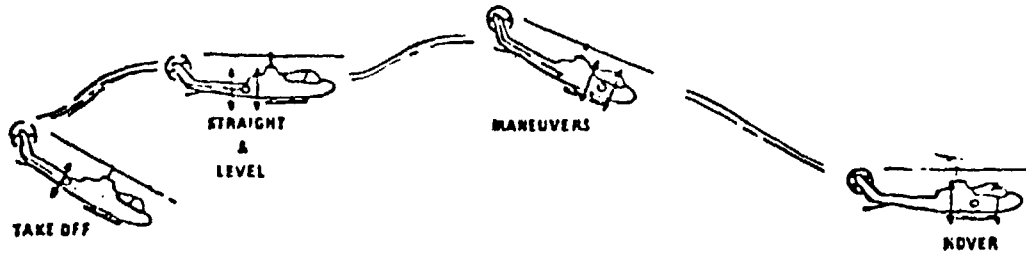
AN AIRCRAFT IS FLOWN THROUGH A TYPICAL MISSION PROFILE.
FIXED SYSTEM MOUNTED ACCELEROMETER SIGNALS ARE RECORDED
NO OTHER INSTRUMENTATION IS REQUIRED.
FROM THIS IN-FLIGHT ACCELERATIONS ARE OBTAINED, OR $\{\ddot{y}\}$
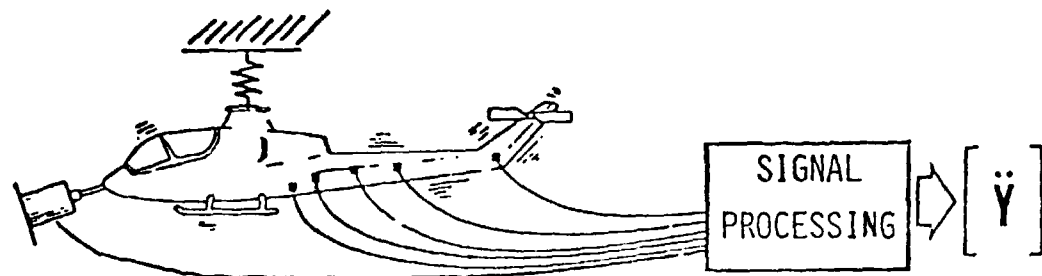
THE AIRCRAFT IS CALIBRATED BY MEANS OF A SHAKE TEST.
ACCELEROMETER AND FORCE SIGNALS ARE PROCESSED TO YIELD
MEASURED ACCELERATION MOBILITY MATRIX OF THE AIRCRAFT.

$$\{F\} = \left[\ddot{Y}\right]^{+} \{\ddot{y}\}$$

CALCULATE MAGNITUDE AND PHASES OF FORCES AND MOMENTS ACTING
ON THE AIRCRAFT IN FLIGHT FROM $\{\ddot{y}\}$ AND $[\ddot{Y}]^{+}$

Figure 27. Force determination process.

151

Equation (98) was used in applying the forces presented in Table 59 to the improved 92 degree of freedom NASTRAN model. The impedance matrix in equation (98) consists of the improved mass and stiffness matrices developed using the Incomplete Model methodology.

At a particular frequency of excitation the impedance matrix and, therefore, the acceleration response of the system depends on the structural damping coefficient.

In calculating the forced response of the AH-1G airframe at the 2/rev, 10.8-Hz, excitation frequency of the main rotor, a structural damping coefficient of .1224 was used which results from the linear variation of damping between the second and third natural frequencies of the system as given in Table 23. The results of applying the main rotor and tail rotor forces obtained from Reference 2 for the six flight conditions considered herein are presented in Tables 60 through 65. The data are shown for the 37 accelerometers used in the program and are identified with respect to the coordinate definition shown in Table 2. Additionally, the magnitude and phase angle of the applied forces and their respective coordinates on the airframe are presented.

Acceleration data for both analysis and flight are also presented in Figures 28 through 33. Generally, the analysis correctly predicts the distribution of acceleration magnitude and phase angle throughout the airframe. The accelerations predicted for the coordinate on the vertical tail pylon do not agree with the test results. A contributing factor is that the location of the accelerometers on the top of the pylon do not coincide with the geometrical location, in terms of fuselage, water line, and butt line stations of the respective degrees of freedom in the NASTRAN model.

TABLE 59. FORCES APPLIED TO IMPROVED NASTRAN MODEL

9500 LB G.W. 196.20 C.G.

FLIGHT CONDITION*

	1		2		3		4		5		6	
	MAG	PHASE	MAG	PHASE	MAG	PHASE	MAG	PHASE	MAG	PHASE	MAG	PHASE
VERT @ HUB	1158	74°	587	41°	1090	169°	1118	20°	3240	77°	2205	46°
LONG @ HUB	447	169°	504	106°	278	164°	225	77°	1036	108°	1224	130°
LATR @ HUB	335	214°	263	213°	124	304°	174	218°	855	222°	610	230°
LATR @ TRGB	81	206°	52	195°	10	231°	6	199°	99	259°	98	230°

* FLIGHT CONDITION

1. Maximum straight and level flight (V_H)

2. 45 degree right turn at .7 V_H

3. Sideward flight right to 35 K_t reverse sideward flight

4. Approach and landing

5. Rolling pullout at V_L – left

6. Rolling pullout right after point target dive to .9 V_L

TABLE 60. ACCELERATION RESPONSE FOR MAXIMUM STRAIGHT AND
LEVEL FLIGHT AT 9500 LB GROSS WEIGHT

Frequency = 10.8 Hz			Structural Damping = 0.122	
Applied Force (lb)				
Direction		Real		Imaginary
Lateral at Tail Rotor Gearbox		-73.		-36.
Longitudinal at hub		439.		-85.
Lateral at hub		-278.		-187.
Vertical at hub		319.		1113.
Accelerometer	Magnitude (g's)		Phase (deg)	
Identification	Analysis	Flight	Analysis	Flight
Z50	.236	0.200	177.	166.
Z100T	.102	0.139	152.	154.
Z210T	.086	0.191	133.	161
Z340	.105	0.309	91.	40.
Z400	.168	0.210	60.	29.
Z460	.143	0.105	150.	304.
Z540	.246	0.494	240.	235.
Z90R	.114	0.078	166.	145.
Z90L	.105	0.120	118.	136.
Z140R	.042	0.056	111.	104.
Z140L	.131	0.101	66.	110.
Z200R	.163	0.171	59.	4.
Z200L	.394	0.283	50.	81.
Z260R	.177	0.182	73.	63.
Z260L	.197	0.222	64.	53.
Z396R	.373	0.122	50.	77.
Z396L	.062	0.260	171.	23.
ZLONG	.092	0.094	63.	65.
ZLATR	.122	0.107	60.	71.
ZCOLL	.160	0.121	68.	80.
Y50	.248	0.037	233.	246.
Y30	.149	0.022	232.	162.
Y140	.100	0.037	225.	144.
Y220B	.087	0.036	35.	111.
Y220T	.523	0.389	214.	232.
Y300	.246	0.206	48.	120.
Y380	.308	0.363	60.	155.
Y440	.310	0.628	75.	172.
Y490	.370	0.474	185.	200.
Y517	1.891	1.123	214.	221.
X140	.068	0.027	23.	86.
X180T	1.244	0.272	172.	141.
X540	.280	0.444	245.	227.
X200R	.141	0.142	27.	48.
X200L	.092	0.114	217.	250.
X190	.081	0.115	36.	70.
X200L	.047	0.027	23.	333.

20
B

154

TABLE 61. ACCELERATION RESPONSE FOR A 45-DEGREE TURN AT 9500 LB GROSS WEIGHT

Frequency = 10.8 Hz			Structural Damping = 0.122	
Applied Force (lb)				
Direction		Real	Imaginary	
Lateral at Tail Rotor Gearbox		- 50.	- 14.	
Longitudinal at hub		139.	485.	
Lateral at hub		-221.	-143.	
Vertical at hub		443.	385.	
Accelerometer	Magnitude (g's)		Phase (deg)	
Identification	Analysis	Flight	Analysis	Flight
Z50	.239	0.226	116.	175.
Z100T	.126	0.120	103.	165.
Z210T	.062	0.204	96.	154.
Z340	.038	0.236	292.	85.
Z400	.102	0.172	310.	357.
Z460	.044	0.031	134.	234.
Z540	.168	0.449	252.	184.
Z90R	.089	0.088	123.	184.
Z90L	.125	0.120	90.	149.
Z140R	.012	0.029	71.	172.
Z140L	.079	0.079	43.	127.
Z200R	.092	0.171	323.	319.
Z200L	.226	0.195	25.	86.
Z260R	.072	0.116	10.	27.
Z260L	.099	0.157	22.	32.
Z396R	.180	0.129	31.	351.
Z396L	.167	0.184	254.	351.
ZLONG	.045	0.052	355.	40.
ZLATR	.063	0.072	16.	57.
ZCOLL	.094	0.076	35.	67.
Y50	.248	0.019	232.	183.
Y30	.142	0.020	231.	180.
Y140	.096	0.024	230.	147.
Y220B	.092	0.046	45.	94.
Y220T	.396	0.328	211.	224.
Y300	.195	0.156	42.	112.
Y380	.145	0.269	19.	144.
Y440	.093	0.474	359.	161.
Y490	.282	0.483	211.	174.
Y517	1.425	0.595	213.	208.
X140	.057	0.029	312.	350.
X180T	1.386	0.333	109.	144.
X540	.101	0.418	231.	176.
X200R	.120	0.143	36.	50.
X200L	.138	0.095	245.	277.
X190	.050	0 105	343.	90.
X200L	.040	0.028	311.	325.

TABLE 62. ACCELERATION RESPONSE FOR SIDEWARD FLIGHT AT 9500 LB GROSS WEIGHT

Frequency = 10.8 Hz		Structural Damping = 0.122	
Applied Force (lb)			
Direction		Real	Imaginary
Lateral at Tail Rotor Gearbox		- 6.	- 8.
Longitudinal at hub		267.	- 77.
Lateral at hub		69.	-103.
Vertical at hub		-1070.	208.

Accelerometer Identification	Magnitude (g's)		Phase (deg)	
	Analysis	Flight	Analysis	Flight
Z50	.104	0.154	167.	217.
Z100T	.074	0.114	171.	196.
Z210T	.092	0.129	183.	219.
Z340	.090	0.267	190.	157.
Z400	.117	0.162	176.	154.
Z460	.150	0.003	170.	108.
Z540	.140	0.295	350.	332.
Z90R	.078	0.103	180.	204.
Z90L	.115	0.113	165.	197.
Z140R	.052	0.093	185.	190.
Z140L	.094	0.111	166.	185.
Z200R	.142	0.111	178.	147.
Z200L	.229	0.234	157.	159.
Z260R	.162	0.198	175.	170.
Z260L	.153	0.220	170.	159.
Z396R	.116	0.151	149.	166.
Z396L	.078	0.145	207.	143.
ZLONG	.068	0.112	183.	172.
ZLATR	.081	0.118	174.	167.
ZCOLL	.129	0.138	171.	172.
Y50	.061	0.101	323.	168.
Y30	.050	0.059	327.	180.
Y140	.035	0.047	316.	185.
Y220B	.017	0.028	49.	174.
Y220T	.239	0.144	309.	307.
Y300	.099	0.056	144.	185.
Y380	.265	0.079	161.	212.
Y440	.417	0.135	164.	245.
Y490	.321	0.081	177.	209.
Y517	.400	0.061	285.	63.
X140	.009	0.029	342.	280.
X180T	.760	0.191	167.	216.
X540	.197	0.298	350.	334.
X200R	.034	0.064	45.	104.
X200L	.053	0.034	291.	353.
X190	.014	0.100	155.	157.
X220L	.007	0.026	334.	77.

TABLE 63. ACCELERATION RESPONSE FOR APPROACH AND LANDING AT 9500 LB GROSS WEIGHT

Frequency = 10.8 Hz			Structural Damping = 0.122	
Applied Force (lb)				
Direction		Real		Imaginary
Lateral at Tail Rotor Gearbox		- 6.		- 2.
Longitudinal at hub		- 51.		249.
Lateral at hub		-137.		-107.
Vertical at hub		1051.		382.

Accelerometer Identification	Magnitude (g's)		Phase (deg)	
	Analysis	Flight	Analysis	Flight
Z50	.097	0.085	100.	122.
Z100T	.065	0.067	78.	75.
Z210T	.082	0.078	43.	133.
Z340	.091	0.277	0.	14.
Z400	.157	0.187	350.	9.
Z460	.122	0.023	5.	200.
Z540	.151	0.504	236.	188.
Z90R	.047	0.021	58.	71.
Z90L	.099	0.074	49.	84.
Z140R	.045	0.035	23.	35.
Z140L	.101	0.073	26.	60.
Z200R	.172	0.111	0.	315.
Z200L	.276	0.195	19.	45.
Z260R	.175	0.162	13.	16.
Z260L	.173	0.198	17.	23.
Z396R	.145	0.173	25.	354.
Z396L	.114	0.227	319.	347.
ZLONG	.080	0.083	15.	20.
ZLATR	.097	0.095	21.	38.
ZCOLL	.141	0.105	23.	37.
Y50	.107	0.058	256.	2.
Y30	.068	0.026	242.	358.
Y140	.043	0.013	240.	18.
Y220B	.036	0.024	98.	92.
Y220T	.335	0.230	214.	221.
Y300	.131	0.079	40.	114.
Y380	.309	0.120	13.	132.
Y440	.472	0.183	9.	162.
Y490	.298	0.141	0.	136.
Y517	.514	0.074	228.	44.
X140	.027	0.019	315.	354.
X180T	.700	0.177	80.	130.
X540	.182	0.483	203.	184.
X200R	.038	0.088	100.	52.
X200L	.060	0.057	261.	280.
X190	.036	0.076	356.	61.
X220L	.018	0.02C	314.	323.

TABLE 64. ACCELERATION RESPONSE FOR A LEFT
ROLLING PULLOUT AT 9500 LB GROSS WEIGHT

Frequency = 10.8 Hz			Structural Damping = 0.122	
	Applied Force (lb)			
Direction		Real	Imaginary	
Lateral at Tail Rotor Gearbox		- 19.	- 97.	
Longitudinal at hub		320.	-985.	
Lateral at hub		-635.	-572.	
Vertical at hub		729.	3157.	
Accelerometer	Magnitude (g's)		Phase (deg)	
Identification	Analysis	Flight	Analysis	Flight
Z50	.468	0.632	126.	137.
Z100T	.329	0.495	114.	120.
Z210T	.263	0.460	105.	169.
Z340	.167	0.943	115.	58.
Z400	.216	0.686	71.	53.
Z460	.275	0.100	105.	38.
Z540	.615	1.299	261.	233.
Z90R	.260	0.320	128.	133.
Z90L	.398	0.480	92.	118.
Z140R	.131	0.221	109.	118.
Z140L	.344	0.408	75.	107.
Z200R	.299	0.206	79.	38.
Z200L	.922	0.895	59.	87.
Z260R	.420	0.515	80.	82.
Z260L	.482	0.692	72.	70.
Z396R	.593	0.450	64.	74.
Z396L	.191	0.778	234.	37.
ZLONG	.187	0.268	80.	82.
ZLATR	.273	0.335	73.	85.
ZCOLL	.434	0.413	80.	93.
Y50	.678	0.422	269.	308.
Y30	.412	0.208	264.	291.
Y140	.273	0.110	258.	269.
Y220B	.179	0.105	72.	166.
Y220T	1.540	0.908	214.	231.
Y300	.584	0.363	65.	154.
Y380	.782	0.732	53.	178.
Y440	.962	1.339	43.	195.
Y490	.312	1.005	325.	332.
Y517	3.484	0.724	243.	264.
X140	.057	0.089	333.	60.
X180T	2.836	0.748	111.	153.
X540	.622	1.311	262.	227.
X200R	.244	0.267	59.	55.
X200L	.336	0.097	243.	279.
X190	.097	0.310	46.	92.
X220L	.035	0.070	327.	28.

TABLE 65. ACCELERATION RESPONSE FOR A RIGHT ROLLING PULLOUT AT 9500 LB GROSS WEIGHT

Frequency = 10.8 Hz			Structural Damping = 0.122	
Applied Force (lb)				
Direction		Real	Imaginary	
Lateral at Tail Rotor Gearbox		- 63.	- 75.	
Longitudinal at hub		287.	-938.	
Lateral at hub		-392.	-467.	
Vertical at hub		1532.	1586.	
Accelerometer Identification	Magnitude (g's)		Phase (deg)	
	Analysis	Flight	Analysis	Flight
Z50	.607	0.651	142.	156.
Z100T	.319	0.440	127.	136.
Z210T	.171	0.517	96.	186.
Z340	.174	0.869	2.	40.
Z400	.390	0.624	354.	32.
Z460	.108	0.107	67.	329.
Z540	.391	1.405	268.	218.
Z90R	.214	0.239	137.	158.
Z90L	.298	0.440	105.	131.
Z140R	.068	0.096	60.	123.
Z140L	.241	0.333	54.	113.
Z200R	.384	0.307	5.	338.
Z200L	.700	0.818	38.	85.
Z260R	.346	0.418	29.	64.
Z260L	.381	0.641	35.	54.
Z396R	.466	0.333	49.	49.
Z396L	.381	0.679	305.	27.
ZLONG	.185	0.224	24.	56.
ZLATR	.232	0.282	34.	73.
ZCOLL	.321	0.323	48.	81.
Y50	.576	0.454	266.	328.
Y30	.330	0.218	261.	316.
Y140	.215	0.093	260.	303.
Y220B	.193	0.077	84.	156.
Y220T	.999	1.033	222.	242.
Y300	.461	0.364	63.	138.
Y380	.612	0.723	26.	163.
Y440	.765	1.240	11.	178.
Y490	.496	0.806	292.	196.
Y517	2.964	1.007	242.	260.
X140	.147	0.073	342.	53.
X180T	3.367	0.908	133.	163.
X540	.352	1.415	230.	212.
X200R	.234	0.254	73.	49.
X200L	.285	0.083	278.	273.
X190	.142	0.282	10.	105.
X220L	.100	0.065	341.	14.

159

Figure 28. Acceleration response for straight and
level flight at a gross weight of 9500 lbs.

--- Analysis
— Flight
Scale 1" = 1 g

--- Analysis
— Flight
Scale 1" = 1 g
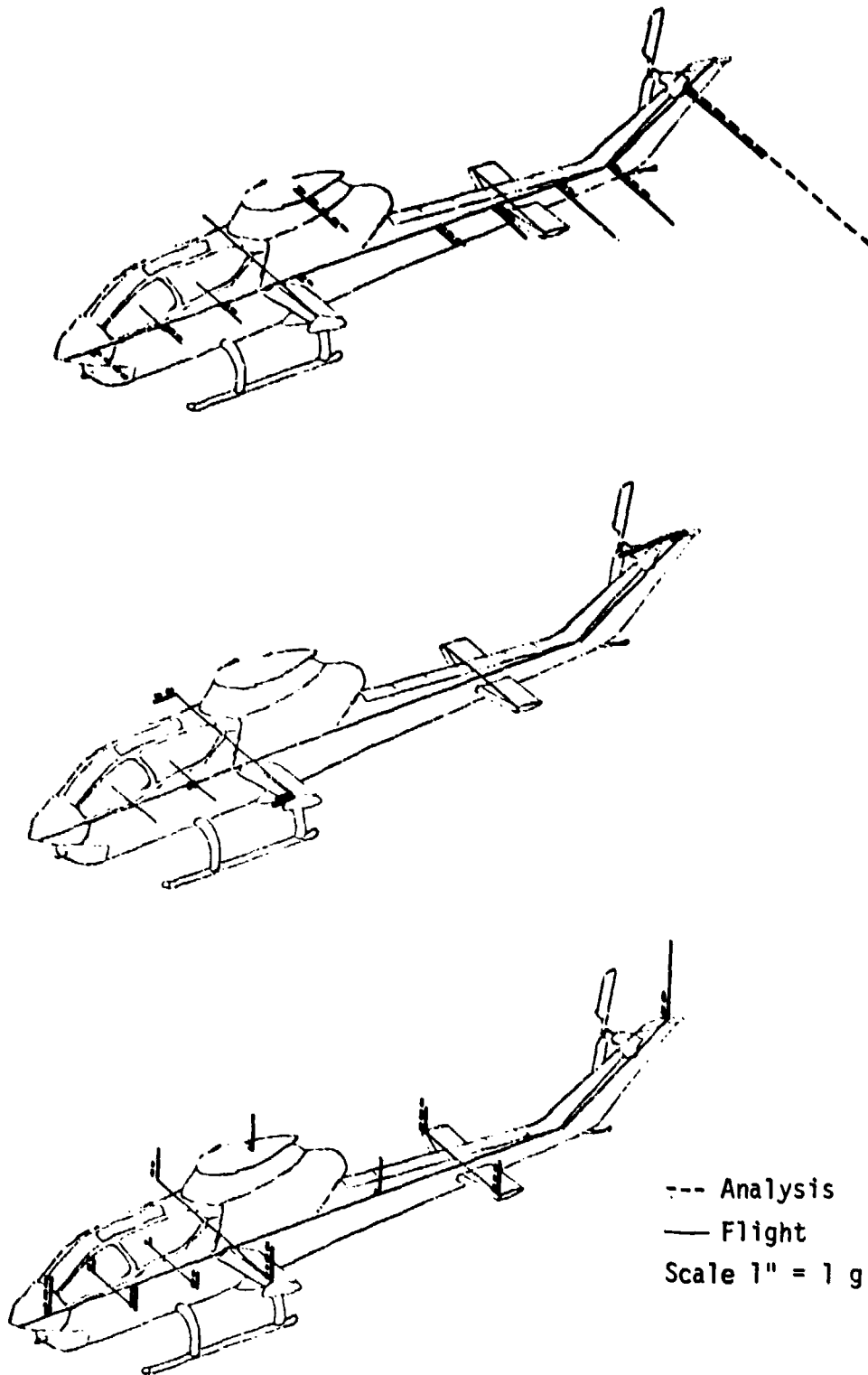
Figure 29. Acceleration response for a 45-degree turn
at a gross weight of 9500 lbs.

161

--- Analysis
— Flight
Scale 1" = 1 g
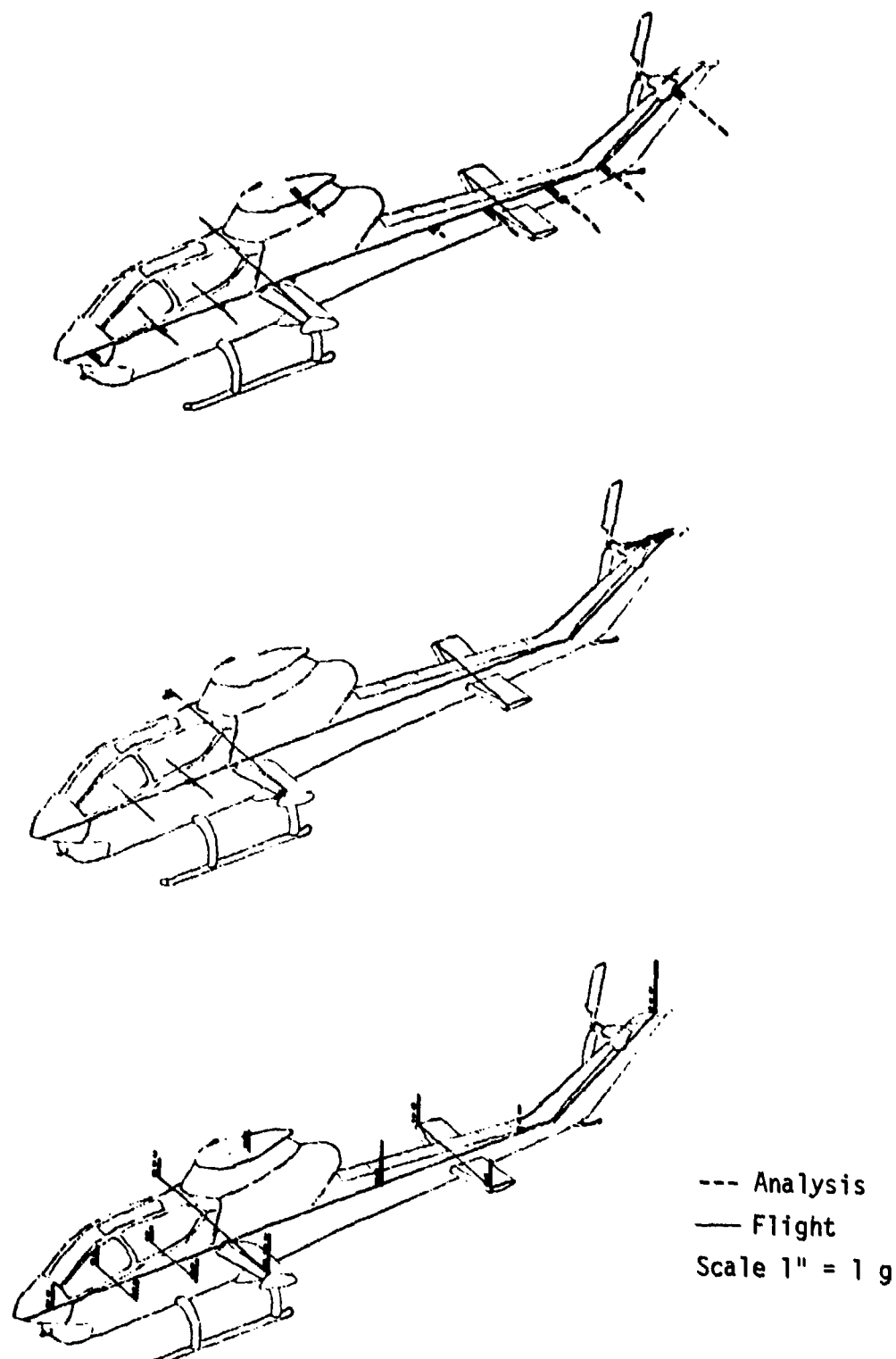
Figure 30.   Acceleration response for sidewalk flight
at a gross weight of 9500 lbs.

162
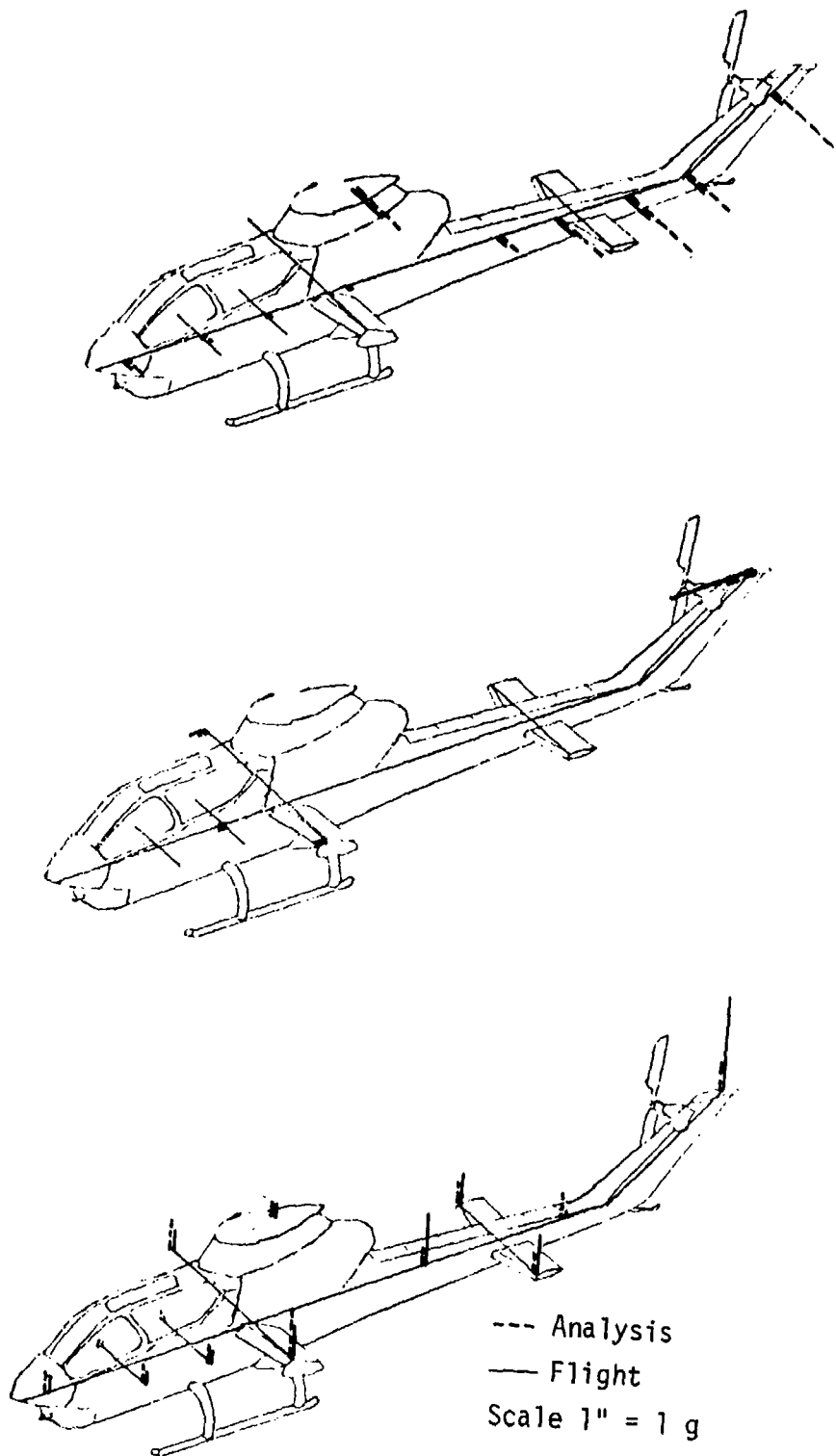
Figure 31. Acceleration response for approach and landing at a gross weight of 9500 lbs.
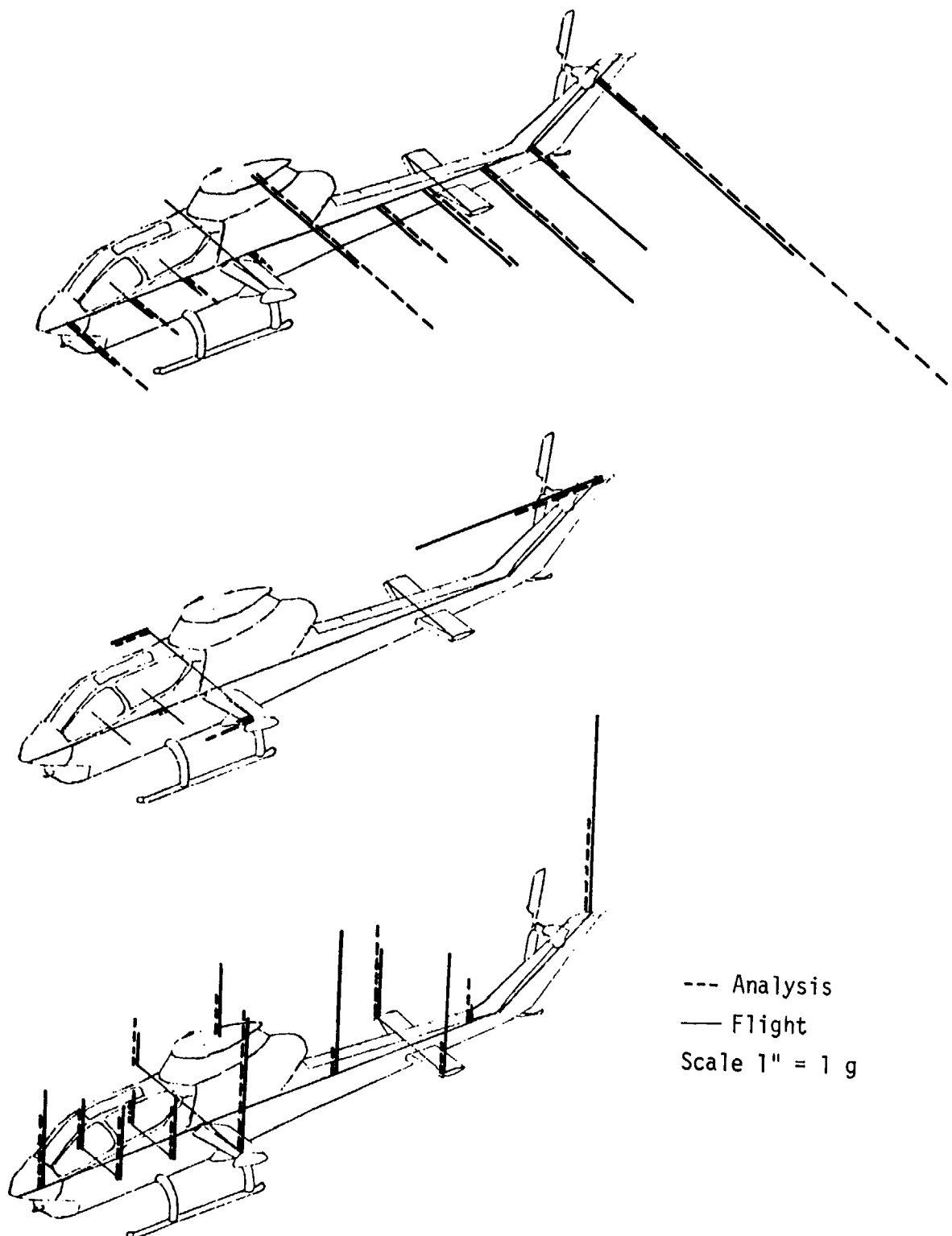
Figure 32. Acceleration response for a left rolling
pullout at a gross weight of 9500 lbs.

--- Analysis
—— Flight
Scale 1" = 1 g
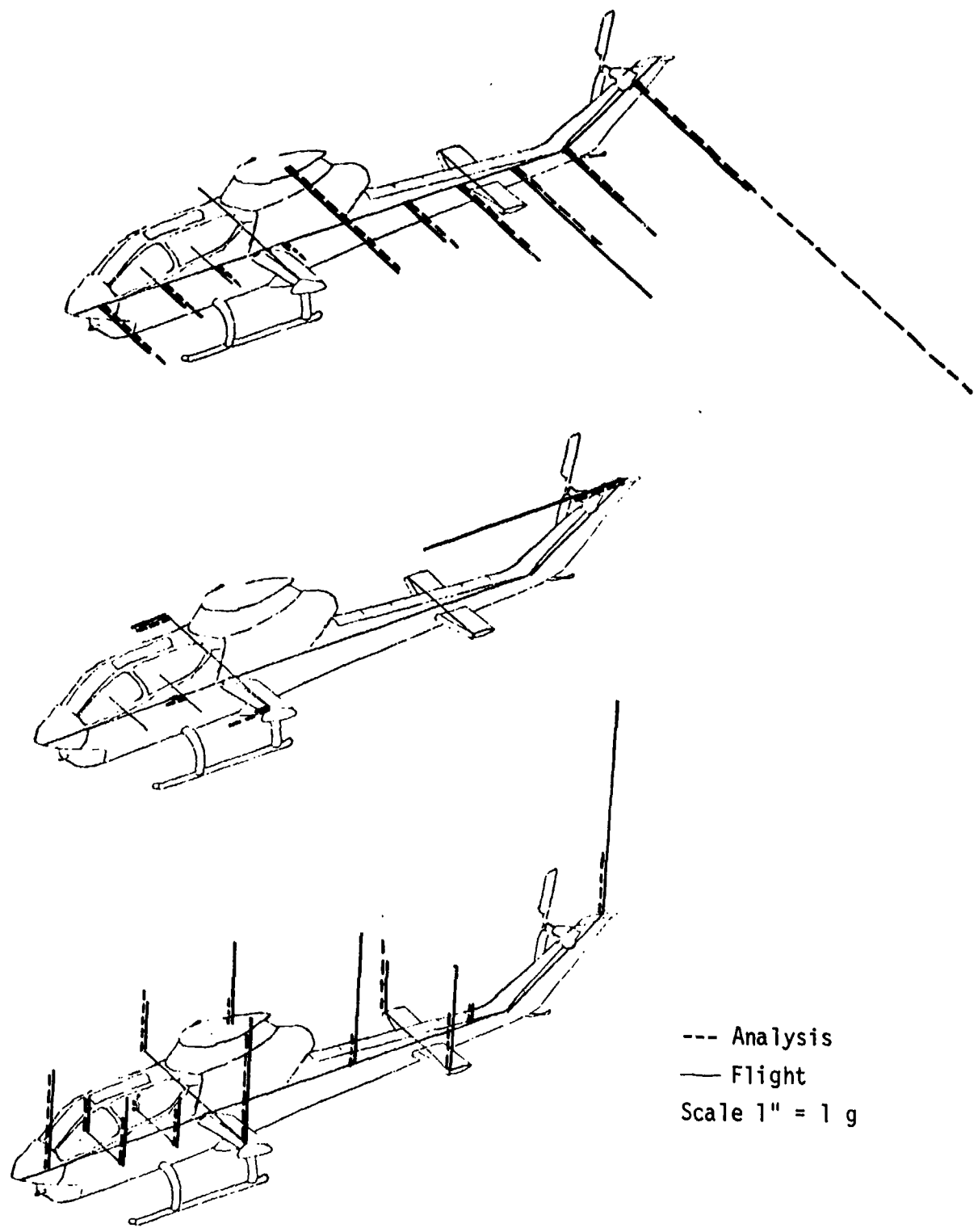
Figure 33. Acceleration response for a right rolling
pullout at a gross weight of 9500 lbs.

--- Analysis
— Flight
Scale 1" = 1 g

165

CONCLUSIONS

1. Techniques were developed and implemented during dynamic tests of the AH-1G airframe which yielded accurate acceleration mobility frequency response data.

2. Analytical methods which were developed at Kaman Aerospace Corporation were applied to dynamic test measurements of the AH-1G airframe and accurately defined the natural frequencies, damping coefficients and complex orthonormal mode shapes in the frequency range 0-25 Hz.

3. Truncated Model system identification was performed successfully on the dynamic test data of the AH-1G airframe. Truncated models can predict the effect of concentrated mass changes and strut type stiffness changes on the natural frequencies and orthonormal modes of the structure.

4. The Incomplete Model methodology was applied to a 92 D.O.F. NASTRAN model of the AH-1G airframe resulting in an improved model which predicted successfully the natural frequencies and frequency response of the structure. Analytical predictions of the vibration characteristics of the airframe using the improved model compared favorably with test data and exhibited significant improvement compared to the predictive capability of the original 92 D.O.F. NASTRAN model.

5. The main rotor and tail rotor forces obtained from Reference 2 were applied to the improved 92 D.O.F. NASTRAN model and the predicted accelerations were in agreement with the accelerations measured in flight.

6. The Incomplete Model method proved to be insensitive to levels of bias and random error applied to the measured orthonormal modes used in the analysis.

7. The method of Done and Hughes was able to predict the effect on natural frequencies and complex orthonormal mode elements resulting from concentrated mass changes and strut type stiffness changes made to the airframe.

RECOMMENDATIONS

Based on the results of this effort, it is recommended that:

1. The Incomplete Model and Truncated Model methodologies, which currently operate on real orthonormal modal data, be extended to incorporate complex modes, thereby improving the vibration prediction capability of the methods.

2. The experimental and analytical procedures that were developed and applied in the current program be applied to a composite structure, such as a helicopter tail cone, to validate and promote acceptance of the methods for all types of structures.

REFERENCES

1. Cronkite, James D., et al. A NASTRAN VIBRATION MODEL OF THE AH-1G
    HELICOPTER AIRFRAME, Vol. 1, USAAMRDL R-TR-74-045, Rock Island
    Arsenal, U. S. Army Air Mobility Research and Development Laboratory,
    Rock Island, Illinois, June 1974, AD-A009482.

2. Jones, R., et al., EXPERIMENTAL VERIFICATION OF FORCE DETERMINATION
    AND GROUND FLYING ON A FULL-SCALE HELICOPTER. Kaman Aerospace Cor-
    poration Report Number R-1625, USAAVRADCOM-TR-81-D-11, Applied Tech-
    nology Laboratory, U. S. Army Research and Technology Laboratory,
    Fort Eustis, Virginia, 23604, May 1981, AD A100182.

3. Guyan, R., Reduction of Stiffness and Mass Matrices. AIAA JOURNAL,
    Vol. 3, No. 2, February 1965, pp. 380.

4. Flannelly, W. G., and Giansante, N., EXPERIMENTAL VERIFICATION OF
    SYSTEM IDENTIFICATION, Kaman Aerospace Corporation, Report Number
    R-1275, USAAMRDL TR-74-64, Eustis Directorate, U. S. Army Air Mobility
    Research and Development Laboratory, Fort Eustis, Virginia 23604,
    August 1974, AD 784190.

5. Cronkhite, James D., and Berry, Victor L., CORRELATION OF THE AH-1G
    AIRFRAME TEST DATA WITH A NASTRAN MATHEMATICAL MODEL. NASA CR-145119,
    February 1976.

6. Berman, A., et al., IMPROVEMENT OF ANALYTICAL DYNAMIC MODELS USING
    MODAL TEST DATA. AAIAA/ASME/ASCE/AHS 21st Structures, Structural
    Dynamics and Materials Conference, May 12-14, 1980, Seattle, Washington.

7. Baruch, M., and Bar Itzhock, I. Y., OPTIMAL WEIGHTED ORTHAGONALIZATION
    OF MEASURED MODES. AIAA Journal, Vol. 16, No. 4, 1978, pp. 346-351.

8. Done, G. T. S., and Hughes, A. D., The Response of a Vibrating Struc-
    ture as a Function of Structural Parameters. Journal of Sound and
    Vibration, Vol. 38, No. 2, 1975.

9. Crandall, S. H., The Roll of Damping in Vibration Theory. Journal
    of Sound and Vibration, Vol. 11, No. 1, 1970.

168

APPENDIX A
DYNAMIC TESTING OF THE AH-1G AIRFRAME

GROUND VIBRATION TESTS

The dynamic testing of the AH-1G airframe was conducted in Kaman Aerospace
Corporation's full-size dynamic test facility. During shake tests the
airframe was suspended using a bungee system to simulate free flight. A
photograph of the airframe suspension system is presented in Figure A-1.
A full view of the airframe in the test facility is shown in Figure A-2.
The electromagnetic shaker system for excitation applied laterally at the
tail rotor gearbox location is presented in Figure A-3. Force excitation
was also applied vertically at the tail skid location and at the hub loca-
tion in the vertical direction.

INSTRUMENTATION

Thirty seven STATHAM Model A69TL strain gage accelerometers were located
on the airframe as described in Reference 2. The accelerometers are
designed for flight and general purpose use with a measurement range of
$\pm$ 5 g's and a natural frequency of approximately 375 Hz. In addition,
55 ENDEVCO Model 2262-25 piezoresistive accelerometers were placed on the
airframe during the present study. The ENDEVCO Model 2262-25 accelerometers
have a rated range of $\pm$ 25g and a natural frequency of approximately 750 Hz.
The accelerometers were rigidly attached to the structure, via mounting
blocks, using existing bolt or connector holes or with appropriate bonding
agents to minimize extraneous localized response effects. Typical acceler-
ometer installations are shown in Figures A-4 and A-5. The accelerometers
shown in the foreground on the wing of the airframe are STATHAM Model A69TL
accelerometers with direction of major sensitivity in the vertical and
longitudinal directions. Also shown in the figure are the ENDEVCO Model
2262-25 with direction of major sensitivity in the vertical direction.
The accelerometers shown in Figure A-5 are ENDEVCO Model 2262-25. The
accelerometer shown in the lower part of the figure is placed with direction
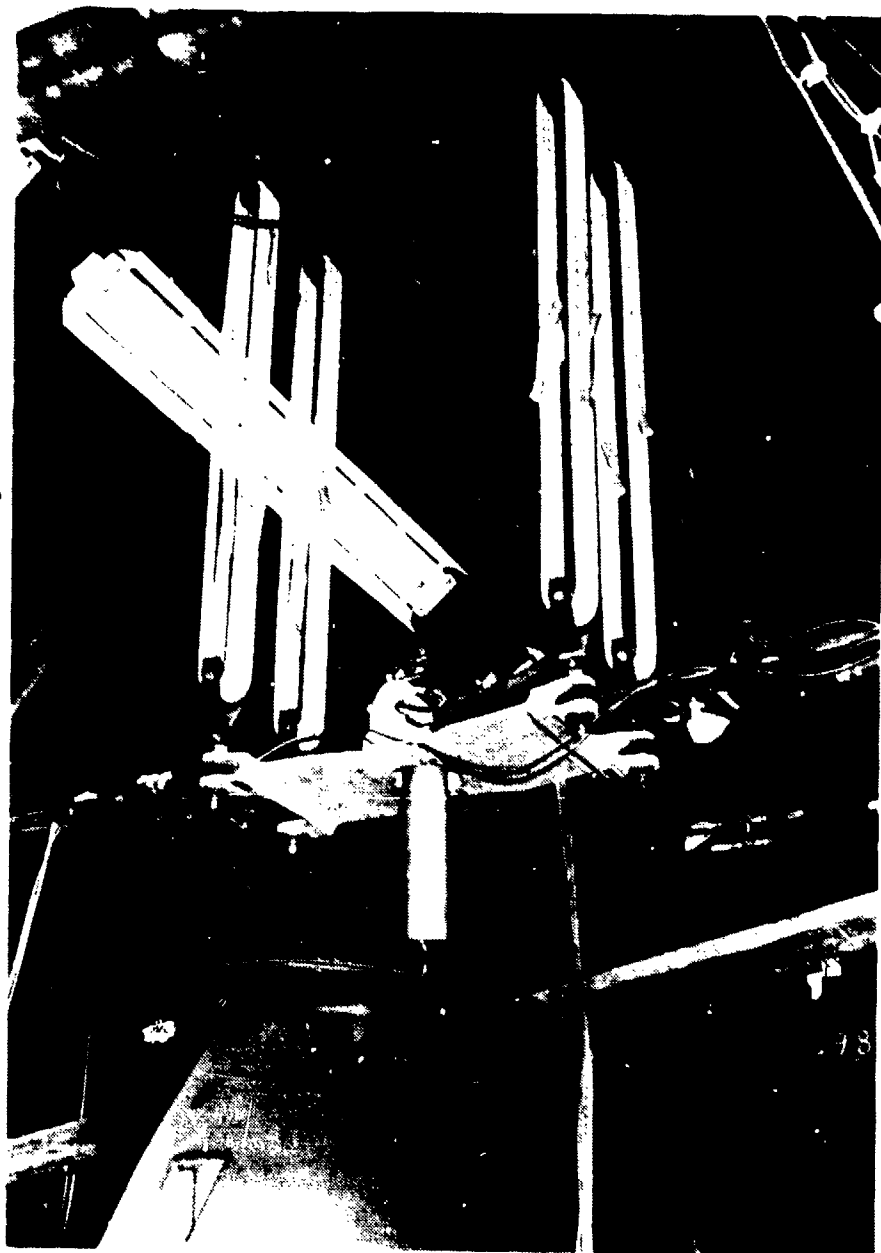
Figure A-1. AH-1G suspension system.

Figure A-2. AH-1G airframe in dynamic test facility.
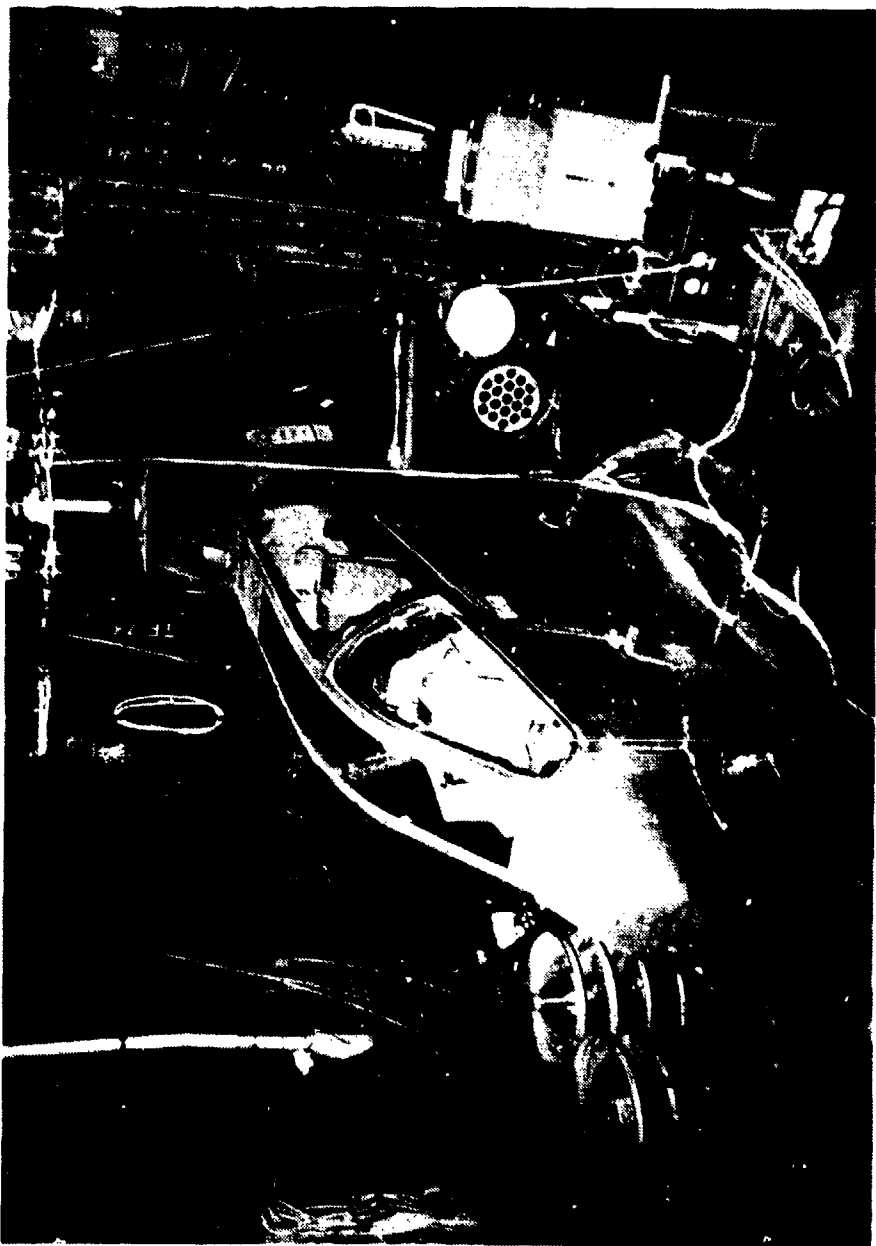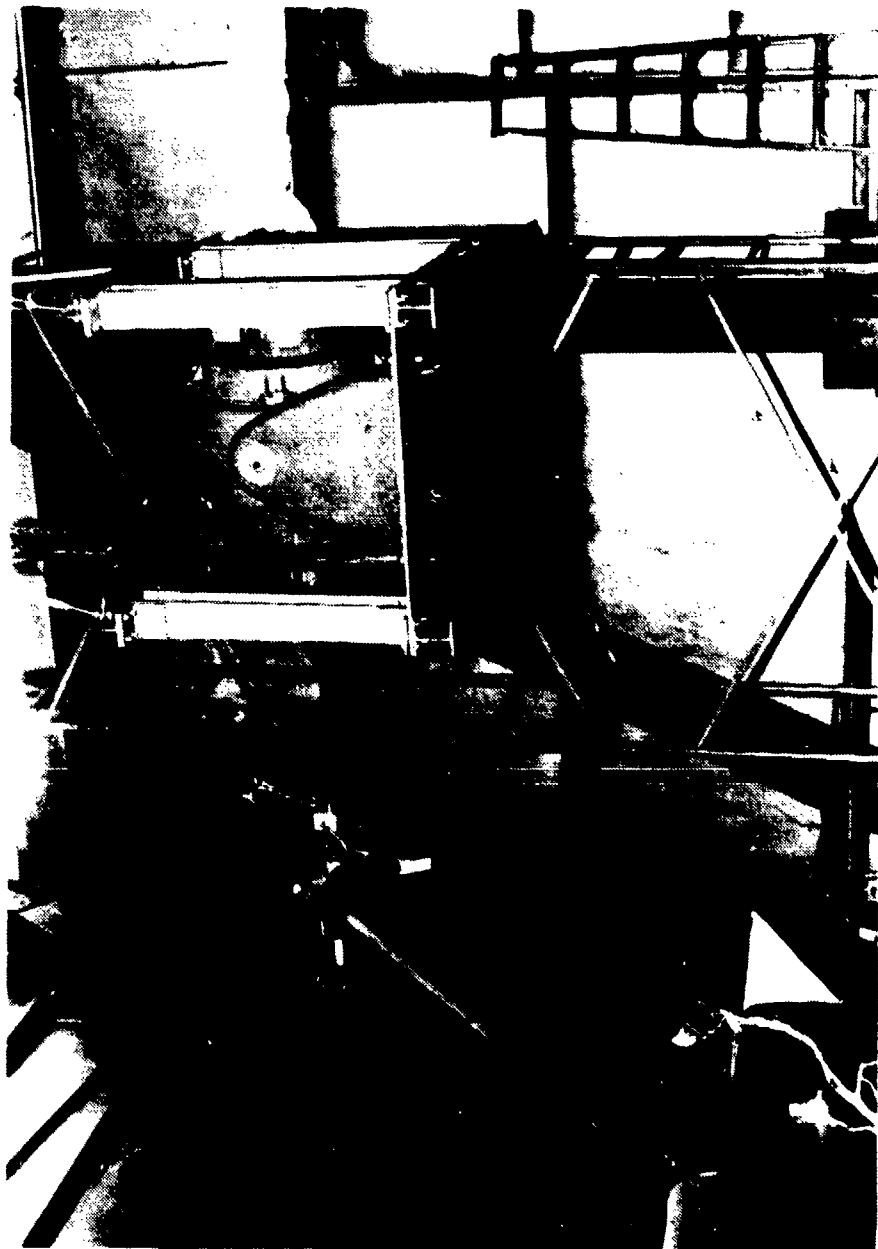
Figure A-3. Lateral excitation at the tail rotor gearbox.

Figure A-4. Typical accelerometer installation on AH-1G wing.

173
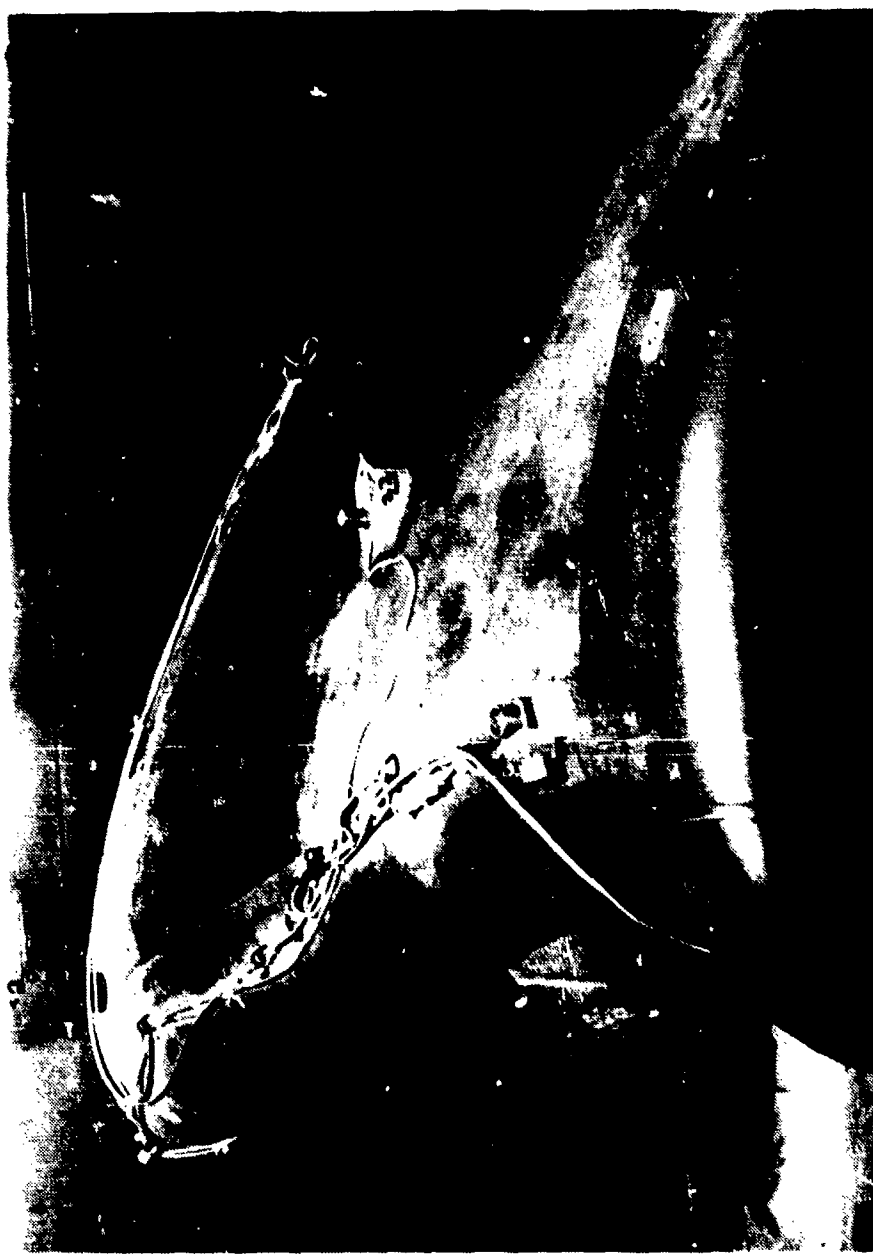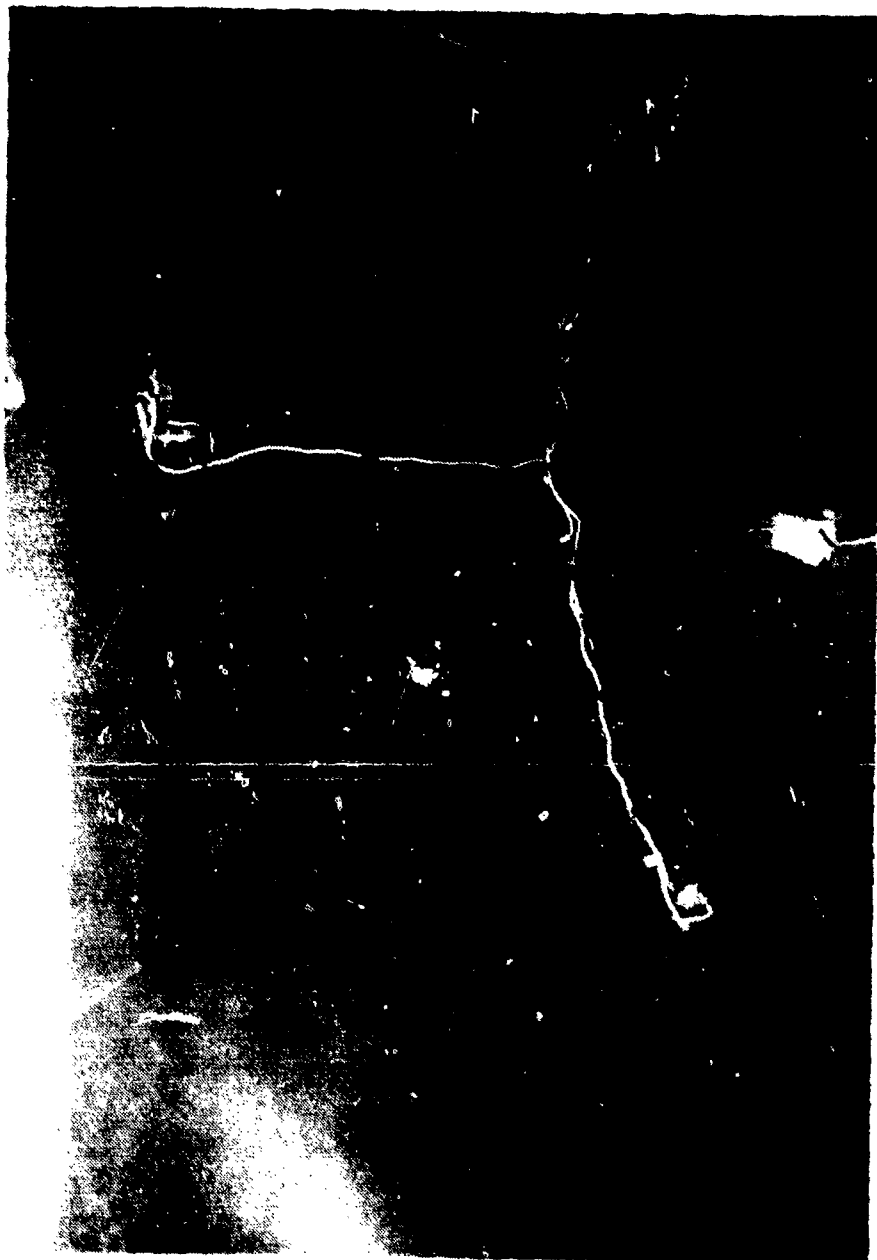
Figure A-5. Typical accelerometer installation on AH-1G airframe.

of major sensitivity in the lateral direction, and the accelerometer in the upper part of the figure is positioned with direction of major sensitivity in the vertical direction. Force was measured using an INTERFACE Load Cell Model 1010-AF.

The accelerometers used in the program were wired to B&I Instrument Model 24-200 balance boxes and bridge power supplies. The balance boxes, used as signal conditioning units, had their output signals directed to a Pulse Code Modulation encoder (PCM). Data signals, at excitation frequencies of interest, were transmitted from the test site, stored on magnetic tape, and processed on the IBM 360/50 to yield the acceleration mobilities of the airframe. Prior to data acquisition and reduction selective accelerometer and force data were processed using the HP5420A Digital Signal Analyzer. Both random and sinusoidal force excitation were used in this phase of the program to check reciprocity and linearity of the mobility acceleration frequency response of the airframe. Figure A-6 presents instrumentation used in the dynamic testing of the AH-1G airframe.

Figure A-6. Test instrumentation.
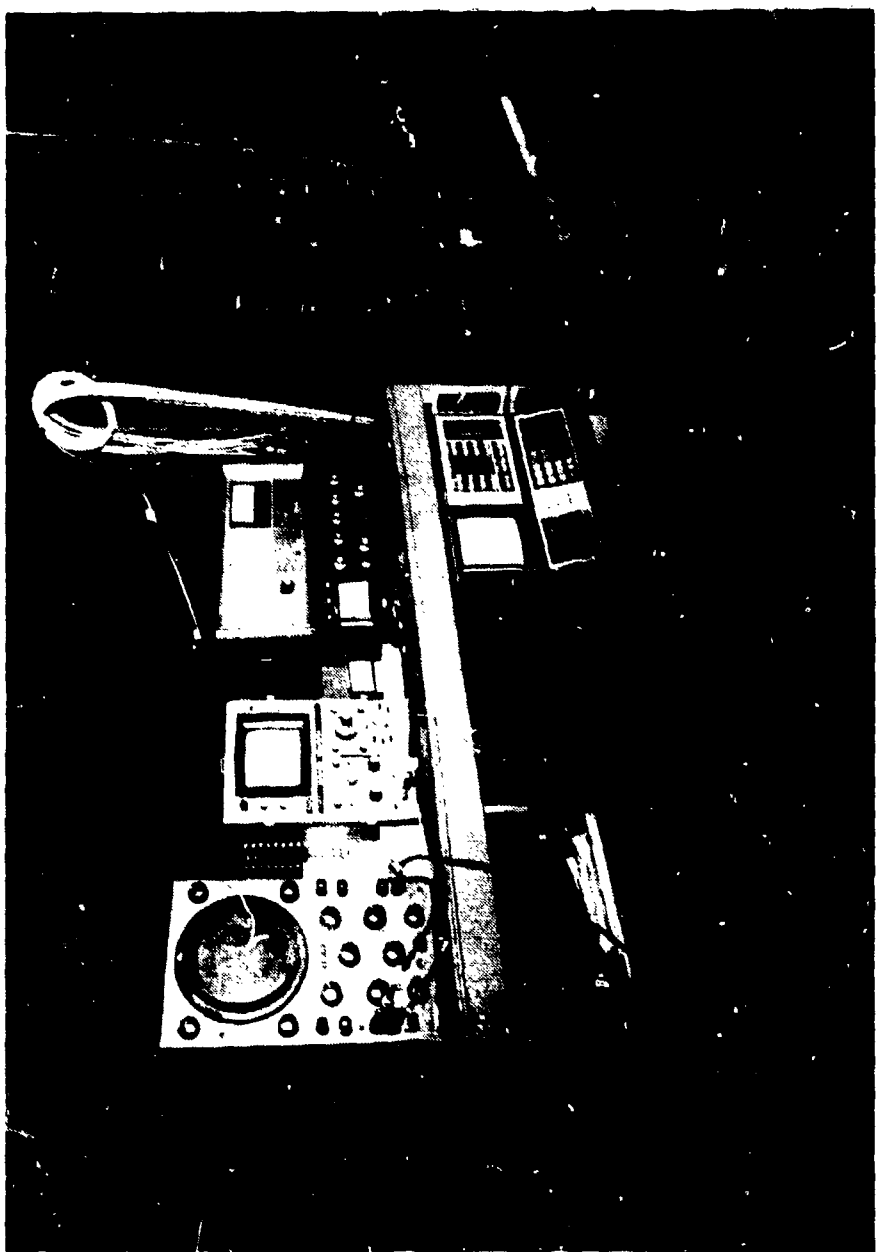
TECHNIQUES AND PROCEDURES FOR VIBRATION
TESTING OF THE AH-1G HELICOPTER

The development of effective techniques for shaking the AH-1G and analyz-
ing the acquired vibration data constituted a major part of the research
work associated with testing. The validity of the methods employed rests
heavily upon the consistency between the measured structural mobilities
and the theoretical models for which these mobilities are derived. This
consistency is critical since the measured mobilities are used not only
for obtaining the global modal parameters of the test vehicle, but also
to derive mobilities which were not measured directly.

Digital signal analyzers have made it possible to measure the response of
structures to any physically realizable excitation. However, the inter-
pretation of measured structure to specified excitation forces is subject
to the mathematical model used in the process of analyzing the data. The
model may be more or less sophisticated, depending on the test data. The
dynamic testing of a structure like the helicopter poses a number of speci-
fic problems. These problems are associated with: (1) the size and com-
plexity of the structure; (2) nonuniform distribution of mass, stiffness
and damping; and (3) the correct application of linear vibration theory
to the process of data acquisition and analysis.

It has been implied that the techniques adopted for the structural dynamic
testing are closely related with the theory underlying the vibration analy-
sis. Therefore, a discussion of the specific test procedures must necess-
arily be preceded by a brief summary of the theoretical considerations in-
cluding: (1) the theory of the generalized linear structure; (2) the prin-
cipal characteristics of acceleration mobility data; (3) testing procedures
for global parameters and the estimation of these parameters; (4) testing
procedures for obtaining mode shapes and the method of calculating mode
shapes; and (5) methods for ing mobilities from modal data.

THEORY OF THE GENERALIZED LINEAR STRUCTURE

The dynamic properties of any structure can always be characterized by a relationship between a selected set of motion coordinates and the set of externally applied forces, i.e.,

$$
\begin{Bmatrix} \text{Motion} \\ \text{Vector} \end{Bmatrix} = \begin{vmatrix} \text{Character of} \\ \text{Structure} \end{vmatrix} \times \begin{Bmatrix} \text{Force} \\ \text{Vector} \end{Bmatrix} \tag{A-1}
$$

The character of the structure implied in equation (A-1) will be termed mobility. If the motion vector is a vector of displacements/velocities/ accelerations, the character of the structure is termed displacement/ veloity/acceleration mobility, respectively.

The central phenomenon of vibration theory is cyclic oscillation, hence the quantities that go into equation (A-1) are generally sought in the frequency-domain; for example, in acceleration measurements

$$
\{\ddot{y}(\omega)\} = [\ddot{Y}(\omega)]\{f(\omega)\} \tag{A-2}
$$

where $\{\ddot{y}(\omega)\}$ is the Fourier transform of the accelerations; $[\ddot{Y}(\omega)]$ is the acceleration mobility matrix; and $\{f(\omega)\}$ is the Fourier transform of the vector of generalized forces, compatible with the selected set of coordinates.

From a measurement standpoint, the jkth element of the matrix $[\ddot{Y}(\omega)]$ relates the acceleration measured along the jth coordinate when the only force acting on the structure is that applied along the kth coordinate; i.e.,

$$
\ddot{y}_j(\cdot) = \ddot{Y}_{jk}(\omega)\, f_k(\omega) \qquad \text{when } f_{i \neq k} = 0 \tag{A-3}
$$

Linear vibration response of a structure may be characterized by the following conditions: (1) the response of the structure to random forcing is stationary in time (i.e., forced vibrations are steady); (2) the elements of the matrix $[\ddot{Y}(\omega)]$ are functions of frequency only, and depend on

178

neither the motion coordinates nor the forcing vector; and (3) the mobility matrix $[\ddot{Y}(\omega)]$ is symmetric; i.e., $Y_{jk} = Y_{kj}$.

The foregoing conditions have specific practical implications in vibration testing and analysis. The first condition is necessary for any structure to survive continuous operation under arbitrary dynamic excitation. The second condition more or less stipulates the type of shake test data that is adequate for analysis based on a linear model of the structure. If the mobility functions measured for different force levels are not the same, the assumption of linearity is not satisfied. This is usually the case when only part of the structure may be participating in the response. As the force level is increased, more and more of the relevant motion coordinates of the structure start to participate in the response. The range of linear response is reached only when the measured mobility remains unchanged with changing force levels. The third requirement is that of reciprocity. If the shaking and measurement stations are interchanged, the same mobility should be recorded, otherwise the $[\ddot{Y}]$ matrix will not be symmetric, as required by the linear model.

In the foregoing characterization of a linear system, no assumptions are made about the nature of the damping mechanisms occurring in the structures. All the conditions required for linear modeling can be verified in the process of the actual shake test of the structure.

The relationship between the Fourier transform of the force vector and that of the displacement vector of a steadily vibrating undamped multiple degree of freedom system can be written as:

$$\left[- \omega^2 \, [M] + [K] \right] \{y(\omega)\} = f(\omega) \tag{A-4}$$

where $[M]$ and $[K]$ are real, symmetric mass and stiffness matrices, respectively. Thus, the displacement mobility matrix for an undamped system is simply

$$[\ddot{Y}(\omega)]_U = \left[- \omega^2 \, [M] + [K] \right]^{-1} \tag{A-5}$$

179

The presence of damping in its most general form can be modeled by introducing a frequency-dependent complex damping matrix into equation (A-5), i.e.,

$$[\ddot{Y}(\omega)]_D = \left[-\omega^2 [M] + [K] + [D^R(\omega)] + i[D^I(\omega)] \right]^{-1} \qquad \text{(A-6)}$$

This analytical development has meaning only in the frequency domain for the general case of damping. This is mainly because the physical quantities that can be used to characterize the arbitrary damping of a structure are related to the energy dissipated per cycle of oscillation. In cases where the time domain, force/motion relationship, representing the damping mechanism is known, the damped equations of motion can be developed in the time domain and then Fourier transformed into the frequency-domain. However, as described in Reference 9, the inverse Fourier transform of the frequency-domain equations that may adequately describe an arbitrarily damped system may not yield a time-domain system of equations that makes physical sense. In other words, arbitrary damping mechanisms may not be susceptible to a time-domain description. Mathematical models, developed from time-domain equations of motion, usually fail to identify global characteristics of structures with significant damping.

In general, the elements of $[D^R(\omega)]$ are small, compared to those of the [K] matrix. Also, in order for reciprocity conditions to be met and for energy to be dissipated, the damping matrix must be symmetric and nonnegative definite over the entire frequency range.

For a damped system, then

$$\left[[K] + i[D(\omega)] - \omega^2 [M] \right] \{y(\omega)\} = \{f(\omega)\} \qquad \text{(A-7)}$$

---

9. Crandall, S. H., The Roll of Damping in Vibration Theory. Journal of Sound and Vibration, Vol. 11, No. 1, 1970.

Consider the complex frequency-dependent characteristic value problem

$$\Big[[K] + i[D(\omega)]\Big]\{\phi\} = \lambda(\omega)[M]\{\phi\} \qquad \text{(A-8)}$$

where $\{\phi\} = \{\phi^R\} + i\{\phi^I\}$ is the complex characteristic vector which can be assumed to be frequency independent; $\lambda(\omega) = \lambda^R(\omega) + i\lambda^I(\omega)$ is the frequency dependent complex eigenvalue.

If combinations of $\Big[\lambda_j(\omega), \{\phi\}_j\Big]$ and $\Big[\lambda_k(\omega), \{\phi\}_k\Big]$ exist, which satisfy equation (A-8), then

$$\{\phi\}_k^T \Big[[K] + i[D(\omega)]\Big]\{\phi\}_j = \lambda_j(\omega)\{\phi\}_k^T [M]\{\phi\}_j \qquad \text{(A-9)}$$

and

$$\{\phi\}_j^T \Big[[K] + i[D(\omega)]\Big]\{\phi\}_k = \lambda_k(\omega)\{\phi\}_j^T [M]\{\phi\}_k \qquad \text{(A-10)}$$

$\{\phi\}^T$ denotes the transpose of $\{\phi\}$. By virtue of the symmetry of the $[K]$, $[M]$ and $[D(\omega)]$ matrices, equations (A-9) and (A-10) lead to the following orthogonality relationships:

$$\{\phi\}_j^T [M] \{\phi\}_k = m_j\, \delta_{jk} \qquad \text{(A-11)}$$

and

$$\{\phi\}_j^T \Big[[K] + i[D(\omega)]\Big]\{\phi\}_k = \Big[k_j + id_j(\omega)\Big]\, \delta_{jk} \qquad \text{(A-12)}$$

where

$$m_j = \{\phi\}_j^T [M] \{\phi\}_j \qquad \text{(A-13)}$$

$$k_j = \{\phi\}_j^T [K] \{\phi\}_j \qquad \text{(A-14)}$$

$$d_j(\omega) = \{\phi\}_j^T [D(\omega)] \{\phi\}_j \qquad \text{(A-15)}$$

$$\delta_{jk} = \begin{matrix} 0, & j \neq k \\ 1, & j = k \end{matrix} \qquad \text{(A-16)}$$

It follows that

$$\{\phi\}_j^T \left[[K] - \omega^2 [M] + i[D(\omega)] \right] \{\phi\}_k = \left[k_j - \omega^2 m_j + id_j(\omega) \right] \delta_{jk}$$

$$= \left[\lambda_j(\omega) - \omega^2 m_j \right] \delta_{jk} \qquad (A-17)$$

If the vectors $\{\phi\}_j$ exist, it can easily be verified that only the imaginary parts of $\lambda_j(\omega)$ need be frequency dependent. So that

$$\lambda_j(\omega) = \lambda_j^R + i \lambda_j^I(\omega) \qquad (A-18)$$

By post-multiplying the transpose of equation (A-8) by $\{\phi\}_j^*$, which is the complex conjugate of $\{\phi\}_j$, the following equation is obtained:

$$\{\phi\}_j^T \left[[K] - i[D(\omega)] \right] \{\phi\}_j^* = \lambda_j(\omega) \{\phi\}_j^T [M] \{\phi\}_j^* \qquad (A-19)$$

Similarly, the complex conjugate of equation (A-8) can be premultiplied by $\{\phi\}_j^T$ to get

$$\{\phi\}_j^T \left[[K] - i[D(\omega)] \right] \{\phi\}_j^* = \lambda_j^*(\omega) \{\phi\}_j^T [M] \{\phi\}_j^* \qquad (A-20)$$

From equations (A-19) and (A-20)

$$\lambda_j(\omega) + \lambda_j^*(\omega) = 2 \{\phi\}_j^T [K] \{\phi\}_j^* / \{\phi\}_j^T [M] \{\phi\}_j^* \qquad (A-21)$$

and

$$\lambda_j(\omega) - \lambda_j^*(\omega) = 2i \{\phi\}_j^T [D(\omega)] \{\phi\}_j^* / \{\phi\}_j^T [M] \{\phi\}_j^* \qquad (A-22)$$

The right-hand side of equation (A-21) is a frequency independent quantity. However, the right-hand side of equation (A-22) is frequency dependent, establishing the validity of the claim made in equation (A-18).

182

A complex L x N modal matrix $[\Phi]$ can be defined such that its jth column is the L x 1 vector $\{\phi\}_j$; j = 1, 2, ...N, where L is the number of coordinates chosen to describe the system and N is the number of modes of the system. In principle, N is infinite; however, in practice, over a given frequency range, only a finite number of system modes are necessary.

Equation (A-7) can be rewritten to give

$$\{y(\omega)\} = [\Phi]\left[[\Phi]^T\Big([K] - \omega^2[M] + i[D(\omega)]\Big)[\Phi]\right]^{-1}[\Phi]^T\{f(\omega)\} \qquad (A\text{-}23)$$

and, using the orthogonality relationships, leads to the results

$$\{y(\omega)\} = [\Phi]\left[\frac{1}{\left[(\lambda_j^R - \omega^2) + i\lambda_j^I(\omega)\right]m_j}\right][\Phi]^T\{f(\omega)\} \qquad (A\text{-}24)$$

By definition, $\{y(\omega)\} = [Y(\omega)]\{f(\omega)\}$; hence,

$$[Y(\omega)] = \sum_{n=1}^{N}\left[\frac{\{\phi\}_n\{\phi\}_n^T}{m_n}\right]\frac{1}{(\lambda_n^R - \omega^2) + i\lambda_n^I(\omega)} \qquad (A\text{-}25)$$

λ_n^R and $\lambda_n^I(\omega)$ have units of $(\text{frequency})^2$, and from physical considerations, both λ_n^R and $\lambda_n^I(\omega)$ are positive. Therefore, it is possible to define

$$\lambda_n^R \equiv \Omega_n^2 \qquad (A\text{-}26)$$

and

$$\lambda_n^I(\omega) \equiv g_n(\omega)\Omega_n^2 \qquad (A\text{-}27)$$

The matrix of modal acceleration coefficients of the nth mode is defined as

$$[A]_n \equiv \frac{1}{m_n}\{\phi\}_n\{\phi\}_n^T \qquad (A\text{-}28)$$

183

The acceleration mobility matrix and the displacement mobility matrix are related by

$$[\ddot{Y}(\omega)] = -\omega^2 [Y(\omega)] \tag{A-29}$$

Using equations (A-26), (A-27), (A-28), and (A-29), the jkth acceleration mobility can be written as

$$\ddot{Y}_{jk}(\omega) = -\sum_{n=1}^{N} A_{jkn} \frac{\omega^2/\Omega_n^2}{(1 - \omega^2/\Omega_n^2) + ig_n(\omega)} \tag{A-30}$$

and $A_{jkn} = A_{jkn}^R + i A_{jkn}^I$, which is the complex modal acceleration for response at coordinate j and force excitation k for mode n.

Ω_n = the natural frequency of the nth mode

g_n = damping coefficient of the nth mode

ω = frequency of excitation

In the most general case, the dependence of $g_n(\omega)$ on frequency may not be known. However, it is expedient to take advantage of the fact that the $ig_n(\omega)$ term in equation (A-30) is dominant only in the frequency range near the natural frequency of the nth mode where $\omega^2/\Omega_n^2 \simeq 1$. Thus, any suitable representation of $g_n(\omega)$ which matches the correct value in the neighborhood of $\omega = \Omega_n$ may be assumed.

The general form of the jkth element of the acceleration mobility matrix can be written as

$$\ddot{Y}_{jk} = \ddot{Y}_{jk}^R + i\ddot{Y}_{jk}^I = E_{jk}^R + iE_{jk}^I - \sum_{n=1}^{N} A_{jkn} \frac{\omega^2/\Omega_n^2}{(1 - \omega^2/\Omega_n^2) + ig_n(\omega)} \tag{A-31}$$

where $E_{jk}^R + iE_{jk}^I$ represents the rigid body acceleration coefficients. In most cases, E_{jk}^I is very small compared to the rest of the terms in the series and is usually neglected.

184

CHARACTERISTICS OF ACCELERATION MOBILITY DATA

MODE FREQUENCY FUNCTIONS

The real and imaginary parts of $\ddot{Y}_{jk}$ can be written as

$$\ddot{Y}_{jk}^{R} = E_{jk}^{R} - \sum_{n=1}^{N} \left[A_{jkn}^{R} \ddot{F}_{n}^{R}(\omega) - A_{jkn}^{I} \ddot{F}_{n}^{I}(\omega) \right] \tag{A-32}$$

and

$$\ddot{Y}_{jk}^{I} = E_{jk}^{I} - \sum_{n=1}^{N} \left[A_{jkn}^{I} \ddot{F}_{n}^{R}(\omega) + A_{jkn}^{R} \ddot{F}_{n}^{I}(\omega) \right] \tag{A-33}$$

or

$$\ddot{Y}_{jk} = E_{jk}^{R} + iE_{jk}^{I} - \sum_{n=1}^{N} A_{jkn} \ddot{F}_{n}(\omega) \tag{A-34}$$

where the mode functions are defined as

$$\ddot{F}_{n}^{R}(\omega) \equiv \frac{\omega^2/\Omega_n^2 \ (\omega^2/\Omega_n^2 - 1)}{(\omega^2/\Omega_n^2 - 1)^2 + g_n^2} \tag{A-35}$$

$$\ddot{F}_{n}^{I}(\omega) \equiv \frac{g_n \ \omega^2/\Omega_n^2}{(\omega^2/\Omega_n^2 - 1)^2 + g_n^2} \tag{A-36}$$

and

$$\ddot{F}_{n}(\omega) = \ddot{F}_{n}^{R}(\omega) + i\ddot{F}_{n}^{I}(\omega) \tag{A-37}$$

Equations (A-32), (A-33), and (A-34) represent the measured acceleration mobility as a linear combination of the mode functions.

185

Plots of $\ddot{F}^R(\omega)$ and $\ddot{F}^I(\omega)$ as functions of frequency ratio for three values of the damping coefficient are shown in Figure A-7. The Nyquist plots of the complex $\ddot{F}(\omega)$ functions are shown in Figure A-8.

The $\ddot{F}^R(\omega)$ function is characterized by two peaks at

$$\omega_{1n} = \Omega_n \sqrt{1 + g_n^2 - g_n \sqrt{1 + g_n^2}} \tag{A-38}$$

and

$$\omega_{2n} = \Omega_n \sqrt{1 + g_n^2 + g_n \sqrt{1 + g_n^2}} \tag{A-39}$$

while the $\ddot{F}^I(\omega)$ function has only one peak at $\omega_{3n} = \Omega_n \sqrt{1 + g_n^2}$ Note that

$$\frac{\omega_{2n}^2 - \omega_{1n}^2}{\Omega_n^2} = 2 g_n \sqrt{1 + g_n^2} \tag{A-40}$$

which increases with increased damping.

From the plots in Figure A-7, it is seen that linear combinations of $\ddot{F}^R$ and $\ddot{F}^I$ vary rapidly in the vicinity of the natural frequency, and are either negligible or slowly varying with frequency in the regions away from the natural frequency.
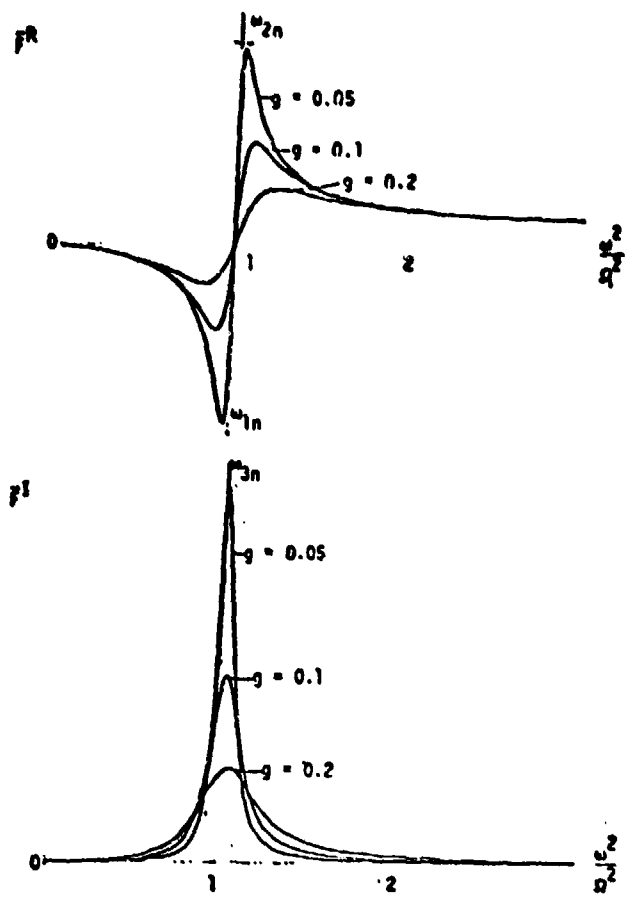
Figure A-7. Complex mode functions.
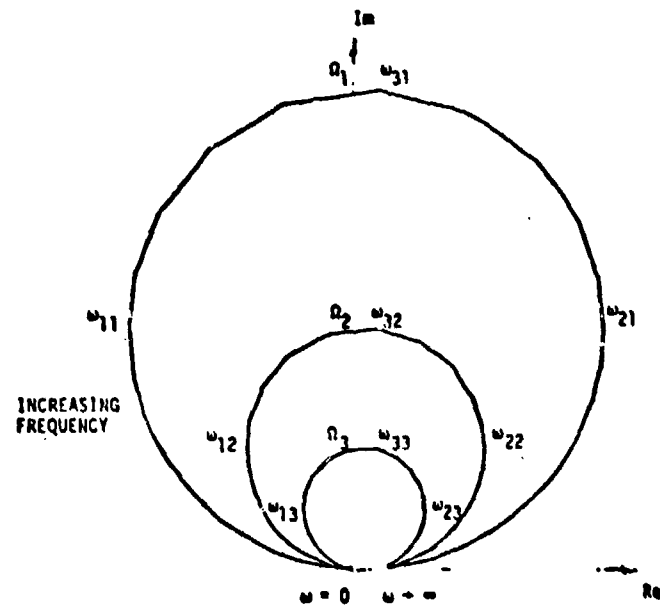
Figure A-8. Nyquist diagram of the complex mode function.

187

<u>Separated Modes</u> - Equation (A-31) carries the basic implication that the effects of the structure's modes occurring at different frequencies on the measured mobility are additive in the frequency domain. If a mode occurs at a frequency, in the neighborhood of which the contributions from the other modes of the structure are either negligible or are weakly varying with frequency, such a mode is said to be well separated. The nature of the measured mobility in this frequency range will be dominated by that particular mode.

<u>Classical Modes</u> - In the case of a classical mode, i.e., when the system mode shape is the same for the damped system as it would be for the undamped system the A_{jkn} is a real number $\left(A^I_{jkn} = 0 \right)$, and the real part of the measured acceleration mobility will show two turning points for each separated mode and the imaginary part will show a single turning point only. For a classical mode, equation (A-40) can be approximated to give an estimate of the damping coefficient: $g_n \simeq (\omega_{2n} - \omega_{1n})/\Omega_n$.

<u>Complex Modes</u> - For the general case of nonclassical or complex modes, both A^R_{jkn} and A^I_{jkn} are significant. The measured real and imaginary mobilities of a well-separated mode contain linear combinations of both $\ddot{F}^R(\omega)$ and $\ddot{F}^I(\omega)$ in proportions given in equations (A-32) and (A-33). In particular, if $A^I_{jkn} \gg A^R_{jkn}$, it is the imaginary part of the acceleration mobility which will show two turning points, while the real part will show a single turning point only.

188

<u>Coupled Modes</u> - System modes, occurring in frequency ranges such that their mutual contributions to the measured mobility in this frequency range are rapidly varying functions of frequency, are said to be coupled.

<u>Mode Clusters</u> - A mode cluster (or a cluster of modes) is characterized by a group of system modes which are coupled together by virtue of the proximity of their resonances. Mode clusters are usually separated by regions of negligible or slowly varying mobility values in the frequency domain.

Mode clusters generally have the appearance of single modes in wideband, low frequency resolution mobility measurements. Higher resolution data usually helps to reveal the modal content of a particular mode cluster. Figure A-9 shows broad band (0 - 200 Hz) mobility of a helicopter vertical tail shake, measuring vertical acceleration at the nose. Between mode clusters, measured mobility varies slowly close to the zero value. In fact, what appears to be a single mode in the 0 - 10 Hz frequency range is actually a cluster of two modes as shown in Figures 4a and 4b, which are higher resolution measurement of the same mobility in the 5 - 10 Hz range.

Identification of mode clusters is useful in determining which modes should be included when truncating equation (A-31) and in identifying frequency bandwidths for higher resolution data acquisition.
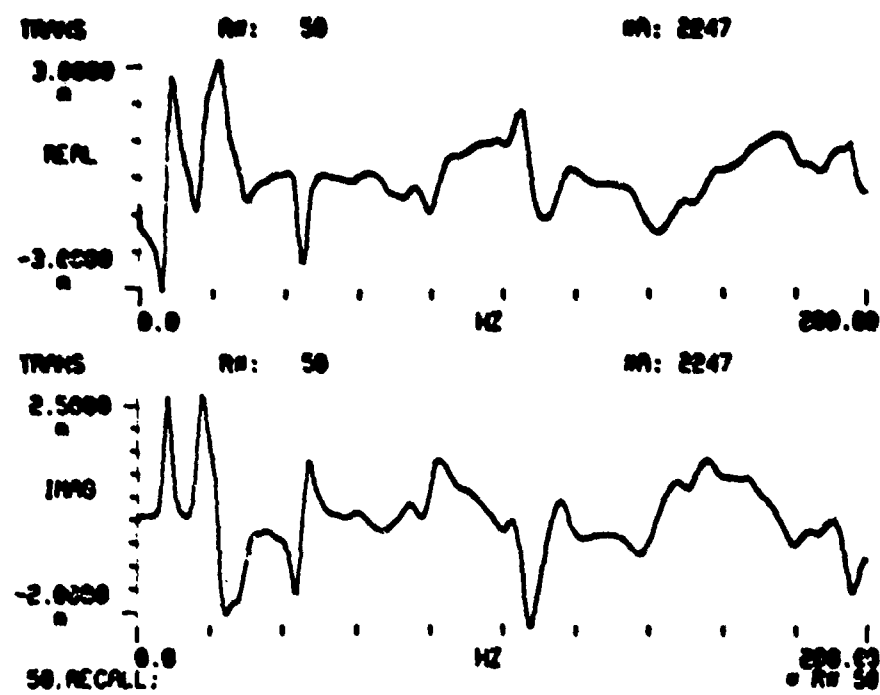
Figure A-9. Measured acceleration mobility of the AH-1G between 0 Hz and 200 Hz.

SHAKE TESTING FOR GLOBAL PARAMETERS

Each elastic mode of a structure is characterized by a natural frequency, Ω_n, and a damping coefficient, g_n, which are global properties of the structure. These are the only constants that enter into the mode frequency functions. They are the same for a given mode, regardless of the response coordinate. The first stage of modal testing is to determine the global parameters of the dominant elastic modes which occur in the frequency range of interest.

The experimental data required for determining the global parameters are the continuous frequency plots of a number of mobilities which are considered to represent the global vibrational behavior of the structure. For a selected set of shaking locations, e.g., tail vertical and tail rotor gearbox lateral, the transfer functions between the response coordinate and the shaking coordinate are measured over the determined frequency range. Typical response coordinates for such measurements are: (1) nose vertical, (2) wing (right and/or left) vertical, (3) center-of-gravity vertical, (4) tail vertical, and (5) horizontal stabilizer vertical.

The test setup for measuring frequency-dependent mobility functions is shown in Figure A-10. The helicopter is suspended as a free body by soft rubber bungee chords. The configuration shown has the shaker located for vertical excitation at the tail and the accelerometer located for measuring vertical response in the vicinity of the horizontal stabilizer. Signals for driving the electromagnetic shaker originate from the signal generator. A force gage, installed at the point of force application, generates a voltage signal which is proportional to the applied force. This signal is input to the dual channel digital signal analyzer. The accelerometer at the response coordinate generates a voltage signal, proportional to the response acceleration, which is also input to the digital signal analyzer.

The signal analyzer is capable of sampling the time-domain force and response signals, digitizing these samples, and computing the real-time

191
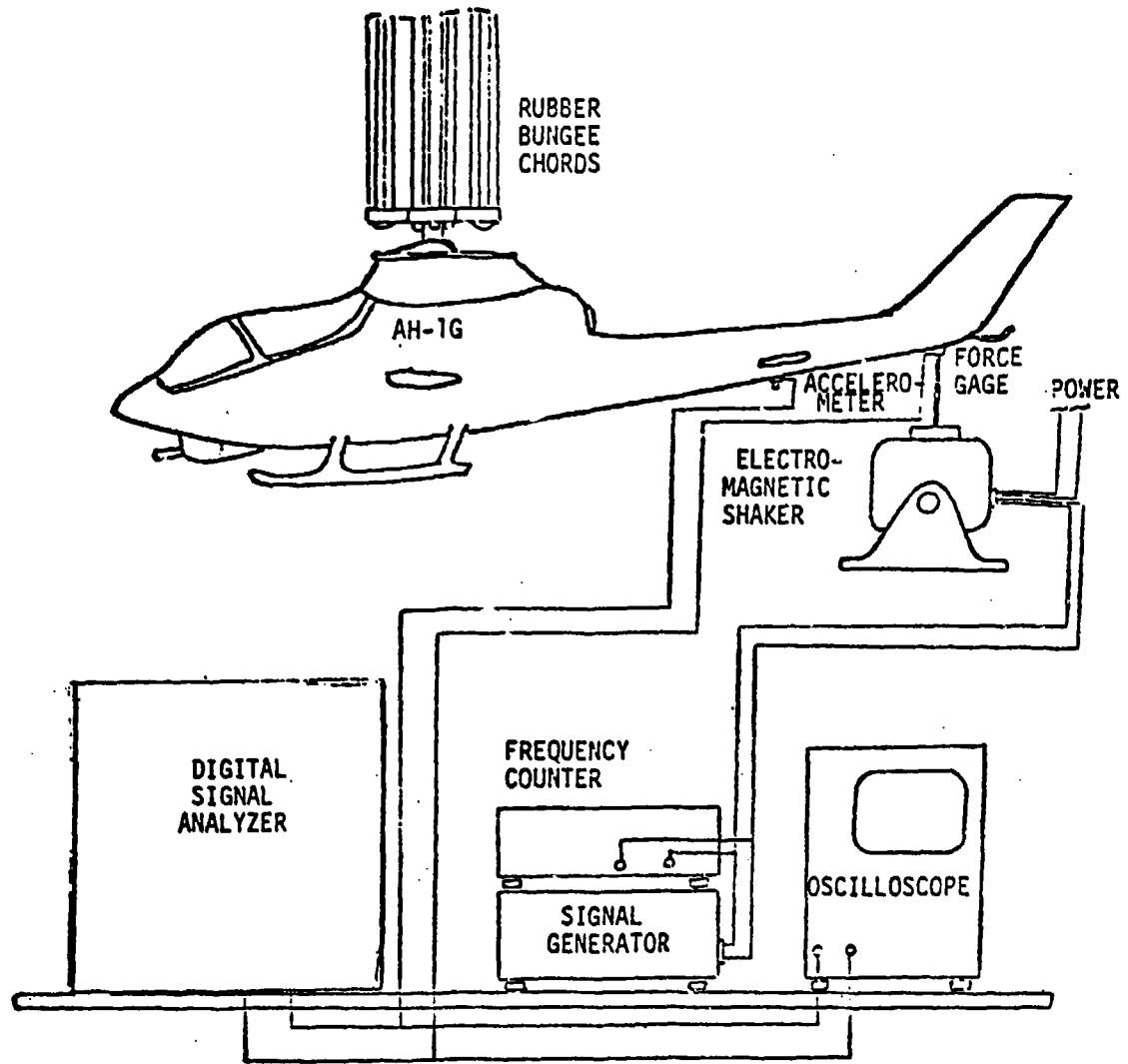
Figure A-10. Schematic of test setup for global parameter testing.

Fourier transforms of the data. It also computes the frequency-domain transfer function between the input and output spectra, which is the mobility between the response and forcing coordinates. All the frequency functions computed by the analyzer over the specified frequency interval can be stored on cassette tapes for future restoration and analysis. The oscilloscope allows the monitoring of the time-domain signals emanating from the force and response transducers. The frequency counter is used to precisely measure the frequencies of harmonic signals when required.

The accuracy with which the global parameters can be estimated is critically dependent on the quality of the data acquired for this purpose. For each pair of force and response locations, a random shake is done with the frequency bandwidth set to span twice the frequency range of interest. This is done to insure that the modes in the frequency range of interest are not coupled to modes occurring beyond the range, as may be the case when a local mode is present. For each shaking station, several force levels are tested until the range of applied force is reached where the mobility plots are independent of the force level. This is one of the linearity requirements for mobility measurement. Having established the required force level and the absence of local coupling modes at higher frequency, another random shake is done, this time with the bandwidth set at the frequency range of interest. The above procedure is repeated for all the accelerometers which have been selected for global parameter testing.

The ratio of modal acceleration coefficient to damping (A_{jkn}/g_n) varies not only from mode to mode but also from mobility to mobility, for a given mode, and the prominence of the various modes of the structure will be different in each of the mobilities recorded. That is, a given mode n occurring at Ω_n may appear very prominently on mobility $Y_{jk}(\omega)$, while the same mode may not be so significant in the mobility $Y_j\ell$, where ℓ designates a response coordinate different from k. This will especially

25
F

193

be the case if the mode shape associated with mode n has a much larger mode element at coordinate k than coordinate ℓ. The prominence of a mode may also be due to light damping. Thus, by examining the set of broadband mobilities recorded, it is possible to associate each mode n with the mobility where the mode appears most prominently.

Although it is possible to obtain rough estimates of the natural frequencies and damping of the structural elastic modes from these broad-band mobility plots, especially when damping is very light (e.g., peaks of the imaginary mobility plots, and frequency separation of the peaks in the real mobility plots), there are a number of specific considerations why broad-band mobility data is not suitable for global parameter extraction. Among these considerations are:

Measurement Accuracy - The low-frequency resolution associated with broad-band mobility measurements tends to introduce errors into the measured mobility values due to the phenomenon of leakage -- a spreading of the energy contained at each discrete frequency over a relatively narrow band nearby. Although considerable effort is exerted by equipment manufacturers in reducing leakage effects by using window techniques, the phenomenon still has to be reckoned with when the frequency resolution gets below certain limits. For acceptable measurements, bandwidths of about 25% of the center frequency have been recommended.

Parameter Extraction Accuracy - Also associated with low-frequency resolution are inaccuracies in the parameter extraction methods due to the frequency spacing between successive data points. The polar plot of mobilities (see Figure A-8), in the vicinity of a mode, describes a circular arc. Most methods for extracting natural frequencies, damping and modal acceleration coefficients are based on fitting a continuous circle through measured data and in some cases computing the rate of change of the arc length with frequency. Since the frequency data is discrete, arcs of the circle are necessarily approximated by segments. The error incurred by approximating

194

a circular arc by a straight line segment increases as the frequency spacing between successive data points increases. Narrow band data with bandwidth less than 25% of the natural frequency of a given mode have been found to yield sufficiently accurate results. Initial estimates of the natural frequencies can be obtained from the broad-band data.

For sufficient frequency resolution and to minimize leakage, the following bandwidths are recommended for use in narrow band testing using the HP5420A signal analyzer.

TABLE A-1.   BANDWIDTH RECOMMENDATIONS.

Natural Frequency Ω_n		Bandwidth
Equal to or greater than	But less than	
2 Hertz	3 Hertz	.5 Hertz
3	4	.781
4	6	1.000
6	8	1.5625
8	12	2.000
12	16	3.125
16	25	4.000
25	32	6.250
32	50	8.000
50	64	12.500
64	100	16.000

In cases of g_n greater than .25 broader bandwidth should be used and in all cases the natural frequency should be the center frequency.

SWEPT SINE TESTING

For all the narrow band mobility measurements, the excitation was achieved by applying pure sine wave signals to the electromagnetic shaker and varying the frequency of the sine waves over the range spanned by the bandwidth. This so-called swept sine technique was preferred to other excitation techniques over a narrow frequency band. Other reasons for choosing the swept sine technique are that:

1. The energy input into each measurement frequency is maximum.

2. By choosing the right sweep speed (see sketch below), the steady-state sinusoidal response of the structure is achieved at each measurement frequency. This is one of the assumptions made in the derivation of the generalized linear model.

3. Measurements are more accurate and reproducible.

4. The sampling frequencies and the adequate number of averages are more easily determined.

5. Good linearity and reciprocity checks are obtained.

6. High resolution of close modes can be achieved by selecting the right sweep speed.

Consider an undamped single degree of freedom linear system, described by the following equation of forced vibrations:

$$m\ddot{x} + kx = Fe^{i\omega t} \tag{A-41}$$

If the forcing frequency coincides with the undamped natural frequency, i.e., $\omega = \sqrt{\dfrac{k}{m}}$, the response of the system grows linearly with time.

196

Schematically:
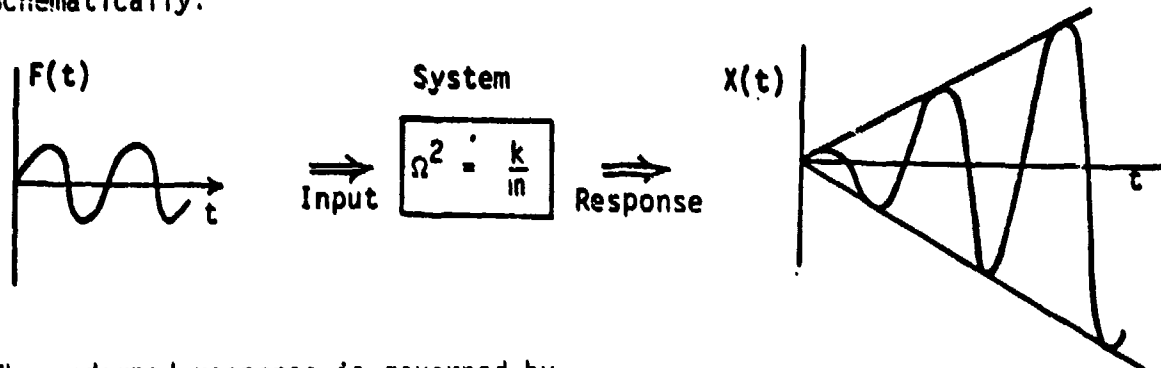
The undamped response is governed by

$$\ddot{x} + \Omega^2 x = \frac{F}{m} e^{i\Omega t} \tag{A-42}$$

or

$$x(t) = -i \frac{Ft}{2m\Omega} e^{i\Omega t} \tag{A-43}$$

However, because of the various dissipative mechanisms which constitute damping, the oscillations reach a limiting amplitude after some time τ.
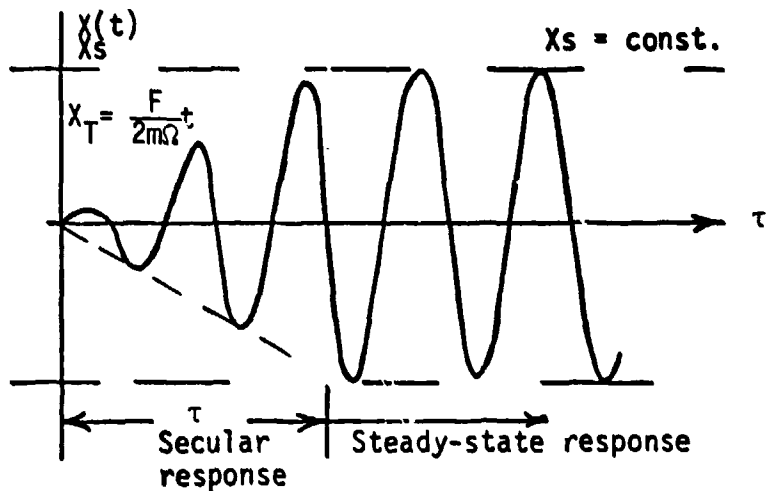
For hysteretic damping, g, the steady-state response is governed by

$$\ddot{x} + (1 + ig)\Omega^2 x = \frac{F}{m} e^{i\Omega t} \tag{A-44}$$

197

or $\quad x(t) = -\dfrac{F}{mg\Omega^2} e^{i\Omega t}$ $\hspace{4cm}$ (A-45)

The steady-state amplitude is given by

$$Xs = \dfrac{F}{mg\Omega^2} \hspace{4cm} (A\text{-}46)$$

and the characteristic time for reaching steady-state response can be estimated by equating

$$X_T(\tau) = Xs \hspace{4cm} (A\text{-}47)$$

which gives $\quad \dfrac{F}{2m\Omega} \tau = \dfrac{F}{mg\Omega^2}$ $\hspace{3cm}$ (A-48)

thus $\hspace{2cm} \tau = \dfrac{2}{g\Omega} = \dfrac{1}{\pi g f}$ $\hspace{3cm}$ (A-49)

where f = frequency in Hz.

Suppose there are two neighboring structural modes with the natural frequencies separated by Δf, Hz. To resolve these two close modes, the speed at which the excitation frequency is changing must be of the order of

$$v = \dfrac{\Delta_f}{\tau} = \pi g f \, \Delta_f \quad \text{Hz/sec} \hspace{3cm} (A\text{-}50)$$

where $\quad$ g = damping coefficient (lower bound)

$\hspace{2cm} \Delta_f$ = mode resolution in Hz.

or
$$v \propto f \hspace{4cm} (A\text{-}51)$$

for a given frequency separation between modes to be determined and for a given damping coefficient.

The relationship between the linear scale and the logarithmic scale on the signal generator is

$$f_{dec} = \log_{10} \frac{f_{Hz}}{f_o} \qquad \text{(A-52)}$$

where f_{Hz} = frequency in hertz $(f_o \leq f_{Hz} \leq 10 f_o)$

f_{dec} = frequency in decades $(0 \leq f_{dec} \leq 1.0)$

f_o = base frequency on the scale

From equation (A-52) $\quad f_{Hz} = f_o \times 10^{f_{dec}} \qquad \text{(A-53)}$

Sweep speed $\quad v = \dfrac{df_{Hz}}{df_{dec}} = \dfrac{df_{Hz}}{df_{dec}} \times \dfrac{df_{dec}}{dt} \quad$ Hz/sec. $\qquad \text{(A-54)}$

From equation (A-53) $\dfrac{df_{Hz}}{df_{dec}} = (f_o \ln 10) \times 10^{f_{dec}} = f_{Hz} \ln 10 \qquad \text{(A-55)}$

and $\quad \dfrac{v}{f_{Hz}} = \dfrac{df_{dec}}{dt} \ln 10 \qquad \text{(A-56)}$

Thus, by selecting a constant logarithmic sweep speed $(df_{dec}/dt = \text{const.} = \alpha)$, equation (A-51) is automatically satisfied.

The constant α is determined by substituting the desired value of $\dfrac{v}{f_{Hz}}$ into equation (A-56). For example, if at 2 Hz we desire a sweep rate of 0.01 Hz/sec, then

$$\alpha = \frac{0.01(60)}{2 \ln 10} \text{ dec/min} = .13 \text{ dec/min} \qquad \text{(A-57)}$$

199

ESTIMATION OF GLOBAL PARAMETERS

Various techniques have been developed for estimating the natural frequencies and damping coefficients of the elastic modes of a structure from mobility data. In all cases, certain assumptions have to be made about these modes. The simplest case is when the mode is well separated and lightly damped. For such modes, the natural frequency can be approximated by the peak of the imaginary displacement mobility. The damping coefficient can be estimated as

$$ g_n \simeq \frac{1}{2} \frac{\omega_2^2 - \omega_1^2}{\Omega_n^2} \simeq \frac{\omega_2 - \omega_1}{\Omega_n} \tag{58} $$

where ω_2 and ω_1 are the turning point frequencies in the real displacement mobility. The above simple case is almost exclusively reserved for simple structures with uniform distribution of mass, stiffness, and damping. Very few of the modes of the helicopter can be treated this way.

The ds/df^2 method of Kennedy and Pancu - The following is a more general approach which has been found to work well for both classical and complex, close or separated modes. By analogy with equations (A-32) through (A-37), the jkth displacement mobility can be expressed as

$$ Y_{jk} = \frac{E_{jk}}{-\omega^2} + \sum_{n=1}^{N} \left\{ \left(A_{jkn}^R \ F_n^R - A_{jkn}^I \ F_n^I \right) + i \left(A_{jkn}^R \ F_n^I + A_{jkn}^I \ F_n^R \right) \right\} \tag{A-59} $$

where $A_{jkn} = A_{jkn}^R + iA_{jkn}^I$ is the jkth modal acceleration coefficient of nth mode and E_{jk} is the contribution from the rigid body modes.

Recall that

$$ F_n(\omega) = F_n^R(\omega) + i \ F_n^I(\omega) = \frac{-1}{\omega^2} \ddot{F}_n(\omega) \tag{A-60} $$

which gives

$$F_n^R(\omega) = \frac{1}{\Omega_n^2} \frac{1 - \omega^2/\Omega_n^2}{\left[1 - \omega^2/\Omega_n^2\right]^2 + g_n^2} \tag{A-61}$$

and

$$F_n^I(\omega) = \frac{1}{\Omega_n^2} \frac{-g_n}{\left[1 - \omega^2/\Omega_n^2\right]^2 + g_n^2} \tag{A-62}$$

In the immediate vicinity of the nth natural frequency, the displacement mobility can be approximated by

$$Y_{jk}(\omega \approx \Omega_n) \approx \left[A_{jkn}^R F_n^R(\omega) - A_{jkn}^I F_n^I(\omega) + C_n^R \frac{\omega^2}{\Omega_n^2} + d_n^R \right]$$

$$+ i \left[A_{jkn}^R F_n^I(\omega) + A_{jkn}^I F_n^R(\omega) + C_n^I \frac{\omega^2}{\Omega_n^2} + d_n^I \right] \tag{A-63}$$

In equation (A-63), the sum of the contributions from all other modes has been represented by a complex straight line

$$\left[C_n^R + i\, C_n^I \right] \frac{\omega^2}{\Omega_n^2} + d_n^R + i\, d_n^I$$

Dropping the subscripts j, k, and n, and writing the real and imaginary parts of the displacement mobility separately, gives

$$Y^R(\omega \approx \Omega) \approx A^R F^R(\omega) - A^I F^I(\omega) + C^R \frac{\omega^2}{\Omega^2} + d^R \tag{A-64}$$

$$Y^I(\omega \approx \Omega) \approx A^R F^I(\omega) + A^I F^R(\omega) + C^I \frac{\omega^2}{\Omega^2} + d^I \tag{A-65}$$

If the nth mode is classical and well separated the imaginary part of the modal acceleration coefficient vanishes and the contributions from other modes are nearly independent of frequency. In other words, A^I, C^R, and C^I vanish. Thus,

$$\gamma^R \ (\omega \simeq \Omega) \simeq \ A^R \ F^R(\omega) + d^R \qquad (A-66)$$

$$\gamma^I \ (\omega \simeq \Omega) \simeq \ A^R \ F^I(\omega) + d^I \qquad (A-67)$$

The peak of the imaginary mobility occurs when

$$\frac{d\gamma^I}{d(\omega^2)} = 0 = A^R \ \frac{d}{d(\omega^2)} \left[F^I(\omega)\right] \qquad (A-68)$$

or

$$\frac{A^R}{2} \ \frac{2/\Omega^2 \ g \ 1 - \omega^2/\Omega^2}{\left[\left[1 - \omega^2/\Omega^2\right]^2 + g^2\right]^2} = 0 \qquad (A-69)$$

which is when $\omega^2/\Omega^2 = 1$, as stated previously.

The peaks of the real displacement mobility occur when

$$\frac{d\gamma^R}{d(\omega^2)} = 0 = A^R \frac{d}{d(\omega^2)} \left[F^R(\omega)\right] \qquad (A-70)$$

or

$$\frac{A^R}{\Omega^4} \ \frac{\left[1 - \omega^2/\Omega^2\right]^2 - g^2}{\left[\left[1 - \omega^2/\Omega^2\right]^2 + g^2\right]^2} = 0 \qquad (A-71)$$

which gives peaks at

$$\frac{\omega_1^2}{\Omega^2} = 1 - g \qquad (A-72)$$

and

$$\frac{\omega_2^2}{\Omega^2} = 1 + g \qquad (A-73)$$

202

or $\quad g = \dfrac{1}{2} \dfrac{\omega_2^2 - \omega_1^2}{\Omega^2}$ $\qquad\qquad\qquad\qquad\qquad\qquad\qquad$ (A-74)

When the mode is complex, equations (A-64) and (A-65) indicate that both the real and imaginary parts of the displacement mobility contain linear combinations of $F^R(\omega)$, $F^I(\omega)$, ω^2 and constants. The peaks in the mobilities in the general case may not be simply related to the natural frequency and damping coefficients. Naturally, different degrees of approximations are feasible, depending on how complicated the situation really is.

A general technique that has been found to be applicable to the majority of modes encountered on the AH-1G helicopter is based on the rate of change of the arc length of the modal curve (plotted on the complex plane, i.e., the plot of the Y^I against Y^R with frequency as a parameter).

$$\frac{ds}{d(\omega^2)} = \sqrt{\left[\frac{dY^R}{d(\omega^2)}\right]^2 + \left[\frac{dY^I}{d(\omega^2)}\right]^2}$$ $\qquad\qquad$ (A-75)

where s is the arc length.

The rate of change of the arc length with respect to the square of frequency is stationary when

$$\frac{d^2s}{d(\omega^2)^2} = 0 = \frac{\dfrac{dY^R}{d(\omega^2)}\dfrac{d^2Y^R}{d(\omega^2)^2} + \dfrac{dY^I}{d(\omega^2)}\dfrac{d^2Y^I}{d(\omega^2)^2}}{\sqrt{\left[\dfrac{dY^R}{d(\omega^2)}\right]^2 + \left[\dfrac{dY^I}{d(\omega^2)}\right]^2}}$$ $\qquad$ (A-76)

or

$$\frac{dY^R}{d(\omega^2)}\frac{d^2Y^R}{d(\omega^2)^2} + \frac{dY^I}{d(\omega^2)}\frac{d^2Y^I}{d(\omega^2)^2} = 0$$ $\qquad\qquad$ (A-77)

By substituting equations (A-64) and (A-65) into equation (A-77) and simplifying, the following condition for the peak of the $\frac{ds}{d(\omega)^2}$ plot is obtained:

$$|A|^2 \ \frac{d}{d(\omega^2)} \left\{ \left[\frac{dF^R}{d(\omega^2)}\right]^2 + \left[\frac{dF^I}{d(\omega^2)}\right]^2 \right\} + \frac{C^R}{2} \left\{ A^R \ \frac{d^2F^R}{d(\omega^2)^2} - A^I \ \frac{d^2F^I}{d(\omega^2)^2} \right\}$$

$$+ \ \frac{C^I}{\Omega^2} \left\{ A^R \ \frac{d^2F^I}{d(\omega^2)^2} + A^I \ \frac{d^2F^R}{d(\omega^2)^2} \right\} = 0 \qquad \text{(A-78)}$$

where $|A|^2 \equiv (A^R)^2 + (A^I)^2$

For a well separated mode, the constants C^R and C^I will be nearly zero and equation (A-78) gives

$$\frac{d}{d(\omega^2)} \left\{ \left[\frac{dF^R}{d(\omega^2)}\right]^2 + \left[\frac{dF^I}{d(\omega^2)}\right]^2 \right\} = 0 \qquad \text{(A-79)}$$

Equation (A-79) does not involve the modal acceleration coefficients A^R and A^I. Thus, the condition for the peaking of the rate of change of the arc length with respect to frequency squared holds true regardless of how complex the mode is, as long as it is well separated.

Equation (A-79) can be expanded, making use of equations (A-61) and (A-62), and the result is

$$\frac{d}{d(\omega^2)} \left[\frac{\left[\left[\left(1 - \frac{\omega^2}{\Omega^2}\right)^2 - g^2\right]^2 + 4g^2 \left[1 - \frac{\omega^2}{\Omega^2}\right]^2\right]}{\Omega^8 \left[\left(1 - \frac{2}{\Omega^2}\right)^2 + g^2\right]^4} \right] = 0 \qquad \text{(A-80)}$$

Equation (A-80) can be evaluated to yield

$$\frac{d}{d(\omega^2)} \left[\frac{1}{\Omega^8 \left[\left(1 - \frac{\omega^2}{\Omega^2}\right)^2 + g^2 \right]^2} \right] = \frac{4}{\Omega^{10}} \frac{1 - \frac{\omega^2}{\Omega^2}}{\left[\left(1 - \frac{\omega^2}{\Omega^2}\right)^2 + g^2 \right]^3} = 0 \qquad \text{(A-81)}$$

Thus, for a well separated mode, the peak of the $\frac{ds}{d(\omega^2)}$ plot will occur at the natural frequency, regardless of whether the mode is complex or classical. Any suitable finite difference scheme can be used to compute $\frac{ds}{d(\omega^2)}$ from measured data using equation (A-75).

Even for modes that are not well separated, the peaks of the $\frac{ds}{d(\omega^2)}$ plot still give good approximations to the natural frequencies. To establish why this is so, consider equation (A-78) term by term; the first term vanishes at the natural frequency, as we have already seen, and the remaining terms can be rearranged as

$$\frac{1}{\Omega^2} \frac{d^2 F^R}{d(\omega^2)^2} \left(c^R A^R + c^I A^I \right) + \frac{1}{\Omega^2} \frac{d^2 F^I}{d(\omega^2)^2} \left(c^I A^R - c^R A^I \right) \qquad \text{(A-82)}$$

At the natural frequency $\frac{d^2 F^R}{d(\omega^2)^2} = 0$ (A-83)

the remaining term becomes

$$- \frac{2}{\Omega^8 g^3} \left(c^I A^R - c^R A^I \right)$$

Lightly damped modes generally tend to be classical and well separated. This is understandable, since in the limit of zero damping, a classical undamped mode results. Thus, the low damping that drives $2/\Omega^8 g^3$ up, also drives $\left(c^I A^R - c^R A^I \right)$ down, effectively neutralizing the expression. This consequently reduces the error incurred by approximating

205

the natural frequency by the peak of the $ds/d(\omega^2)$ plot. Experience has shown that modes which are too close to be resolved by the $ds/d(\omega^2)$ routine, may probably not be resolvable by any other method presently known.

The diameter of the modal circle that fits the curvature of the displacement mobility plot (on the polar plane) in the vicinity of the natural frequency is

$$D = \frac{|A|}{g\Omega^2} \qquad\qquad (A-84)$$

At the natural frequency

$$\frac{dY^R}{d(\omega^2)} \bigg|_{\omega\,=\,\Omega} = -\frac{A^R}{g^2\Omega^4} + \frac{C^R}{\Omega^2} \qquad\qquad (A-85)$$

and

$$\frac{dY^I}{d(\omega^2)} \bigg|_{\omega\,=\,\Omega} = -\frac{A^I}{g^2\Omega^4} + \frac{C^I}{\Omega^2} \qquad\qquad (A-86)$$

Substituting equations (A-85) and (A-86) into equation (A-75) gives

$$\frac{ds}{d(\omega^2)} \bigg|_{\omega\,=\,\Omega} = \frac{|A|}{g^2\Omega^4} + \text{Error of approximation} \qquad\qquad (A-87)$$

The plot of arc length s against ω^2 has a characteristic S shape, as shown by the sketch below

206
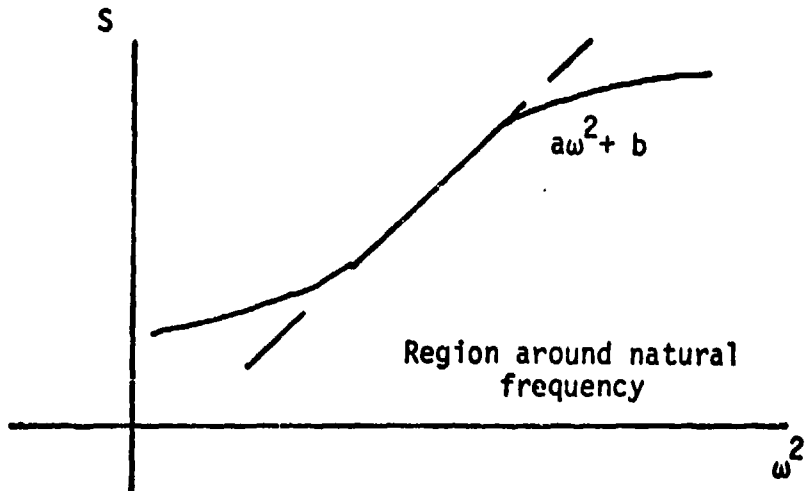
By fitting the best straight line to the inflection region of the S curve, one obtains a, the gradient of this line.

$$a \simeq |A|/g^2 \Omega^4 \qquad \text{(A-88)}$$

From equations (A-84) and (A-88), the damping coefficient is evaluated as

$$g \simeq D/a\Omega^2 \qquad \text{(A-89)}$$

where D is the diameter of the circle fit to mobility data, a is the gradient of the line fit to the S plot, and Ω is the natural frequency.

TESTING FOR ORTHONORMAL MODES AND MODESHAPES

The mode shapes of any structure are related to the modal acceleration coefficients as shown in equation (A-28); i.e.,

$$A_{jkn} = \frac{1}{m_n} \phi_{jn} \phi_{kn} \qquad \text{(A-90)}$$

where ϕ_{jn} and ϕ_{kn} are mode shape elements at the jth and kth coordinates of the nth mode, m_n is the generalized mass of the nth mode.

The orthonormal mode elements are defined as

$$\psi_{jn} \equiv \sqrt{\frac{1}{m_n}} \, \phi_{jn} \qquad \text{(A-91)}$$

and

$$\psi_{kn} \equiv \sqrt{\frac{1}{m_n}} \, \phi_{kn} \qquad \text{(A-92)}$$

Thus, $\qquad A_{jkn} = \psi_{jn} \psi_{kn} \qquad \text{(A-93)}$

and $\qquad A_{jjn} = (\psi_{jn})^2 \qquad \text{(A-94)}$

It follows from equations (A-93) and (A-94) that

$$\psi_{kn} = \frac{A_{jkn}}{\sqrt{A_{jjn}}} \tag{A-95}$$

It can also be deduced that

$$\psi_{kn} = \pm\sqrt{\frac{A_{jkn} \, A_{\ell kn}}{A_{\ell jn}}} \tag{A-96}$$

The choice of using either equation (A-95) or equation (A-96) to determine ψ_{kn} depends on the accessibility of the modal acceleration coefficients involved. Note that two shaking stations are involved in equation (A-96), whereas only one shaking station is involved in equation (A-95). It may turn out that the driving-point data that yields A_{jjn} are such that accurate estimations of the A_{jjn} for a number of the modes are not easy. This may be due in part to a strong local mode coupling, or a residual effect. In cases where this is so, it may be better to shake at a number of coordinates and then use schemes similar to that in equation (A-96).

Consistency of the phase angle in equation (A-96) is achieved in the following manner. For an orthonormal mode element, in the nth mode, of large magnitude, say ψ_{kn}, let

$$\psi_{kn} = \left| \sqrt{\frac{|A_{jkn}| \cdot |A_{\ell kn}|}{|A_{\ell jn}|}} \right| \angle \frac{1}{2}(\phi_{jkn} + \phi_{\ell kn} - \phi_{\ell jn}) \tag{A-97}$$

where ϕ is phase angle. For any other orthonormal mode element, say p,

$$\psi_{pn} = \left| \sqrt{\frac{|A_{jpn}| \cdot |A_{\ell pn}|}{|A_{\ell jn}|}} \right| \angle \frac{1}{2}(\phi_{jpn} + \phi_{\ell pn} - \phi_{\ell jn}) \tag{A-98}$$

Mode shapes of the structure, normalized with respect to the highest mode element, can be obtained directly from the modal acceleration coefficients as

$$\{\phi\}_n = \frac{1}{A_{j,max,n}} \left\{ \begin{array}{c} A_{j1n} \\ A_{j2n} \\ \vdots \\ A_{jNn} \end{array} \right\} \tag{A-99}$$

where $A_{j,max,n}$ is the modal acceleration coefficient with the maximum amplitude in the column corresponding to the nth mode, when shaking at the jth coordinate. The generalized mass, corresponding to the mode shape thus normalized is computed from equation (90) as

$$m_n = \phi_{jn} \ \phi_{kn}/A_{jkn} = A_{jjn}/(A_{j,max,n})^2 \tag{A-100}$$

In order to obtain the elements of the orthonormal modes and mode shapes, the modal acceleration coefficients of all the modes for the mobilities relating the response coordinates to the shaking coordinates have to be determined. The computational scheme for determining the modal acceleration coefficients requires mobility data at discrete frequencies. The technique, herein referred to as the matrix difference method, well suited to processing large numbers of transducers for modal analysis using multiplexing data acquisition systems common in the helicopter industry. The natural frequencies and modal damping must be determined beforehand.

For two frequencies ω_i^+ and ω_i^- in the region of the natural frequency of the ith mode, equation (A-34) could be written thus:

$$\Delta_i \ddot{Y}_{jk} = \ddot{Y}_{jk}(\omega_i^+) - \ddot{Y}_{jk}(\omega_i^-) = \sum_{n=1}^{N} A_{jkn} \Delta_i \ddot{F}_n \tag{A-101}$$

where

$$\Delta_i \ddot{F}_n = \ddot{F}_n(\omega_i^+) - \ddot{F}_n(\omega_i^-)$$

Equation (A-101) can be written for all the remaining modes, having selected the corresponding pairs of frequencies. The resulting system of

equations is the matrix difference equation:

$$
\begin{Bmatrix} \Delta_1 \ddot{Y}_{jk} \\ \Delta_2 \ddot{Y}_{jk} \\ \vdots \\ \Delta_N \ddot{Y}_{jk} \end{Bmatrix}
=
\begin{bmatrix}
\Delta_1 \ddot{F}_1 & \Delta_1 \ddot{F}_2 & \cdots & \Delta_1 \ddot{F}_N \\
\Delta_2 \ddot{F}_1 & \Delta_2 \ddot{F}_2 & \cdots & \Delta_2 F_N \\
\bullet & \bullet & & \bullet \\
\Delta_N \ddot{F} & \Delta_N \ddot{F}_2 & & \Delta_N \ddot{F}_N
\end{bmatrix}
\begin{Bmatrix} A_{jk1} \\ A_{jk2} \\ \vdots \\ A_{jkN} \end{Bmatrix}
\qquad \text{(A-102)}
$$

or
$$ \{ \Delta \ddot{Y}_{jk} \} = [\Delta \ddot{F}] \{ A_{jk} \} \qquad \text{(A-103)} $$

From which $\{ A_{jk} \} = [\Delta F]^{-1} \{ Y_{jk} \}$ $\qquad \text{(A-104)}$

An immediate observation about the matrix difference scheme is that all contributions to the mobilities near a given mode which are weakly varying with frequency, such as the effects of distant modes or rigid body modes, are subtracted out.   Proper selection of ω_i^+ and $\omega_i^-, \Delta_i F_n$ can be made such that $\Delta_i F_i$ is large and $\Delta_i F_j$ is small for all $j \neq i$. Experience shows that

$$ \omega_i^+ = \Omega_i (1 + g_i/_2) \qquad \text{(A-105)} $$

and

$$ \omega_i^- = \Omega_i (1 - g_i/_2) \qquad \text{(A-106)} $$

are the most effective choices for the upper and lower discrete frequencies. For these discrete frequencies, the matrix $[\Delta F]$ is well conditioned for inversion since the off-diagonal terms are small compared to the diagonal terms.

Test procedure - Figure A-11 shows the schematic of the instrumentation setup for the shake test for orthonormal modes and mode shapes. Signals from all the accelerometers and from the force gage are transmitted via telemetry to a computer where the transfer functions between the response coordinates and the force coordinate are computed and printed out. The excitation signals are sinusoidal at the discrete frequencies ω_i^+ and ω_i^- for $i = 1, 2, \ldots N$. The same force levels used for the swept sine global parameter shake test are also used for the modal shake test at the corresponding discrete frequencies.

DERIVATION OF MOBILITIES

Underlying any technique of modal analysis is the principle of linear decomposition of structural response mobility into contributions from the natural modes occurring between a chosen frequency interval. The preceding methods estimate not only the natural frequencies and damping coefficients of each mode, but also the modal acceleration coefficients of each modal contribution to the mobility between response and forcing coordinates.

Subsequent to the determination of the modal parameters and modal constants, the next logical step is to reconstruct mobilities both between a pair of forcing and response coordinates over a continuous frequency interval, and at a chosen frequency between several pairs of forcing and response coordinates. By comparing the mobility derived over a continuous frequency range with the measured mobility over the same frequency range, some assessment of the accuracy of the global parameter estimations can be made. The comparison of discrete frequency mobilities for a large number of coordinate pairs allows the assessment of the acceptability of the orthonormal mode and mode shape calculations. The results of these comparisons build the confidence in the mobilities which are derived but not actually measured.

211
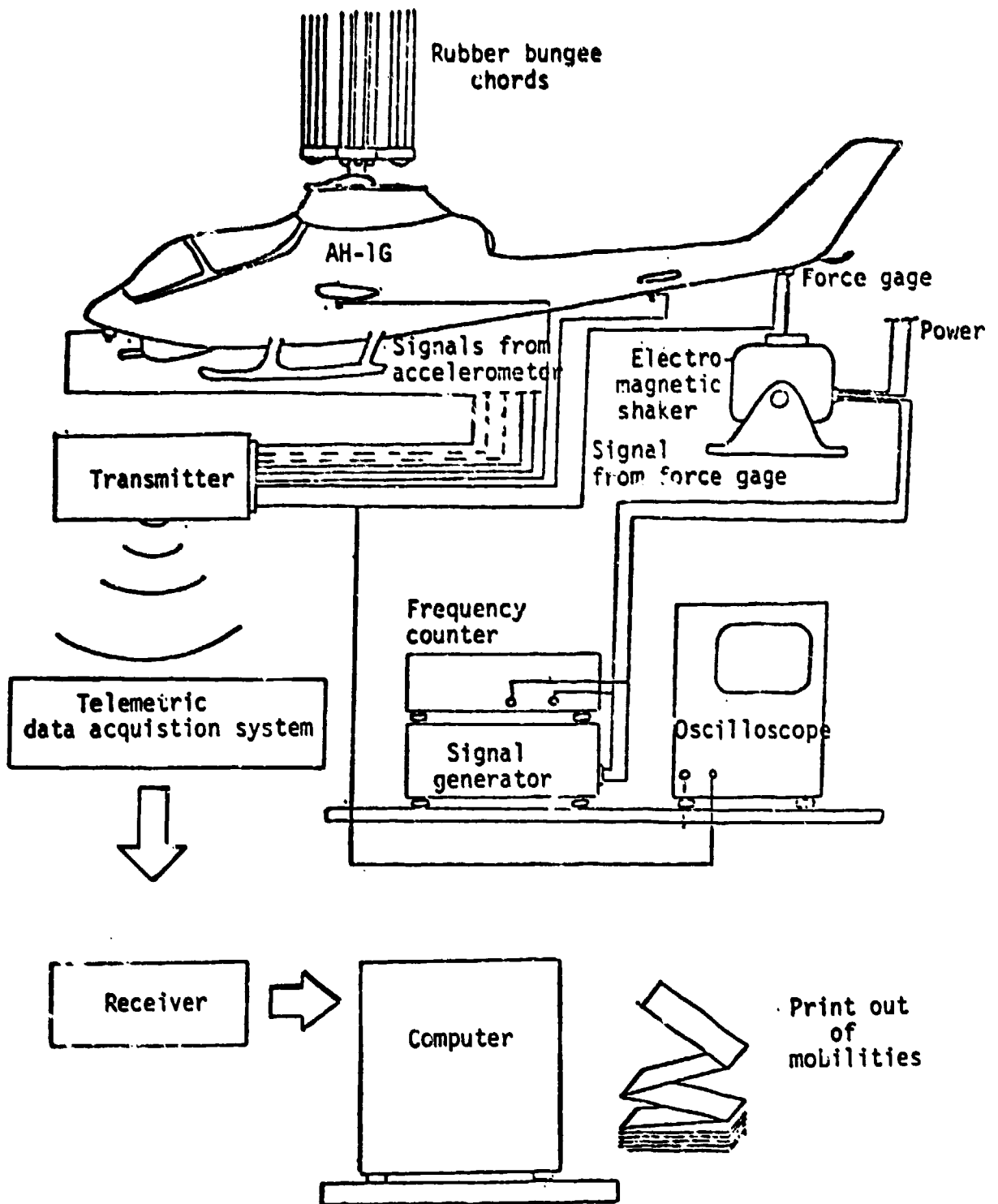
Figure A-11.   Schematic of test setup for matrix difference
method of modal testing.

Comparison of measured and simulated mobilities over frequency band -
Global parameters Ω_n and g_n of system modes occurring within a specified
frequency range can be satisfactorily estimated using methods based on the
properties of the mode functions, $F(\omega)$. The matrix difference method can
then be used to calculate the modal acceleration coefficients (A^R_{jkn}, A^I_{jkn})
of the relevant elastic modes. Table A-2 summarizes the parameters esti-
mated between 0 and 50 Hz from the tail vertical shake/nose vertical
acceleration data. Figure A-12 shows plots of the mobility measured
between 2 and 50 Hz. Using the parameters of Table A-2 and equation (A-31),
without including the rigid body coefficients, the plots of Figures A-13,
A-14, and A-15 were generated.

The computed and measured mobilities are superimposed in Figures A-14 and
A-15. It is seen that the two plots agree to within a frequency indepen-
dent complex constant, which is an estimate of the contribution of the
rigid body modes.

TABLE A-2. ESTIMATED MODAL PARAMETERS BETWEEN
0 - 50 Hz (TAIL VERTICAL SHAKE, NOSE
VERTICAL ACCELERATION)

| Mode no. n	Natural frequency Ω_n (Hz)	Damping coefficient g_n	Nose/tail modal acceleration coefficient	
			Real $A^R_{ZN, ZT, n}$ (g/lb)	Imaginary $A^I_{ZN, ZT, n}$ (g/lb)
1	7.33	0.062	7.26×10^{-4}	1.40×10^{-4}
2	8.09	0.12	4.48×10^{-4}	-3.55×10^{-4}
3	13.3	0.13	-1.57×10^{-5}	-4.97×10^{-6}
4	15.97	0.085	2.25×10^{-5}	1.39×10^{-4}
5	16.35	0.05	5.18×10^{-5}	-1.04×10^{-6}
6	17.63	0.08	1.37×10^{-4}	-5.54×10^{-5}
7	22.1	0.15	-7.28×10^{-5}	-4.06×10^{-4}
8	28.4	0.11	-1.06×10^{-4}	1.13×10^{-4}
9	40.7	0.12	7.84×10^{-6}	-2.16×10^{-5}
10	45.3	0.026	4.02×10^{-5}	1.42×10^{-4}
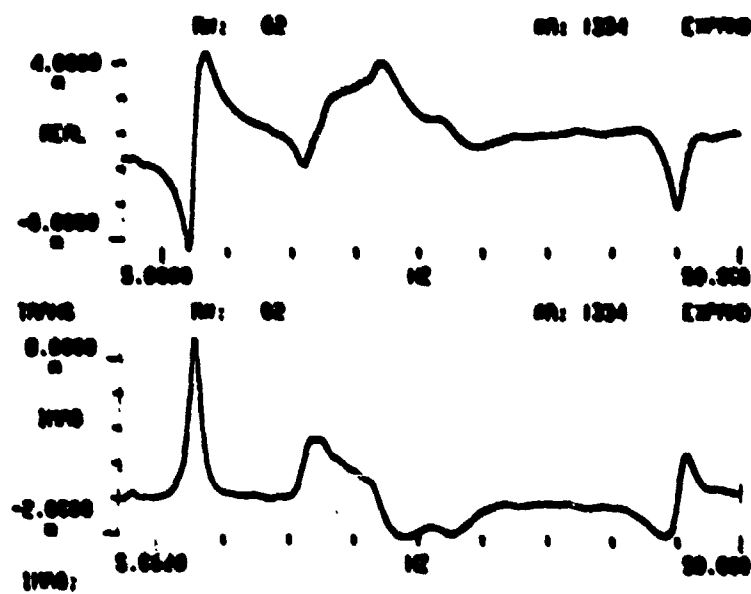
Figure A-12.   Measured acceleration mobility
between 2 Hz and 200 Hz.
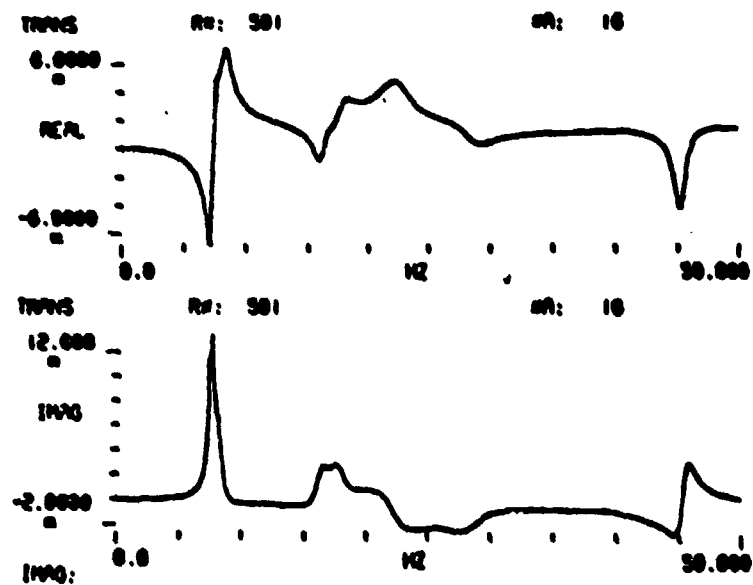
Figure A-13. Numerical simulation of the elastic component of the
acceleration mobility between 0 Hz and 50 Hz.

214
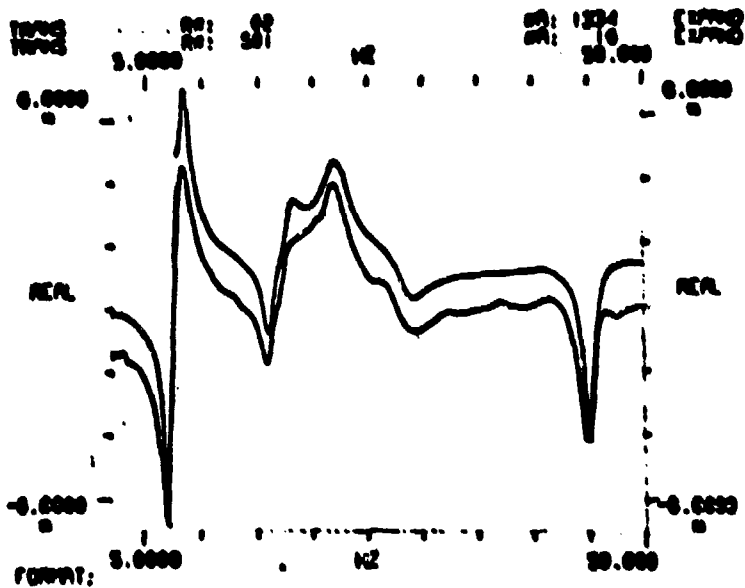
Figure A-14.   Simulated and measured real part of
acceleration mobility 2 - 50 Hz.
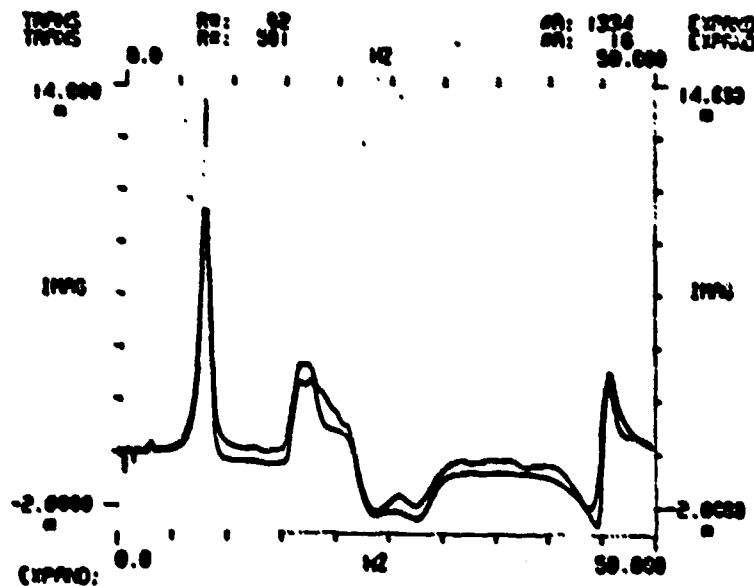
Figure A-15.   Simulated and measured imaginary part of
acceleration mobility 2 - 50 Hz.

Modal Series Method - Equation (A-31) can be rewritten in the following form:

$$\ddot{Y}_{jk} = E_{jk} + R^L_{jk}(\omega) + \sum_{n=1}^{N} A_{jkn} \ddot{F}_n(\omega) + R^H_{jk}(\omega) \tag{A-107}$$

where

$R^L_{jk}(\omega)$ is the low-frequency mobility residual; i.e., contributions to the mobility by elastic modes which occur at frequency below the lower test frequency limit.

$R^H_{jk}(\omega)$ is the high-frequency mobility residual.

The rigid body acceleration coefficient, E_{jk}, is determined from geometry and weights data.

If the lower test frequency limit is near zero, it follows that $R^L = 0$. The higher test frequency limit is usually selected high enough so that R^H can be safely assumed to vanish for all but certain driving-point mobilities which may suffer either from local mode effects or from high-frequency mode residuals.

When the natural frequencies, the damping coefficients, and the modal acceleration coefficients have been determined, the acceleration mobilities between pairs of motion coordinates which do not include the shaking coordinate can be computed from

$$\ddot{Y}_{\ell m} = E_{\ell m} + \sum_{n=1}^{N} \frac{A_{\ell kn} A_{mkn}}{A_{kkn}} \ddot{F}_n(\omega) \tag{A-108}$$

where k is the coordinate of the shaking station for the data which generated $A_{\ell k}$ and A_{mk}. It is necessary to select the shaking station k such that there is no local mode or high-frequency residual effect on the estimated value of A_{kkn}.

If only N_k of the modes are well defined by shaking at k, while the remaining N_p modes are better defined by the shake at p, then

$$\ddot{Y}_{\ell m} = E_{\ell m} + \sum_{n=1}^{N_k} \frac{A_{\ell kn} A_{mkn}}{A_{kkn}} \ddot{F}_n(\omega) + \sum_{n=1}^{N_p} \frac{A_{\ell pn} A_{mpn}}{A_{ppn}} \ddot{F}_n(\omega) \tag{A-109}$$

5166-81